UNIVERSIDADE DE LISBOA
FACULDADE DE CIÊNCIAS
DEPARTAMENTO DE ENGENHARIA GEOGRÁFICA, GEOFÍSICA E ENERGIA

Magnetic Records of Acidification Events at the Cretaceous-Paleogene (KPg) and Paleocene-Eocene Thermal Maximum (PETM) boundaries

Mariana do Amaral Frazão Queiroz de Andrade

Mestrado em Ciências Geofísicas
Especialização em Geofísica Interna

Dissertação orientada por:
Professor Doutor Eric Font (IDL- Universidade de Lisboa)
Professor Doutor Thierry Adatte (ISTE – Lausanne University)

2018

Acknowledgements

I would first like to thank Dr. Eric Font, who introduced me to geomagnetism, for believing in my abilities from the beginning and for his guidance during this project. Thanks also to Dr. Eric Font for his patience and for encouraging me to proceed my academic education.

I am grateful to Dr. Thierry Adatte for providing the samples and the mineralogical data from Dababiya and for his guidance during PETM data discussion.

Thanks to Alexandra Abrajeivitch for her willingness to do the FORC analysis.

Thanks to Dr. João Mata for his clarifications, which allowed me to better understand and interpret important data during the discussion of this project.

Thanks to Teresa and Guida for revising part of the thesis and for their help in improving my English writing.

A very special thanks to Ivo, Rita and Caldeirinha, who accompanied me along this journey since the very beginning, for their support and for helping me in some laboratory work. Thanks to Susana for her support in the final stages of the thesis.

Finally, a special acknowledgement to my family, especially to my sister Marta, my mother, Zé and Guida (once again) for their help, and all their emotional support and constant encouragement.

Abstract

The KPg mass extinction (~66 Ma) and the PETM (~56 Ma) are both abrupt and global climate events in Earth's history. The KPg mass extinction is commonly attributed to the Chicxulub impact, but in the last decades it has been linked to the Deccan volcanism. The abrupt warming during the PETM is attributed to methane release from seafloor sediments as consequence of the ocean warming due to the North Atlantic Igneous Province (NAIP) volcanic activity. The mechanisms by which these magmatic events led to global climate changes are still poor constrained. A recent approach combining rock magnetic techniques and mineralogical data provided interesting benchmarks to identify period of iron oxides dissolution linked to environmental acidification. Here, magnetic techniques such as magnetic susceptibility and isothermal remanent magnetization are applied to two marine sections encompassing the KPg (Zumaia, Spain) and PETM (Egypt, GSSP) transitions, in order to provide new insights to identify period of severe environmental changes in the geological record and their link to magmatic activity.

The magnetic results obtained for both sections, Zumaia and Dababiya, correlate with biostratigraphic, mineralogical and geochemical data from previous studies at different sections worldwide, demonstrating not only the reliability of the data as well as the global dimension of both events. The data obtained for Zumaia supports an important climate event preceding the KPg boundary. Volcanic markers like magnetite dissolution previously identified in Bidart and Gubbio are confirmed here in the case of the Zumaia section. Magnetite depletion also corroborates the presence of akaganéite and Mercury at Zumaia to support the volcanic theory. On a global scale, these markers correlate with global warming, an increase in atmospheric CO_2, environmental acidification via acid rains and presence of high stress opportunistic planctik foraminifera blooms. This climate perturbation also corresponds to the age of the main Deccan eruptions, recently dated by U-P method on zircon, reinforcing the link with the Deccan traps. In contrary to the KPg transition, the PETM at Dababiya is characterized by an increase in magnetite content, which is interpreted as the dissolution of carbonate and relative enrichment in detrital materials (clays). In addition, high concentration of goethite is observed along the section, specially above the PETM, where an increase in biological productivity is observed (Khozyem et al., 2015). In the PETM interval goetite decreases considerably. Goethite content at Dababiya is interpreted as the diagenetic oxidation of pirite and thus an indicator of anoxia during PETM. The increase in magnetite and decrease in goethite at the PETM also correlates with higher ratios of V/Cr, indicative of anoxic conditions (Khozyem et al., 2015). The high magnetite/low goetite interval at Dababiya also correlates with the Carbon Isotope Excursion (CIE) minimum that characterizes the PETM and with a calcite and foraminifera disappearance, supporting an ocean acidification starting below the PE boundary. Mercury enrichments in the same interval, together with negative excursions of $^{187}Os/^{188}Os$, supports the role of volcanism (NAIP) to initiate the concomitant warming and sea level rise that mark the PETM.

Comparasion of the magnetic properties of the KPg and PETM highlight different climate processes: dissolution of detrital magnetite onland in the case of KPg point environmental acidification by acid rains, whereas ocean acidification due to methane release and subsequent carbonate dissolution characterized the PETM. These findings provide new clues to identify climate and environmental acidification in the geological record and improve our understanding of future anthropogenic climate changes.

Key-Words: Cretaceous-Paleogene Mass Extinction, Paleocene-Eocene Thermal Maximum, Environmental Magnetism, Paleoclimate changes, Acidification.

Resumo

Ao longo da sua evolução, a Terra tem experienciado importantes mudanças climáticas que por vezes ocorrem de forma gradual ao longo de milhões de anos, mas por outras, de forma abrupta e repentina a escalas de tempo mais curtas, deixando marcas severas no registo geológico. Este projeto foca-se em dois grandes eventos climáticos da história da Terra: a extinção em massa do Cretácico-Paleogénico (KPg) e o pico térmico do Paleocénico-Eocénico (PETM), ocorridos há aproximadamente 66 e 56 Ma, respetivamente.

O final do período Cretácico é assinalado pela segunda maior extinção da história da Terra, que levou ao desaparecimento de dois terços das espécies existentes (Courtillot, 2003). As mudanças climáticas que estão na origem desta extinção têm sido apontadas como sendo resultado de dois grandes eventos catastróficos distintos, mas que ocorreram no mesmo curto espaço de tempo: o impacto meteorítico de Chicxulub (México) e as erupções vulcânicas do Decão (Índia). A contribuição, individual ou conjunta, de cada um destes eventos para a extinção em massa é ainda um assunto controverso e de intenso debate dentro da comunidade científica.

A teoria do impacto meteorítico, formulada por Alvarez et al. (1980), além da ocorrência global de um nível de Irídio, é suportada pela existência de uma enorme cratera na Península do Yucatán datada do final do Cretácico e ainda, pela ocorrência de microtectites, quartzo de impacto e espinelas ricas em Ni em diversos depósitos do KPg. Contudo, esta teoria não explica a natureza seletiva da extinção e a sua variabilidade geográfica bem como o decréscimo da diversidade de espécies observado antes da fronteira Cretácico-Paleogénico (Keller et al., 1993, 1995, 2011). Ainda assim, esta teoria continua a ser a mais aceite, especialmente fora da comunidade científica, devido à sua grande popularidade.

Na última década, as erupções do Decão têm sido grande alvo de estudo por parte de diversos autores (Chenet et al. 2007; Font et al., 2011; Keller et al., 2014; Schoene et al., 2014; Renne et al., 2015), os quais mostraram existir uma relação clara entre o princípio da extinção e o vulcanismo. Na verdade, a província magmática do Decão constitui um dos maiores episódios vulcânicos da história da Terra. Estima-se que as escoadas tenham coberto uma área de 1,5 milhões de km^2 e que tenham sido expelidos 1,2 milhões km^3 de lava (Keller, 2014). Datações recentes com base nas razões U-Pb em zircões e $^{40}Ar/^{39}Ar$ em plagióclases mostraram que as erupções do Decão terão sofrido uma transição de um período de elevada frequência/baixo volume para um período de erupções de baixa frequência/elevado volume, durante o qual 80-90% do total das erupções terá ocorrido num espaço de tempo muito curto (753 ± 38 kyr), o qual não terá permitido um reequilíbrio por parte dos ecossistemas terrestres levando à extinção do final do Cretácico (Schoene et al., 2014; Renne et al., 2015).

Tal como no KPg, também o intervalo que acompanha a transição do PE é assinalado por mudanças ambientais globais e abruptas. No final do Paleocénico, a Terra terá sofrido um aumento bastante significativo da temperatura tendo o oceano profundo atingido um aumento de 6ºC e o oceano superficial um aumento entre 5 e 8ºC (Zachos et al., 2006; Saleh, 2013). Este pico térmico do Paleocénico-Eocénico (PETM) coincide com uma anomalia (-2 a -7‰) da razão isotópica de carbono ($\delta^{13}C$), o que mostra ter existido um *input* rápido de uma grande quantidade de ^{13}C no sistema oceano-atmosfera. Tal, terá levado a uma intensificação do efeito de estufa e, consequentemente, ao aquecimento global do planeta. O pico térmico do PE gerou uma série de desequilíbrios entre os ecossistemas terrestres levando à alteração dos padrões globais de precipitação, vegetação, circulação atmosférica e oceânica, ao aumento da salinidade, diminuição do pH e do oxigénio dissolvido na água dos oceanos e, ainda, à extinção de algumas espécies de foraminíferos bentónicos e a uma diversificação de alguns foraminíferos planctónicos (Alegrete t al., 2009; Luciani et al., 2007).

A teoria mais aceite para explicar o PETM é a de que o vulcanismo associado à abertura do Atlântico Norte terá provocado um aumento da temperatura dos oceanos, conduzindo à destabilização de clatratos presentes nos sedimentos marinhos, libertando quantidades catastróficas de metano. A libertação deste metano terá levado à acidificação dos oceanos e contribuído para o aumento do CO_2 atmosférico. Apesar de o aquecimento global atual estar a acontecer a taxas superiores às verificadas no PETM, as semelhanças entre estes dois eventos tornam o PETM um bom análogo para testar modelos climáticos de previsão das alterações atuais.

Uma abordagem recente que combina dados de mineralogia com as propriedades magnéticas das rochas tem-se mostrado eficaz no reconhecimento de períodos de dissolução de óxidos de ferro durante episódios de acidificação ambiental. Neste projecto são aplicadas técnicas magnéticas em duas secções marinhas do KPg e PETM, Zumaia (Espanha) e Dababiya (Egipto), respectivamente: (1) suscetibilidade magnética (SM), que permite avaliar a contribuição de partículas dia-, para- e ferromagnéticas; (2) dependência da suscetibilidade face à frequência (K_{fd}), que permite averiguar a presença de partículas ultrafinas (<0.03μm), típicas de processos de alteração em carbonatos; (3) magnetização remanescente isotérmica (IRM), a qual permite diferenciar os principais minerais ferromagnéticos presentes numa dada amostra; e, por último (4) curvas de reversão de primeira ordem (FORC), utilizadas neste trabalho para averiguar a existência de biomagnetite.

Litologicamente, a secção de Zumaia alberga sedimentos hemipelágicos de idade Maastrichtiana, essencialmente margas intercaladas com diversos depósitos turbidíticos, e Daniana, fundamentalmente calcários. Em Dababiya, os sedimentos Paleocénicos formam maioritariamente margas e xistos margosos enquanto os sedimentos do Eocénico formam essencialmente, argilitos ou margas com uma forte componente siltítica.

Os resultados magnéticos obtidos para ambas as secções correlacionam-se com dados biostratigráficos, mineralógicos e geoquímicos de diferentes secções do globo, demonstrando não só a confiabilidade dos dados como também a dimensão global dos dois eventos. Os dados mostraram existir uma forte relação entre a SM e a litologia, indicando que a SM é essencialmente controlada pelo balanço entre o *input* detrítico e a produção de carbonatos.

Os resultados de Zumaia mostram uma redução da concentração da magnetite (detrítica e biogénica) num intervalo que se estende desde os 50 cm antes da fronteira KPg até aos primeiros centímetros do Daniano. Estes resultados corroboram estudos anteriores desenvolvidos em Gubbio e Bidart, onde um intervalo de baixa SM e uma redução no conteúdo em magnetite foram também detetados abaixo da fronteira do KPg (Lowrie et al., 1990; Font et al., 2011, 2014; Abrajevitch et al., 2015). Diversos *proxies* como a akaganéite, Hg, CO_2 atmosférico, paleotemperatura e $^{187}Os/^{188}Os$ da água dos oceanos, relacionam o intervalo de baixa SM encontrado em Zumaia com um episódio de vulcanismo intenso que, de acordo com as datações recentes (Schoene et al., 2014; Renne et al., 2015) terá correspondido ao vulcanismo do Decão. A atuação de chuvas ácidas, resultantes do intenso vulcanismo, explica a dissolução da magnetite detrítica e a ocorrência de uma acidificação ambiental que, por sua vez, terá contribuído para alterações na química da água e/ou nos sedimentos, destabilizando o limite óxico-anóxico e, consequentemente, o desenvolvimento de magnetite biogénica. Os resultados magnéticos de Zumaia corroboram a existência de um importante evento climático ocorrido durante o final do Maastrichtiano, mostrando que a extinção poderá ter tido inicio antes do impacto meteorítico.

Ao contrário da transição do KPg, a secção do PETM em Dababiya é caracterizada por um aumento do conteúdo de magnetite, o qual é interpretado como resultado da dissolução de carbonatos e aumento relativo das componentes detríticas. Ao longo de toda a secção, existe uma grande concentração de goetite, especialmente acima do intervalo do PETM, onde é também observado um aumento da

produtividade biológica (Khozyem et al., 2015). No intervalo do PETM a concentração de goetite é bastante menor. Em Dababiya, esta goetite foi interpretada como sendo resultado da oxidação da pirite e mostrou ser um bom indicador de anoxia durante o PETM. O aumento de magnetite e diminuição de goetite no PETM correlacionam-se com elevados valores da razão V/Cr típicos de condições anóxicas (Khozyem et al., 2015). O intervalo de elevada magnetite/baixa goetite correlaiona-se ainda com os valores mínimos da excursão isotópica de carbono que caracteriza o PETM e com o desaparecimento de calcite e foraminíferos, corroborando a ocorrência de uma acidificação ambiental com início antes da fronteira Paleocénico-Eocénico. Anomalias de mercúrio apresentadas neste trabalho em conjunto com excursões negativas da razão $^{187}Os/^{188}Os$ reportadas em sedimentos marinhos no Atlântico Norte, corroboram o papel do vulcanismo (NAIP) como mecanismo desencadeador do aumento de temperatura e aumento do nível médio do mar que marcam o início do PETM.

A comparação entre propriedades magnéticas do KPg e do PETM sugerem diferentes processos climáticos: no caso do KPg, a dissolução da magnetite detrítica no continente aponta para a ocorrência de acidificação ambiental devido à actuação de chuvas ácidas, enquanto no PETM se verifica apenas acidificação do oceano devido à libertação de metano, o que terá levado à dissolução de carbonatos. Estas novos dados oferecem pistas importantes para identificar eventos de acidificação no registo geológico e também novas pistas para compreender as futuras alterações climáticas do Antropocénico.

Palavras-chave: Extinção em Massa do Cretácico-Paleogénico, Pico Térmico do Paleocénico-Eocénico, Magnetismo Ambiental, Alterações Paleoclimáticas, Acidificação.

Contents

Figures List

Tables List

Acronyms List

B1/2 – Mean coercivity force

CCD – Calcite compensation depht

CIE – Carbon isotope excursion

CLG – Cumulative log-Gaussian

DP – Dispersion parameter

Fm - Formation

FORC – First order reversal curves

GAP – Gradient acquisition plot

GSSP - Global Stratotype Section and Point

H – Magnetic field

Hf – High frequency

ICS - International Commission for Stratigraphy

IRM – Isothermal Remanent Magnetization

J – Induced magnetization

k – Magnetic susceptibility

K_{fd} – Frequency dependent susceptibility

KPg – Cretaceous/Paleogene

LAP – Linear acquisition plot

Lf – Low frequency

LIP – Large Igneous province

MD – Multi domain

NAIP – North atlantic igneous province

NRM – Natural Remanent Magnetization

PE – Paleocene-Eocene

PETM – Paleocene/Eocene Thermal Maximum

PSD – Pseudo-single domain

RSS – Residual sum squared

SAP – Standardized acquisition plot

SD – Single domain

SF – Smoothing factor

SGG - Skew generalized Gaussian

SIRM – Isothermal remanent magnetization of saturation

SP - Superparamagnetic

VSM – Vibrating sample magnetometer

1. Introduction

The Earth temperature and weather patterns changed naturally over time scales ranging from decades, to hundreds of thousands, to millions of years (Ruddiman, 2008). In some cases, these changes are gradual but in others abrupt. This project focuses on the two global and abrupt climate changes that occurred at the Cretaceous-Paleogene (KPg) and at the Paleocene-Eocene (PE) transitions, at approximately 66 and 56 Ma, respectively.

The KPg boundary is marked by a clay layer that points out the end of the Mesozoic and the beginning of the Cenozoic Eras. In the end of Cretaceous period, an abrupt climatic event occurred, leading to the extinction of the dinosaurs, several mammals, ammonites and many other terrestrial and marine species including a considerable number of smaller and less familiar organisms that constitute the marine plankton. This severe mass extinction is the second largest in Earth history, where two-thirds of the species were extincted (Courtillot, 2003).

Two catastrophic events, the Chicxulub asteroid impact and the Deccan Traps eruptions, have been associated to the climate changes that culminated in the KPg mass extinction. However, how each of these catastrophes contributed to the mass extinction, either by itself or in combination, and whether they were coincident in time are still under debate (Abrajevitch et al., 2015; Keller, 2014).

The impact theory, formulated by Alvarez et al. (1980), became very popular after the discovery of an Iridium and other platinum-group elements anomaly in deep-sea limestones exposed in Italy, Denmark and New Zealand. According to the author, the impact of a large Earth-crossing asteroid would inject about 60 times the object's mass into the atmosphere as pulverized rock. A fraction of this dust would remain in the stratosphere for several years and would be then distributed worldwide. The resulting darkness would suppress photosynthesis leading to a great mass extinction (Alvarez et al., 1980). This hypothesis is supported by the presence of impact-derived microtektites, shocked quartz grains and Ni-rich spinels in KPg boundary deposits, as well as the discovery of a giant impact crater on the Yucatán Peninsula, Mexico. Some authors (Smith & Hertogene, 1980; Schulte et al., 2010) have claimed the Chicxulub impact to be the only cause for the mass extinction. However, despite the existence of such apparently obvious coincidence, this hypothesis fails to explain the selective nature of the mass extinction, its geographically variable patterns, and a long-term decline in species diversity prior to the KPg boundary (Keller et al., 1993, 1995, 2011).

Therefore, due to its huge magnitude, some scientists pointed the Deccan volcanism as the main cause of the extinction (Courtillot et al., 1986; Keller et al., 2012). Moreover, three of the five big mass extinctions in Earth's history are consequence of large and rapid volcanic eruptions (Permian-Triassic, Triassic-Jurassic, and end-Devonian), suggesting that large igneous provinces (LIP) could have been the general cause of mass extinctions (Courtillot & Renne, 2003). Actually, the LIP of Deccan is one of the major volcanic episodes in Earth's history, covering most of India with an estimated superficie of 1.5 million km^2 and 1.2 million km^3 of extruded lava. Today, with about two thirds eroded or buried, the lava exposures still cover an area the size of France (Keller, 2014).

Several factors such as the popularity of the impact theory, the belief that Deccan volcanism occurred over a long period (leaving sufficient time for recovery between eruptions) and the absence of data that directly linked the mass extinction with Deccan volcanism in India made the acceptance of Deccan volcanism as the cause (or at least the major contributor) for the mass extinction very challenging. However, the intense research of LIP's over the last few years, especially on the Deccan Traps, provided

new insights about the role of volcanism in the KPg extinction (Abrajevitch et al., 2015; Punekar et al., 2016; Chenet et al., 2007, 2008, 2009; Font et al., 2011, 2014, 2016; Keller et al., 2008, 2009a, 2009b, 2009c, 2011, 2012).

Detailed paleomagnetic studies combined with $^{40}K/^{40}Ar$ (Chenet et al., 2007, 2008, 2009) of Deccan lava flows revealed three main volcanic phases of relatively short durations (Figure 1.1): Phase-1, -2 and -3 with a respectively mean age of 67.5 Ma, 65±0.3 Ma, and 64.7 Ma. Phase-2, is indicated to be responsible for nearly 80% of the total Deccan eruptions and to occur in a very short period (just a few hundred thousand years, or less) coincident with the KPg boundary, suggesting that Deccan volcanism had a major role in the end-Cretaceous mass extinction (Chenet et al., 2007, 2008, 2009). However, age uncertainties of such data are larger than the estimated total duration of Deccan Traps and thus, the onset and duration of volcanism cannot be precisely compared to geological, extinction or environmental records from sedimentary sections spanning the KPg. Based on U-Pb dating zircon Schoene et al. (2014) calculated a duration of 753 ± 38 kyr for an estimated 80-90% of the total eruptive volume of the Deccan Traps, with age uncertainties 1-2 orders of magnitude smaller than previous works. More recently, Renne et al. (2015) combined $^{40}Ar/^{39}Ar$ dating of igneous plagioclase with U-Pb zircon dating from Schoene et al. (2014) and suggest that Deccan volcanism did not had three different phases but a transition from high-frequency, low-volume eruptions to low-frequency, high-volume eruptions instead. The closer temporal coincidence of such transition and the Chicxulub impact (50 kyr) suggest that strong seismic waves produced by the impact could have triggered increased volcanism (Renne et al., 2015).

The cumulative effect of these huge and rapid volcanic eruptions may have led to global climate and environmental changes by the injection of stratospheric acid aerosols, ozone depletions, acid rain and superficial ocean acidification. The critical global effects induced by the Deccan are not expected to have occurred at the onset of the first eruptions, but at the time when increased eruption rates and volumes reached a critical threshold, starting to affect climate, the environment and life on Earth (Font et al., 2018).

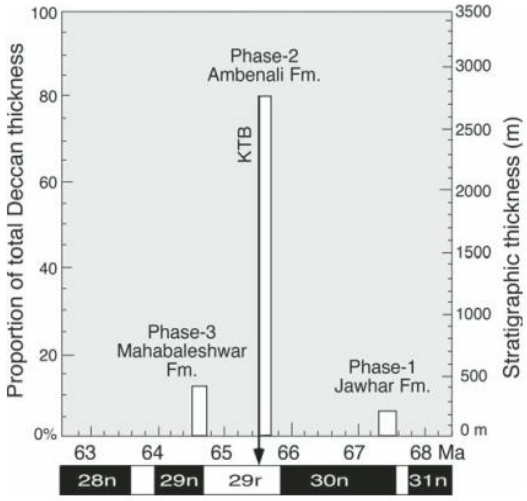

Figure 1.1 – Relative thickness of Deccan lava flows in each of three phases of volcanic eruptions calculated by Chenet et al. (2007) as percent of total Deccan Trap thickness. Ages are based on paleomagnetic time scale. (Keller, 2014).

The huge volumes of lava and specially the enormous sulphur content released were more than able to lead to the KPg extinctions (Chenet et al., 2007). However, the Chicxulub asteroid impact theory should not be disregarded. Only the KPg extinction coincides with both a large impact and one of the largest

volcanic episodes in Earth's History, which makes it difficult to distinguish the role of each event. Some authors believe that each process is unlikely to have caused a global biological collapse individually, preferring a scenario of multiple causes (Keller et al., 2009; Renne et al., 2013). The main challenge for the scientific community is to separate the consequences of these two coeval events. In addition, the timing of both catastrophic event is too short to be elucidated by radiometric dating but can be investigated in the stratigraphic record. In several sections worldwide. Keller et al. (2011) show significant changes in planctik foraminifera, including dwarfing and test dissolution, in the Upper Maastrichtian CF1 and CF2 biozones, just below the Iridium-rich layer, and interpreted as the result of ocean acidification linked to the Deccan traps activity. In Bidart and Gubbio, Font et al., (2014, 2016) show that the presence of a low magnetic susceptibility interval, including mercury anomalies and presence of akaganéite, in the CF1 biozone, consistent with environmental acidification induced by Deccan traps eruptions. Abrajevitch et al. (2015) showed that the low magnetic susceptibility interval in Bidart and Gubbio corresponds to a drastic decrease in detrital magnetite and biogenic magnetite formed by magnetotatic bacteria, interpreted as the result of dissolution by acid rain onland and change in seawater chemistry, respectively. These data suggest that the climate perturbations induced by the Deccan traps initiated shortly before the Chicxulub impact. However, this hypothesis has now to be tested in other sections, as it is the objective here in Zumaia.

The interval near the Paleocene-Eocene transition at 55.8±0.2 Ma (Westerhold et al., 2009), also known as Paleocene-Eocene Thermal Maximum (PETM), is marked by global and sudden environmental changes. Isotopic data revealed that a rapid warming started in the late Paleocene, with deep sea temperatures rising 6ºC and sea surface temperatures rising at least 8ºC in the poles and 5ºC in the tropics (Zachos et al., 2006; Saleh, 2013). Precipitation and vegetation patterns dramatically altered worldwide, and both atmospheric and oceanic circulation were perturbed (Foreman et al., 2012).

This abrupt global warming, firstly recognized by Kennet and Stott (1991), is marked by a large (-2 to -7‰) negative carbon isotope excursion (CIE) in marine and terrestrial sediments (Kender et al., 2012). This negative shift in the carbon isotope ratio ($\delta^{13}C$) reflects a rapid release of ^{13}C-depleted carbon into the ocean-atmosphere system due to a massive and rapid injection of greenhouse gases (CH_4 and/or CO_2). The approximate mass of Carbon released has been estimated to be more than 2000 Gt (Dickens et al., 1997) and possibly as high as 4500 Gt (Zachos et al., 2005).

The most acceptable scenario to explain the PETM event is the catastrofic methane release from clathrates. Solid clathrates, contain ^{13}C-depleted methane and water and, are stored in deep-sea sediments along the continental margin where its stabilization as hydrate requires high pressure and relatively low temperature. A small increase in temperature, a decrease in pressure or a sea level change is enough to destabilize the clathrates which might escape from the seafloor and be rapidly oxidized to CO_2 in the water column or atmosphere. The most likely cause for the destabilization of clathrates in the PETM was an ocean warming due to the North Atlantic Igneous Province (NAIP) volcanism. An enormous input of mantle-derived carbon linked to the opening of the North Atlantic Ocean is also possible because evidence exist for massive volcanism close to the PETM . However, it remains uncertain whether volcanism could have produced CO_2 at a rate recquired for rapid global environmental change (Sluijs et al., 2007).

Other scenarios have been proposed to explain the massive injection of CO_2 in both marine and atmospheric ecosystems such as (1) the extensive burning of Palaeocene peat and coal deposits linked with the arid period that prevailed during the latest Palaeocene; (2) the release of thermogenic methane from Cretaceous-Paleocene mudstones in the North Atlantic, linked to hydrothermal injection in

organic-rich sediments; (3) the drying of isolated epicontinental seas, leading to dessication and rapid oxidation of organic matter and (4) melting of the methane-rich permafrost (Khozyem et al., 2013).

The environmental perturbations associated with the global temperature rise, such as increasing sea water salinity and drop in pH and dissolved oxygen, led to major species extinctions (35-50%) in deep marine benthic foraminifera (Alegret et al., 2009), but diversification in planktic foraminifera with subtropical affinities (Luciani et al., 2007). In the terrestrial realm, it led to the diversification of modern mammal species and their migration across the northern continents (Bowen et al., 2002). The PETM is also marked by an increase in kaolinite content in marine sediments throughout the Tethys region, which was associated with a change to warm and humid conditions that would have led to the intensification of chemical leaching (Bolle et al., 2000). Because the length of time taken to form kaolinite is 10^6 years, Kemp et al. (2016) indicates the kaolinite anomaly to be the result of an intensified hydrological regime that caused extensive erosion of pre-existing kaolinite-bearing soils and regolith (Kemp et al., 2016).

The mechanism and rate by which the excess of carbon was removed from the atmosphere and oceans is ambiguous and is still under debate (Bains et al., 2000; Torfstein et al., 2010). One of the most proeminent hypothesis is that the termination of the PETM crisis was a response to a sharp increase in the intensity of the marine and terrestrial biological productivity, resulting in the drawdown of atmospheric CO_2 and subsequent carbon sequestration in the ocean (Bains et al., 2000). However, Torfstein et al. (2010) showed that the export production did not rapidly remove excess carbon from the atmophere and indicated the silicate wethering as the most likely mechanism for carbon removal, which operates at much lower rates.

The PETM and KPg warming have been caused by a sudden greenhouse gas emissions, similary to today's anthropogenic warming. Although the current warming has been running at much faster rates, the ressemblances between these events make the KPg and specially the PETM excellent analogues to test modelling studies in order to forecast the actual climate change. In contrast to the KPg sections where rock magnetic properties provide interesting indicators or environmental accidification, rock magnetism has been poorly tested in the case of the PETM hitherto.

This project aims to apply environmental magnetic methods such as magnetic susceptibility (MS) and isothermal remanent magnetization (IRM) on reference marine sections encompassing the KPg and PE transitions at Zumaia (Spain) and Dababiya (Egypt), respectively. The applied techniques will provide new insights to identify periods of severe environmental change (acidification) in the global sedimentary record as well as new constrains about the origin and timing of both climate events. Furthermore, the study of the PETM and KPg sections will bring insight into the response of the Earth's climate to the anthropogenic carbon emissions expected in the near future.

2. Geological Setting and Sampling

2.1 The KPg transition at Zumaia (Spain)

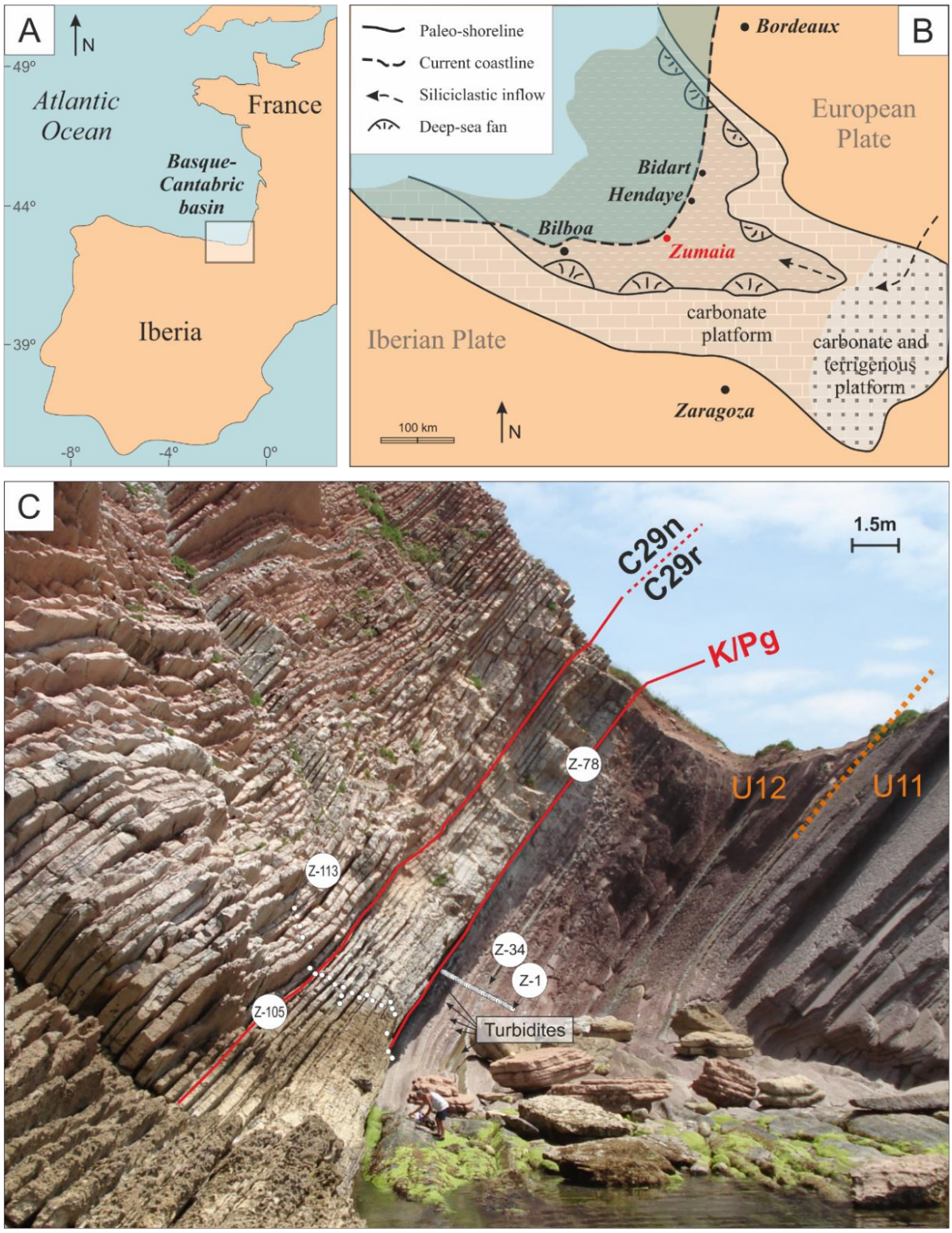

Figure 2.1 – A) Location map of the studied area in the Basque-Cantabric basin. B) Paleoenvironmental context of the Zumaia section. C) Field photograph of the Zumaia section and location of the collected samples. Position of the KPg and 29r/29n chron boundaries are also shown. (Modified from Font et al., 2018).

The Zumaia section is located in the Basque country at the Bay of Biscay and it crops out at the Itzurun beach (42º18.00'N/ 2º15.30'W) in north-western Spain, slightly north of Zumaia village (Figure 2.1 A, B). The Zumaia area is structurally a part of the synclinorium of Bilbao and sedimentologically it forms part of the Basque-Cantabric basin (Ten Kate & Sprenger, 1993). The Basque-Cantabric basin was a deep-water E-W trending interplate trough (flysch trough), flanked by shallow shelf areas to the north (Aquitania), south (Iberia) and east (Pyrenees), and opening westward into the Bay of Biscay (Dinarès-Turrel et al., 2013). This interplate trough was formed in the Early Campanian, as smaller basins from previous rifting stages joined at the start of the Pyrenean convergence (Batenburg et al., 2012). Throughout the Late Maastrichtian and Paleocene the sea transgressed the shallow flanking areas, leading to the development of extensive ramps, or carbonate platforms. This wholesale transgression also mades it difficult for coarse-grained siliciclastic deposits to reach the deep trough, which became the site of a hemipelagic limestone/marl type of sedimentation (Dinarès-Turrel et al., 2013). In a major tectonic phase during the Eocene (40-50 Ma), when the African and European continents collided, the sedimentary pile of the basin was folded and faulted but the stratigraphic sequences are easily recognizable in the field (Ten Kate & Sprenger, 1993; Pérez-Rodríguez et al., 2012).

The Zumaia section, as the Bidart and the Hendaye coastal sections (Figure 2.1B), consists of Late Cretaceous to Early Paleogene thick hemipelagic sequences of alternating marls and limestones, deposited at an estimated water depth of 800-1500 m, in which a minor amount of turbidites are intercalated (Batemburg et al., 2012). These coastal cliffs form a classical site for paleo, magneto, bio and cyclostratigraphic studies. The alternation between marls and limestones in the sequences underlying and overlying the KPg boundary was attributed to astronomical cycles in the Milankovitch band. Several cyclostratigraphic studies focusing on physical and geochemical parameters in combination with detailed biomagnetostratigraphic analysis, identified precession cycles of 21 kyr, short eccentricity cycles of 100 kyr, long eccentricity cycles of 405 kyr, obliquity modulation cycles of 1.2 Myr and very long eccentricity modulation cycles of 2.8 Myr (Payros et al., 2016).

The Maastrichtian succession at Zumaia is about 240 m thick, very well exposed and stratigraphically continuous. The bulk of the Maastrichtian strata corresponds to the Zumaia-Algorri Formation in which four main lithofacies can be recognized: 1) marls, which can be thinly bedded to massive, and vary in color from reddish or purple to brown, depending on the burial and diagenetic history of the section; 2) limestone-marl rhythmites of varying thickness, but with most couplets attaining thickness of 30 cm or less; 3) massive limestones; and 4) isolated distal turbidites interbedded with the above lithologies, which can occur as either single or multiple distal turbidites (Ward and Kennedy, 1993).

Based on the varying proportions of these lithologies, two different lithological classifications were proposed. Wiedmann (1988) subdivided the Maastrichtian strata exposed at Zumaia into three main assemblages: (1) a lower Maastrichtian turbidite assemblage, deposited during an interval of increased subsidence (Pérez-Rodriguéz et al., 2012); (2) a middle turbidite assemblage of turbidites grading upward into limestone-marl sequences and (3) an upper Maastrichtian sequence characterized by relative tectonic stability (Pérez-Rodriguéz et al., 2012) containing interbedded marls and more resistant limestones. These three subdivisions were further subdivided into 12 lithological units (Figure 2.2). Only unit 12 is part of the sampled section (Figure 2.1C).

On the other hand, Ward & Kennedy (1993) divided the Maastrichtian strata into five formal members from the lowest (I) to highest (V):

- Member I is 90 m thick and it is composed of thin couplets of limestone and marl with bed thicknesses usually between 5 and 15 cm. In the lower parts of the member, thin interbedded distal turbidites occur. This member corresponds to Wiedmann´s Units 2-5.

- Member II is 15 m thick and is composed of thick massive micritic limestones which show bed thicknesses averaging 0.2-0.4 m, with the thickest beds approaching a meter in thickness. These limestones differ from the limestones above and below by the virtual lack of interbedded marls. This member corresponds to Wiedmann´s Unit 6 and it forms the most prominent marker unit in the Zumaia-Algorri Formation.

- Member III corresponds to Wiedmann´s Unit 7 and it is composed almost entirely of very thinly bedded marl units with occasional thin distal turbidites. The color range is distinctive, from red to purple, appearing to be diagenetically controlled and related to depth of burial. This member is about 10-25 m thick, deeply eroded, and contains numerous faults.

- Member IV is composed of grey limestones interbedded with marls. The limestones can reach up to 1 m thick but are generally thinner. Member IV is a limestone-marl member, with 80 m in thickness, which varies in appearance depending on the amount of limestones. In the lower part of the member, the rhythmicity is predominated by limestones, so that the unit is massive and usually well exposed in steep cliffs. This limestone-dominated portion of the member corresponds to Wiedmann´s Units 8 and 9 and it is succeeded by a marlier portion (Wiedmann's Unit 10), resulting in more recessive coastlines. An upper, again more massive, calcareous portion makes up the top of the member and it corresponds to Unit 11 of Wiedmann.

- Finally, Member V corresponds to Wiedmann´s Unit 12 making up the highest Maastrichtian strata in the Bay of Biscay region. It contains the sampled section and it is composed of massive reddish and sporadically grey marls with some single sandy turbidites interbedded (Font et al., 2018). This member is about 15 m thick at Zumaia and it contains a very small calcareous component.

Figure 2.2 – Panoramic view of the outcrop in the Punta Aitzgorri cliffs, showing the 12 lithological units proposed by Wiedmann (1988). Pérez-Rodríguez et al. (2012).

The KPg boundary was specifically established at the base of the dark clay layer in the El Kef section (Tunisia). It is a yellowish red thin bed with relevant evidence of a meteorite impact. Although the KPg boundary clay layer is not present, the impact extinction event is very well recorded at Zumaia where the lithological boundary between the Maastrichtian and the Danian is marked by a level of secondary calcite (Meléndez & Molina, 2008; Font et al., 2018).

Immediately following the KPg transition, during the Danian, there was an even more dramatic reduction in siliciclastic influx into the basin which resulted in the deposition of pink coccolith limestones (Ward & Kennedy, 1993). The Danian stage is about 50 m thick at Zumaia and its sediments

belong to the Aitzgorri and Itzurun Formations. Only Aitzgorri Fm is part of the sampled section. These Formations are mainly composed of regular alternations of hemipelagic indurated limestones, marlstones and marls. In the Aitzgorri Fm the limestones dominate, whereas in the Itzurun Fm, the proportions of the three lithologies vary considerably. In addition, both formations include minor but significant amounts of thinbedded turbidites. The transition between the two formations is marked by an abrupt lithologic change, which is interpreted as the expression of the prominent sea level fall that characterized the end of Danian across the whole basin (Bernaola et al., 2009).

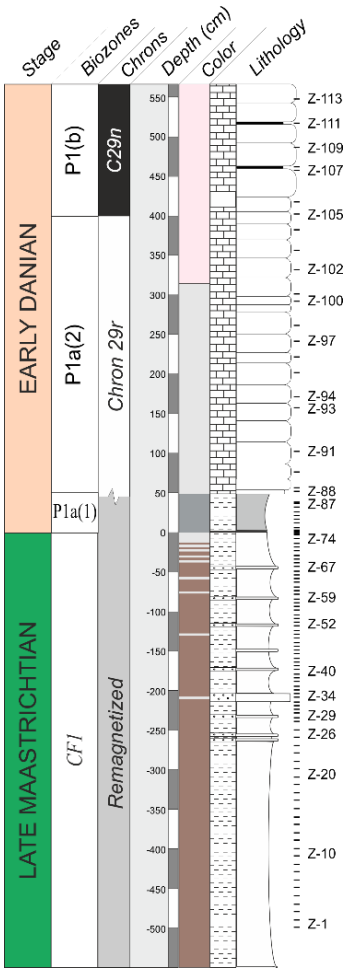

Bernaola et al. (2009) subdivided the Aitzgorri and Itzurn formations into a series of informal members. The Aitzgorri Fm is largely pink-reddish in color and was subdivided in two members: (1) a "crowded" member which is 7 m thick and consists of amalgamated limestones or limestones with very thin interbedded marls and, (2) a "stratified" member which is 9 m thick and overlies the "crowded" member. This member takes its name from the well-developed bedding and obvious contrast between limestones and intervening marlstones. The Itzurun Fm shows higher vertical variations in both the relative proportions of hemipelagic sediments and the amount of turbidite intercalations. In contrast to the Aitzgorri Fm, dark to light grey colors dominate the Itzurun Fm. However, the base of the formation is defined by a 5.5 m thick interval of marls and marlstones of a characteristic red color (Bernaola et al., 2009).

Two set of samples from Zumaia were collected by Dr. Eric Font and Dr. Thierry Adatte in 2015. A total of 113 samples (labelled Z) were collected from 5.5 m above to 5 m below the KPg boundary with a sample spacing of 5-10 cm (Figure 2.1 C; Figure 2.3). A second set of 454 rock fragments (labelled ZU) was collected from 3 m above to 2.42 m below the KPg boundary, based on sample spacing of 1-3 cm, for high resolution magnetic property analysis.

Biostratigraphic and magnetostratigraphic constrains shown in Figure 2.3 are from Dinarès-Turrel et al. (2003) and Font et al. (2018).

Figure 2.3 – Log of the sampled section showing the Cretaceous-Paleogene boundary and bio, magneto and lithostratigraphic information. The location of the samples is also shown. (Modified from Font et al., 2018).

2.2 The Paleocene-Eocene Thermal Maximum at Dababiya (Egypt)

The Dababiya section is located at the eastern side of the upper Nile Valley, near Dababiya village, 35 km southeast of Luxor City (25º30' N, 32º31' E), Egypt (Figure 2.4).

The Paleocene-Eocene transition in the southern margin of the Tethys in Egypt includes the outer-shelf deposits of northeast Egypt and Sinai. In the eastern desert the monocline of the Upper Cretaceous to Upper Eocene resulted in uplift and exposure of the outer shelf to marginal marine strata across the desert in northeastern Egypt where they are exposed in mesas and ridges (Khozyem et al., 2015). The

Dababiya section is one of these exposures. It is a composite section consisting of four partial, stratigraphically overlapping sections namely DBA, DBE, DBH and DBD (Berggren & Ouda, 2003) (Figure 2.5B).

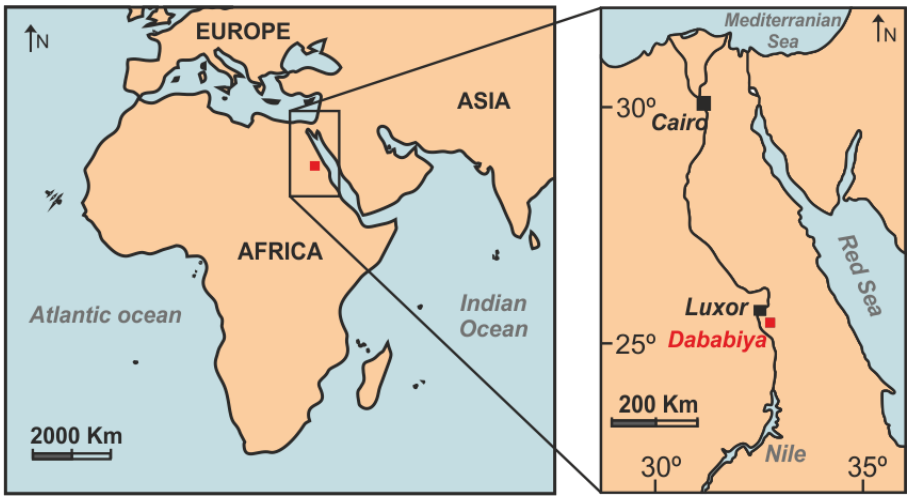

Figure 2.4 – Location map of Dababiya section.

The area corresponds to an old and abandoned quarry of limestones, shales and marls, which provides a remarkable three-dimensional view in some outcrops (Figure 2.5). Limestones were quarried in Pharaonic times and used in the construction of the temples of Luxor and Karnak. Shales and marls were extensively excavated, probably for bricks (Despuis et al., 2003) until the beginning of the XXI century.

In addition to the clear-cut exposure, the Dababiya section also provides a detailed record of lithologic, mineralogic, biotic and geochemical events that were associated with the PETM. Therefore, the International Comission of Stratigraphy (ICS) designated, in 2003, the Dababiya outcrop (section DBH) as the Global Stratotype Section and Point (GSSP) for the Paleocene-Eocene boundary.

Four main lithostratigraphic Formations are exposed in Dababiya's area range: Dakhla, Tarawan, Esna and Thebes, from older to younger, respectively (Figure 2.5).

The Dakhla Formation in Dababiya area is limited to a few meters (~7m) in thickness (Berggren & Ouda, 2003) and is composed of a dark-grayish to grayish green shale, with 60 to 80% of carbonate content (Despuis et al., 2003). Sometimes, it is reddish and ferruginated, with thin veinlets of anhydrite. The base of the section is covered by rock debris and wind-blown sands (Berggren & Ouda, 2003).

The Tarawan Formation is composed of a snow-white to grayish white, indurated chalk that grades upward into yellowish marly limestones. It contains, locally, thin brownish chert bands, which do not exceed 3 cm in thickness and are usually dissected by a network of calcite veinlets (Berggren & Ouda, 2003). The total thickness of this Formation at Dababiya is 21.5 m and, except in the upper part, where stratification is absent. The carbonate content is high (~85% average) in the lower part of the Tarawan limestone. Approximately, halfway through the section there is only 60-70% of carbonate content and then, it decreases drastically, thereby marking the transition to the Esna Formation (Despuis et al., 2003).

The Esna Formation is ~130 m thick at Dababiya (Despuis et al., 2003). It consists of a grayish and greenish gray laminated shale and brown marls. The lowermost part of the section encloses a thin band (~2 m thick) of laminated, partly coprolite-rich, phosphatic shale grading upward into calcareous shales

and marls. This interval overlies a thin dark gray clayey horizon (~0,75 m thick) and underlies a highly fossiliferous detrital limestone of calcarenitic nature (1 m thick) (Berggren & Ouda, 2003).

Despuis et al. (2003) divided the Esna Formation into three main units based on carbonate content: Esna-1, Esna-2 and Esna-3. Only Esna-1 and Esna-2 are exposed in GSSP outcrop.

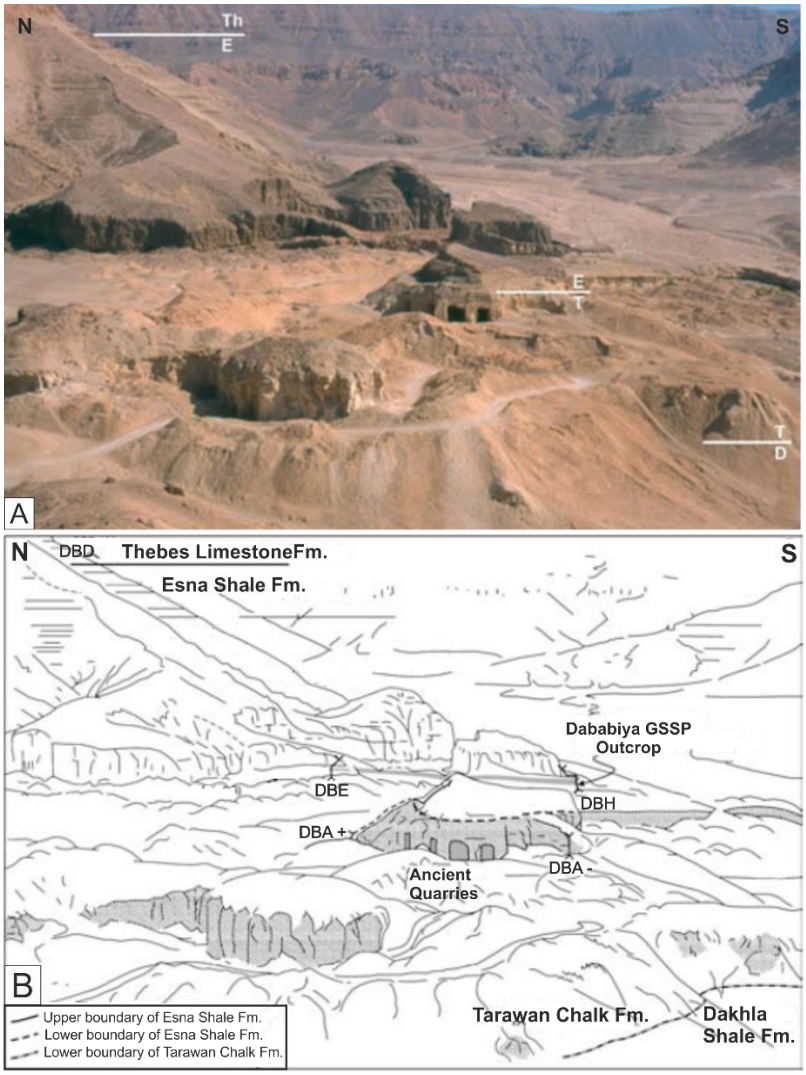

Figure 2.5 – A) Oblique east-facing view of the outcrops in the Dababiya Quarry as seen from the hill immediately to the north of the village of Dababiya. B) Sketch outlining the exposures of the main lithostratigraphic units: Dakhla Shales, Tarawan Chalk, Esna Shale and Thebes Limestone and the four partial sections DBA, DBD, DBE and DBH (P/E GSSP) are shown (modified from Aubry et al., 2007).

The lower Unit Esna-1 is ~7 m thick and it is composed of gray shales containing variable amounts of carbonate. It extends from the base of the Esna Shale up to the contact with the dark clay (Berggren & Ouda, 2003) that defines the limit between units Esna-1 and Esna-2 and also the P/E boundary, which was defined based on the following criteria (Saleh, H., 2013): (1) the negative organic carbon isotope excursion (CIE), (2) the extinction of deep water benthic foraminifera (*Stensioina beccariiformis*), (3) the transient occurrence of planktonic foraminifera (*Acarinina Africana, A. sibaiyaensis, Morozovella allisonensis*) during the $\delta^{13}C$ excursion, (4) the transient occurrence of the *Rhomboaster* spp. – *Discoaster araneus* nannofossils assemblage and (5) an acme of the dinoflagellate *Apectodiniu*.

The middle unit, Esna-2, is ~70 m thick. The first 5 m of Esna-2 are composed of a singular succession of five lithologies designated by Despuis et al. (2003) as The Dababiya Quarry Beds. The remaining 65 m of Esna-2 are essentially clayey, rather dark in color, without prominent bedding and with carbonate content that never exceeds 50%. Despuis et al. (2003) described the Dababiya Quarry Beds cropping out in DBH section:

- Bed 1 is 0.63 m thick and it is composed of dark laminated non-calcareous clay with a few phosphatic coprolites (0.5 cm diameter) at the base. There is a substantial increase (from 7% to 11-14%) in quartz at the base of Dababiya Quarry Beds. The quartz content progressively increases upwards in Bed 1 to 32% at the top.

- Bed 2 is 0.50 m thick and is a phosphatic (~14% apatite) brown shale with numerous phosphatic coprolites with 0.5 cm diameter. It is characterized by an increase in carbonate content (up to 30%) coupled with a decrease in quartz content to about 18%.

- Bed 3 is 0.84 m thick and corresponds to a cream-colored, laminated phosphatic shale with sparse phosphatic coprolites (0.5 cm diameter) and numerous lens-like and pale phosphate inclusions (1 cm diameter). The apatite content in this bed varies between 12% at the base and 8% near the top. Coprolites are essentially absent in this unit, which means that the high apatite content cannot be explained by the coprolite accumulation so, another phosphorus bearer should be presented. The carbonate content decreases upward in the bed from 18% to 12%. The base of the bed is locally marked by concretions of iron oxides, anhydrite and jarosite, interpreted as weathering products of pyrite nodules.

- Bed 4 is 0.71 m thick and it is composed of grey shale with an increasing carbonate content (from 40% to 50%) and decreasing contents of quartz (from 12% to 6%) and apatite (from ~6% to 3%).

- Bed 5 is 1 m thick and corresponds to a marly calcarenitic limestone. The highest carbonate content (67%) of the Dababiya Quarry Beds is recorded at the base of this bed, whose contact with Bed 4 is unbioturbated. The high carbonate contents coincide with low apatite and quartz contents, ~1% and 5%, respectively.

The upper unit of Esna Formation, Esna-3, which is not exposed in GSSP outcrop, is ~ 45 m thick consisting of an alternation of marls, marly limestones and limestones with very thin shale intercalations. Compared to Esna-2, this interval has a lighter color and a higher carbonate content (Despuis et. al., 2003). Berggren & Ouda (2003) describe this unit as being characterized by limestone stringers that become increasingly common, thicker and more indurated upwards. Iron and phosphatic rods and incrustations are commonly scattered throughout the unit. The foraminiferal content and preservation vary widely from common to barren and from fair to very good, respectively.

The boundary between Esna-3 and Thebes Formation is marked by a prominent 1 m thick limestone bed containing 90% of carbonate. There has been some controversy over the placement of this boundary. According to Berggren & Ouda (2003), Unit Esna 3 has been attributed to the Thebes Formation by some researchers. However, the lithology, faunal content and depositional environment of this unit support strongly its inclusion in the Esna Formation. The most acceptable placement of the boundary is the one proposed by Said (1960), who placed it at the base of the massive limestone bed.

The Thebes Formation is ~290 m thick and consists of massive and partly chalky limestones, occasionally thin-bedded, containing bands and nodules of chert at the base and *Nummulites* and *Operculina* banks at the top. This Formation has been divided into three members: (1) a lower Hamidat Member, 55 m thick, that consist of thinly bedded limestone containing chert bands and nodules, (2) a middle Dababiya Member of massive snow-white chalky limestone rich in *Nummulites*, *Operculina* and *Assilina*, 95 m thick, and (3) an upper El Shaghab Member, 60 m thick, composed of massive oyster limestone with echinoids and alveolinids (Berggren & Ouda, 2003).

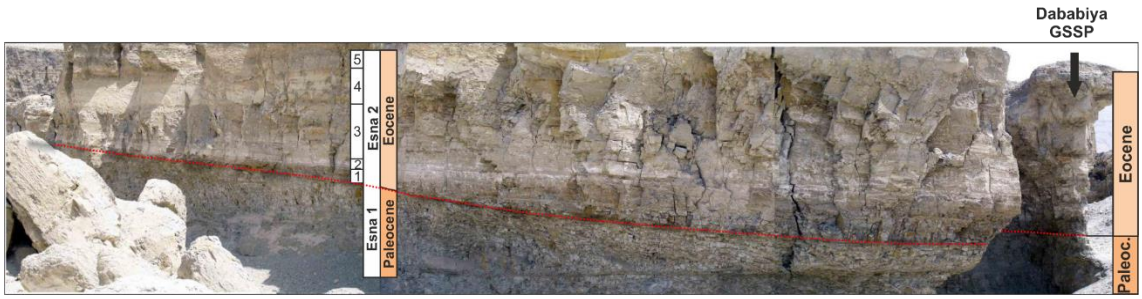

Figure 2.6 – Field photograph of the sampled section showing the PE boundary and beds of Esna-2 Unit. (Photo provided by Dr. Thierry Adatte).

Samples from Dababiya were supplied by Dr. Thierry Adatte who collected them in the context of the doctoral thesis of Hassan Saleh (Saleh, H., 2013). 54 samples (labelled Db) were provided, which were collected at 2 cm, 5 cm and 10 cm sample spacings spanning the Upper Paleocene to Lower Eocene interval.

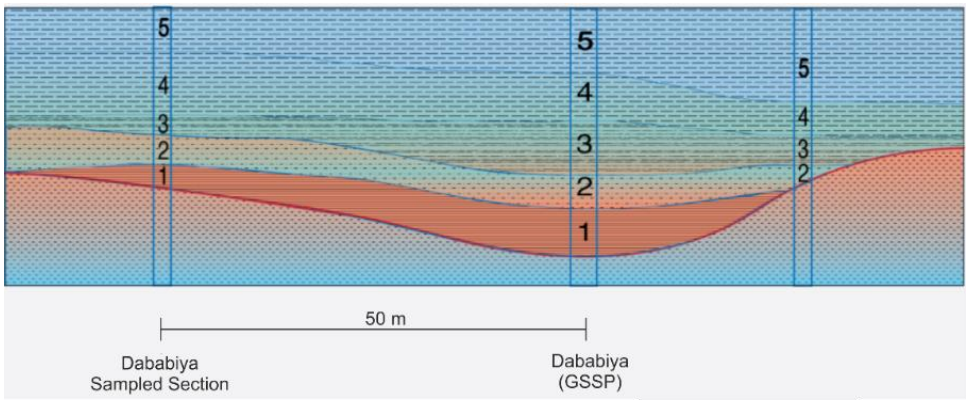

Figure 2.7 – Diagram illustrating the lateral disappearance of basal beds on either side of the main GSSP outcrop due to deposition in an asymmetric channel. (Modified from Saleh, 2013).

The Dababiya GSSP outcrop is not available for sampling because of its limited lateral exposure accessibility (just few tens of meters), the likely annihilation of the rock exposure due the oversampling and other political complications (Saleh, H., 2013). Therefore, the samples were collected on an identical sequence (Figure 2.6), 50 m to the left (NW) of the main GSSP outcrop. The basal beds of the GSSP outcrop were deposited in a submarine channel. Thus, because of the channel morphology, Esna-2 units in the sampled section are less thick than Esna-2 units in the GSSP outcrop (Figure 2.7) (Saleh, 2013).

Since no field work was carried out in this project, the lithological descriptions and the log (Figure 2.8) presented by Saleh (2013) were adopted. The sampled section consists of the late Paleocene marl to marly shale of Esna-1, a well-defined sequence boundary and the overlying early Eocene Esna-2 unit. Saleh (2013) divided Esna-2 into five beds with the following thickness and lithological characteristics:

- Bed 1: silty claystone with anhydrite layers; 0.32 m thickness.
- Bed 2: silty claystone with anhydrite layers; 0.48 m thickness.
- Bed 3: silty marl with phosphatic nodules and anhydrite; 0.24 m thickness.
- Bed 4: marl to marly limestone; 1.0 m thickness.
- Bed 5: only the basal 0.05 m were recovered and therefore it was difficult to describe lithology.

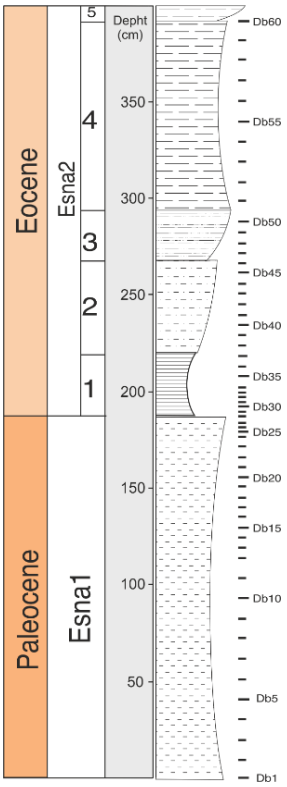

Figure 2.8 – Log of the sampled section showing the Paleocene-Eocene boundary and location of the samples (Modified from Saleh, 2013).

3. Methods

Before the application of magnetic methods, mass was measured for each sample with a precision of 10^{-3} g. Both sets of samples, Z and Db, were previously crushed by using an agate mortar at the University of Lausanne.

3.1 Magnetic Susceptibility

All materials tend to be magnetized when a magnetic field is applied. The magnetization acquired for each material (Induced Magnetization, J) is proportional to the magnetic field (H), as shown in equation 3.1. However, different materials will acquire different values of J for the same H. This is due to the fact that some minerals have greater capacity than others to acquire magnetization. This ability is called Magnetic Susceptibility (*k*) and it is a physical property inherent to each mineral. Therefore, *k* is a constant of proportionality between J and H and it can be defined as a measure of the ease with which a material can be magnetized (Thompson & Oldfield, 1986) when a magnetic field is applied.

$$J = kH \tag{3.1}$$

Magnetic susceptibility can be expressed as a function of the volume being, in that case, a dimensionless property, or as a function of the mass, which the units are m^3/kg.

k values of the samples (Z and Db) were measured at the Institute Dom Luís Laboratory with an MFK1 Kappa Bridge susceptometer, manufactured by AGICO, at the frequency F1 (976 Hz) and reported relative to mass.

Magnetic susceptibility depends on the concentration of the magnetizable material in a sample and on the composition of that material namely mineralogy, grain size and shape. Magnetizable materials in sediments are comprised of not only ferrimagnetic minerals such as the iron oxide minerals magnetite and maghemite, and iron sulfide and sulfate minerals, like pyrrhotite and greigite, but also other less magnetic compounds, including paramagnetic ones. The important paramagnetic minerals in sediments are the clays (predominantly chlorite, smectite and illite), ferromagnesian silicates (such as biotite, pyroxene and amphiboles), iron sulfides (such as pyrite and marcasite), iron carbonates (including siderite and ankerite) and other iron and magnesium bearing minerals. In addition to ferrimagnetic and paramagnetic, there may be an abundance of diamagnetic compounds such as calcite, quartz and organic matter. Diamagnetic materials typically acquire a very weak negative *k* when a magnetic field is applied, i.e., their acquired *k* is opposed to the magnetic field applied. Consequently, the presence of diamagnetic minerals reduces the *k* in a sample. However, since the *k* magnitude in diamagnetic minerals is so weak compared to paramagnetic and ferromagnetic minerals, the diamagnetic contribution is generally negligible (Ellwood et al., 2003, 2008).

Magnetic susceptibility profiles are typically the combination of two signals: a high-frequency, low-amplitude cyclic signal and an irregular low-frequency, high-amplitude signal. The first one may be due to weathering, secondary alteration and metamorphism in sedimentary sequences (Ellwood, 2008). The second one is dominated by eustasy and climate variations (Milankovitch cycles), where high-amplitude, low frequency *k* variations result from transgressive and regressive sea-level fluctuations. When the sea-level drops, the base level falls and erosion increases, thus more detrital grains are sent to the marine environment producing high *k* values (Crick et al., 2001; Ellwood et al., 2003; Correia, J., 2010).

3.2 Frequency Dependent Susceptibility

The frequency dependent susceptibility (K_{fd}) method is used to evaluate the presence of ultrafine (<0.03 μm) superparamagnetic (SP) particles in a sample. Superparamagnetic particles are ferrimagnetic minerals produced largely by biochemical processes in soils (Dearing, J. A., 1994) or by chemical alteration. For exemple, chemical remagnetization in carbonates generally result in significant SP content (Jackson, 1990; Jackson et al., 1992, 1993; Channell and McCabe, 1994; Font et al., 2006). Therefore, K_{fd} is an indicator of chemical alteration of carbonates in the case of the Zumaia and Dababiya sections studied here. Measurements of K_{fd} involve making two *k* readings in magnetic fields created at two different frequencies: Low (*Lf*) and High (*Hf*) frequencies.

A low frequency measurement allows the SP crystals to behave as ferromagnetic minerals fully contributing to the MS signal. At high frequency, the SP crystals acquire a paramagnetic behavior. Since SP crystals lose their magnetization in a very short period of time (about 1/10000th of a second) when the induced magnetic field is removed, a sample without SP crystals would show the same *k* in the two frequencies. On the other hand, samples with SP crystals would show slightly lower values at high frequency than at low frequency (Dearing, J. A., 1994).

The K_{fd} index formula (equation 3.2) expressed as a percentage of the original *Lf* reading and the interpretations of K_{fd} values (Table 3.1) were proposed by Dearing (1994):

$$K_{fd}\,(\%) = \frac{Lf - Hf}{Lf} \times\ 100 \tag{3.2}$$

Table 3.1 – Interpretation of frequency dependent susceptibility values.

K_{fd} (%)		**Interpretation**
Low	< 2.0	Virtually no SP grains (<10%)
Medium	2.0 – 10.0	Admixture of SP and coarser non-SP grains, or SP grains <0.005 μm
High	10.0 – 14.0	Virtually all (>75%) SP grains
Very High	> 14.0	Rare values, erroneous measurement, weak sample or contamination

The *k* values of the samples (Z and Db) were measured at the Institute Dom Luís Laboratory with a MFK1 Kappa Bridge susceptometer at the frequencies F1 (976 Hz) and F3 (15616 Hz) corresponding to the low and high frequencies, respectively. Negative and very high values (>14%) of K_{fd} were considered to be erroneous. Therefore, they were eliminated and are not presented in the results.

3.3 Isothermal Remanent Magnetization curves

In contrary to magnetic susceptibility, which includes the relative contribution of para-, dia- and ferromagnetic particles, Isothermal Remanent Magnetization (IRM) only reflect the contribution of ferromagnetic particles. IRM is the magnetization acquired by a sample when submitted to an induced magnetic field, at constant temperature. In this method, a known volume sample is subjected to a progressively increasing unidirectional magnetic field (in mT). After each increase in the applied field, the sample is removed, and its magnetization (in A/m) is measured (Robertson & France, 1994).

Several iron oxides may be simultaneously present in a natural sample. For example, hematite, goethite and magnetite are very common in sedimentary rocks. Different minerals show different coercivity values so, only the ferromagnetic minerals with lower coercivity than the applied field will be magnetized in each step. Consequently, only high field values will be able to magnetize very coercive particles, such as goethite. An example of an IRM curve is shown in Figure 3.1. The IRM curve provides two crucial informations: the values of the magnetization at saturation (SIRM), which is proportional to the concentration of ferromagnetic particles, and the coercivity ($B_{1/2}$), which is characteristic of the nature of the ferromagnetic particles (ex. Magnetite, hematite, goethite).

In cases of mixed magnetic mineralogy, Robertson & France (1994) observed experimentally that the IRM acquisition curves of individual minerals follow a cumulative log-Gaussian (CLG) function. An IRM curve can therefore be decomposed into several CLG curves, which can be individually characterized by three important parameters: magnetization of saturation (SIRM), mean coercivity force ($B_{1/2}$), that is the field needed to induce half of the saturation, and the dispersion parameter (DP), given by one standard deviation of the logarithmic distribution (Kruiver et al., 2001). The DP is generally related to the distribution of grain sizes.

IRM is very sensitive to ferro/ferromagnetic and antiferromagnetic particles, even in very low amounts (Font et al., 2014), which allows the identification of the types of iron oxide minerals present in a sample. Egli (2003, 2004) identified a series of common magnetic components, presented in table 3.2.

Table 3.2 – Common magnetic components and its typical IRM parameter values (Egli, 2003, 2004).

Components	Log $B_{1/2}$	DP
Pedogenic and extracellular magnetite	1.34	0.34
Detrital Magnetite	1.46	0.36
Low-coercivity magnetofossils	1.64	0.19
High-coercivity magnetofossils	1.85	0.15
Hematite	2.30	0.27
Goethite	3.30	0.25

The types of iron oxide minerals present in natural materials may be used to correlate sedimentary horizons with other horizons or sources, to evaluate on the nature of chemical processes accompanying sedimentation in certain environments and to detect changes in sedimentary environment often related to climate changes (Robertson & France, 1994; Kruiver et al., 2001).

Before IRM acquisition procedures, Db sprayed samples and ZU rock fragments, were put into cubic plastic boxes of 8 cm^3 with special care to ensure there were no contaminations. All analyzed samples were demagnetized with a LDA-3A AF demagnetizer (AGICO) to avoid any initial remanent magnetization. IRM curves were posteriorly acquired by the application of a magnetic field that was gradually increased up to a maximum peak of 1.2 T using an IM-10-30 impulse magnetizer. The acquired magnetization at each step was measured with a JR6 spinner magnetometer. All the procedures were carried out at the Institute Dom Luís Laboratory.

Finally, IRM curves were analyzed using a cumulative Log-Gaussian function, with the software developed by Kruiver et al. (2001) and the Max UnMix program developed by Maxbauer et al. (2016).

The Kruiver et al. (2001) method is based on the assumption that an IRM acquisition curve follows a CLG function and it is accessible for readers to use through download of an excel workbook. The analysis of the IRM acquisition curves is done by converting the field values in their logarithmic values and plotting them versus: (i) the acquisition curve on a linear scale, (ii) the acquisition curve expressed as a gradient and (iii) the acquisition curve on a probability scale (Figure 3.1). The analysis of IRM acquisition curves on a linear ordinate scale is referred to as LAP (Linear Acquisition Plot), as a gradient as GAP (Gradient Acquisition Plot) and, on a probability scale as SAP (Standardized Acquisition Plot). The combined analysis of LAP, GAP and SAP is referred to as CLG analysis (Kruiver et al., 2001).

Plotting an IRM acquisition curve in this way is visually appealing because a unimodal distribution will be representing by a straight line (Figure 3.1). When the data points do not plot on a linear path it means that the acquisition curve needs to be fitted with more than one component.

With the combination of the three plots, it is possible to obtain a robust determination of the magnetic components. Initial SIRM values can be easily estimated from the LAP and, the GAP provides initial values for $\log(B_{1/2})$ and DP. The modelled LAP, GAP and SAP are compared and fitted to the data. The adequateness of the fit is expressed by the sum of the squared differences between the data and the model (squared residuals) for each plot. The values for SIRM, $\log(B_{1/2})$ and DP are optimized interactively by minimizing these squared residuals. This method discriminates on the basis of different mineral coercivity. Therefore, additional rock-magnetic tests are still required to separate minerals with similar coercivities (Kruiver et al., 2001).

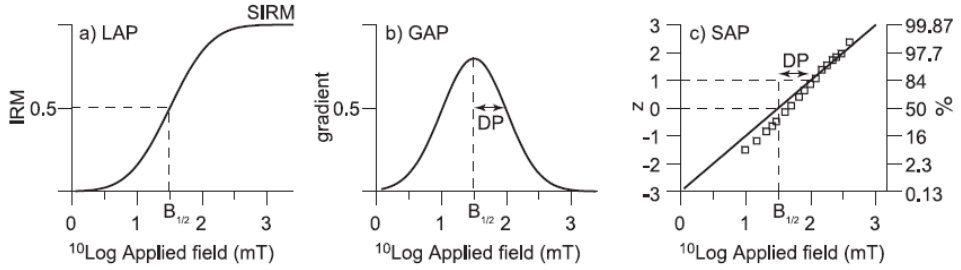

Figure 3.1 – Representation of a) LAP, b) GAP and c) SAP. The squares are an example of a natural sample of a single magnetic mineral (titanomagnetite) and as such the data plot is a straight line (Kruiver et al., 2001).

The Kruiver et al. (2001) software also calculates, from de IRM acquisition curve, the expected S-ratio for the modelled components. Two S-ratio definitions are given as output:

(1) The classical definition: $-IRM_{-0.3T}/IRM_{1T}$
(2) The Bloemendal et al. (1992) definition: $(1 - \frac{IRM_{-0.3T}}{IRM_{1T}})/2$

In this project it will be used the normalized definition of Bloemendal et al. (1992). The interpretation of S-ratio, which can vary from 0 to 1, is based on the tendency of the coercivity to vary significantly with magnetic mineralogy. Ferrimagnetic minerals such as magnetite have considerably lower coercivities than the antiferromagnetic minerals goethite and hematite. Consequently, higher (lower) S-ratio values reflect higher (lower) proportions of magnetite to the high coercivity minerals hematite and/or goethite (Bloemendal et al., 1992).

The Max UnMix program is a web application built using the shiny package for R studio. As the Kruiver et al. (2001) method, it is used for un-mix coercivity distributions derived from magnetization curves.

However, Max UnMix is designed to be user friendly, it runs as an independent website, and it is platform independent (Maxbauer et al., 2016).

The Kruiver et al. (2001) method assumes that an IRM acquisition curve follows a CLG function. However, it is known that many natural samples contain magnetic mineral components whose coercivities are not log-normal (Maxbauer et al., 2016). Instead of CLG function, the Max UnMix program uses a skew generalized Gaussian (SGG) function, introduced by Egli (2003). The SGG function has major advantages over simple Gaussian distributions because it can better account for non-normal behavior that is common in natural samples. Deviations from normality can dictate the need for additional normal or log-normal components within a model to achieve a satisfactory fit, whereas a single skew component may prove sufficient (Maxbauer et al., 2016).

The analysis with the Max UnMix program is done in three simple steps: fitting, optimization and error analysis. The fitting is a subjective process achieved through an interactive interface where the user selects the initial model parameters (mean coercivity, dispersion, relative proportion and skewness) with slider bar inputs. This should be done with caution and consideration for known parameters values of magnetic minerals compounds. The optimization of the initial parameters is achieved using the optim() function, which iteratively determines the ideal values of initial parameters to minimize the residual sum squared (RSS) between the observed and the modeled coercivity distribution (see, Maxbauer et al., 2016, for details). In order to determine the number of magnetic minerals components the Max UnMix application allows F-tests to be performed on models with a variable number of components. It is also possible to calculate the relative contribution of each component. In the error analysis, a resampling routine is used to assign uncertainties to the optimized model parameters and resultant modeled coercivity. For a user-defined number of resampling events, the model calculates newly optimized values based on a Monte-Carlo method. The final set of results provides users with a robust sense of uncertainty and model quality.

3.4 Forc diagrams

First-order reversal curve (FORC) diagrams are used to understand magnetization processes in fine magnetic particle systems (Roberts et al., 2014). This technique was introduced in rock magnetism by Pike et al., (1999) and Roberts et al. (2000) and it provides a way to identify magnetic minerals and characterize their domain structures and interactions by measuring partial hysteresis curves.

The composition and grain-size distribution of magnetic minerals determine the overall magnetic properties of a rock or sediment and the stability of its natural remanent magnetization (NRM) through geological time. The smallest magnetic grains, containing only a single-domain (SD) and the SP particles, have the strongest and most stable remanence, producing the most reliable results in paleointensity studies. On the other hand, larger magnetic grains, multi-domain (MD), produce the least meaningful results. Pseudo-single-domain (PSD) grains are usually volumetrically dominant in a typical rock or sediment and they have a relatively strong and stable remanence. Comparing to SD and MD, PSD grains produce intermediate reliable results (Muxworthy & Dunlop, 2002).

A FORC is measured by progressively saturating a sample in a field H_{SAT}, decreasing the field to a value H_A, reversing and sweeping it back to H_{SAT} in a series of a regular field steps, H_B (Figure 3.2 (a)) (Gubbins & Herrero-Bervera, 2007). This process is repeated for about 100 different values of H_A, producing a series of FORCs (Figure 3.2 (b)). Hysteresis data represent the composite magnetic response of all particles within a sample, therefore providing a measure of the bulk magnetic properties of the

sample (Roberts et al., 2000). The measured magnetization at each step as a function of H_A and H_B gives an $M(H_A, H_B)$ that can be plotted as a function of H_A and H_B in the field space (Figure 3.2 (c)). The field steps are chosen in such a way that H_A and H_B are regularly spaced, which means that $M(H_A, H_B)$ can be plotted on a regular grid (Gubbins & Herrero-Bervera, 2007).

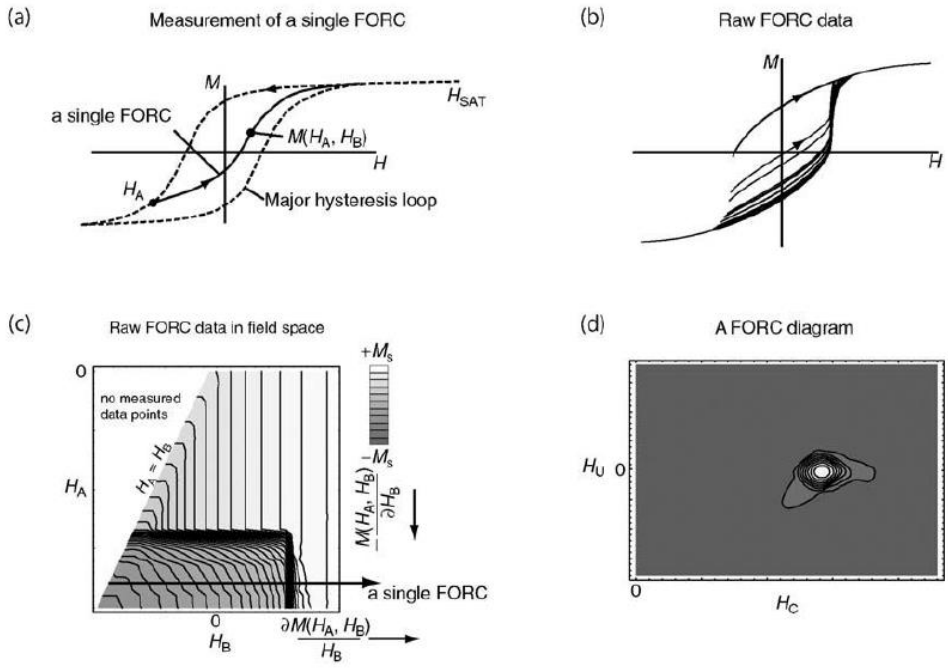

Figure 3.2 – Illustration of the construction of a FORC diagram. (Gubbins & Herrero-Bervera, 2007).

The FORC distribution $\rho(H_A, H_B)$ is defined as the mixed second derivative of the surface shown in Figure 3.2 (c):

$$\rho(H_A, H_B) = \frac{\partial^2 M(H_A, H_B)}{\partial H_A \partial H_B} \tag{3.3}$$

The FORC distribution $\rho(H_A, H_B)$ at a point P is calculated by fitting a polynomial surface on the square grid with P at the center. In order to reduce the effect of measurement noise, which is magnified by the second derivative, smoothing is required. The smoothing factor (SF) sets the size of the local square grid on which the polynomial fit of the magnetization is performed. The number of the points of the grid is $(2SF+1)^2$ (Carvallo et al., 2003).

The final FORC diagram is given by the contour plot of $\rho(H_A, H_B)$ (Figure 3.2 (d)). In this case, it is convenient to rotate the axes by changing coordinates from (H_A, H_B) to (H_C, H_U), where H_C is the coercivity $H_C = (H_B - H_A)/2$ and H_U is the magnetic interaction field distribution $H_U = (H_B + H_A)/2$ (Roberts et al., 2014).

Distinct domain structures and interactions of the particles result in different patterns of the final FORC diagram. An ideal noninteracting SD particle will have a FORC distribution that lies at $H_C = H_{SAT}$ and $H_U = 0$ (Figure 3.3 (a)). For assemblages of randomly orientated noninteracting SD grains, FORC diagrams will show a central peak due to the switching of the magnetization at H_{SAT}. This peak will show an asymmetric "boomerang" shape and there will be a negative region near the bottom left-hand

corner of the diagram (Figure 3.3 (b)). For interacting SD grains, H_C corresponds to the coercive force of each SD loop in the absence of interactions and H_U is the local interaction field H_I. When the ideal SD grain is affected by magnetic interactions, H_I will shift the switching field, resulting in a spreading in the H_U direction on a FORC diagram (Figure 3.3 (c)).

FORC diagrams for MD grains display a series of contours nearly parallel to the H_U axis (Figure 3.3 (d)). This pattern is similar to the one for interacting SD grains. However, instead of being due to inter-grain magnetostatic interaction fields, the spreading is caused by internal demagnetization fields (Gubbins & Herrero-Bervera, 2007). As PSD grains have an intermediate behavior, they display the closed peak structure typical of SD grains and the contours parallel to the H_U axis typical of MD grains (Figure 3.3 (e)).

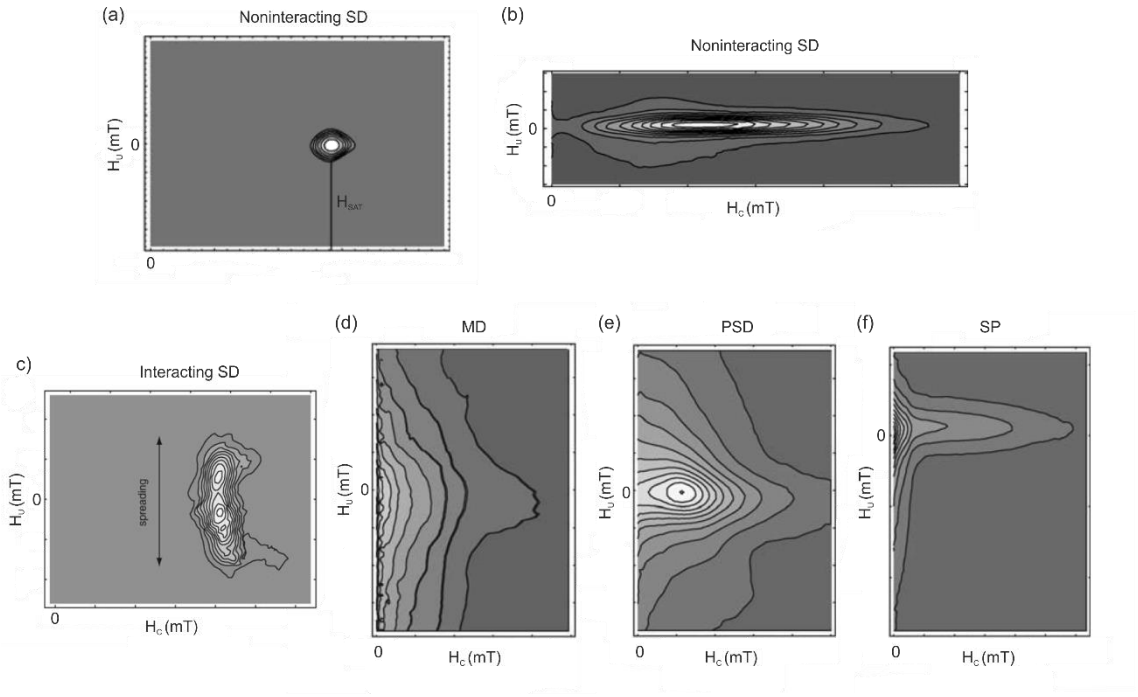

Figure 3.3 – Interpretation of the different patterns of FORC diagrams. (Modified from Gubbins & Herrero-Bervera, 2007).

SP grains will only manifest themselves on the FORC diagram if their relaxation time is of the same order as the averaging time. If the grains have shorter relaxation times ($H_{SAT} \to 0$), $\rho(H_A, H_B) = 0$ at all values (Roberts, 2000). FORC diagrams for the manifesting SP particles show a series of contours running parallel to the H_U axis and a pronounced peak along $H_U = 0$ (Figure 3.3 (f)) that can be similar to the one for noninteracting SD particles. However, the distinction can be easily made through the identification of thermal relaxation time by cooling a sample (Gubbins & Herrero-Bervera, 2007).

Ultrafine magnetic particles (SP and SD) can be used as paleoenvironmental tracers because they have an authigenic origin and they can also be an important source of a stable NRM. Magnetostatic bacteria synthetize chains of SD particles (magnetossomes) with extremely controlled sizes and shapes. Magnetossomes can be preserved over geological times as fossils. Magnetofossils have been found in a variety of marine and freshwater sediments and sedimentary rocks, where they can contribute with more than 60% to the saturation remanent magnetization. Magnetofossils are extremely useful in paleoenvironmental studies because they provide information about past geochemical conditions that favored growth of magnetotactic bacteria and/or that controlled the preservation or dissolution of magnetossomes (Egli et al., 2010).

FORC analysis were implement only for a few samples of Dababiya. The procedures were carried out by Alexandra Abrajevitch from the Department of Earth Sciences, Faculty of Sciences, Ehime University, Matsuyama City, Japan. Because of time constrains, low resolution FORCs were measured, with a vibrating sample magnetometer (VSM). A saturating field of 1T, an averaging time of 100 ms and a wait time of 1s between successive measurements were used. Each measurement run included 100 FORCs, measured with a field increment of 2.3 mT and were processed with an SF of 5. FORC measurement time for one sample was approximately 58 minutes. The results were processed using the algorithm of Zhao et al. (2015).

4. Results

4.1 The KPg transition at Zumaia

Mass specific magnetic susceptibility of the Z and ZU collections is illustrated in Figure 4.1 and 4.3, respectively. In both set of samples, the MS shows the same trend, conforting a reliable repeatability of the measurement. Mass specific magnetic susceptibility (m^3/kg) of the Zumaia section is strongly facies-dependent, as the magnetic signal is well correlated with the mineralogy (Font et al., 2018). In the case of the Z collection, MS varies from higher values ($5.9 - 12.9 \times 10^{-8}\ m^3/kg$) in Maastrichtian marls to lower values ($1.0 - 8.6\ \times 10^{-8}\ m^3/kg$) in the Danian limestones. A slight but significant gradual decrease in MS values can be observed 2 m below the K-Pg boundary (Figure 4.1). Negative shifts of MS data observed in the Maastrichtian correspond to turbidite layers (Figure 4.3). Because iron oxide content and grain size have no environmental significance in turbidites, these samples were further excluded from IRM analysis.

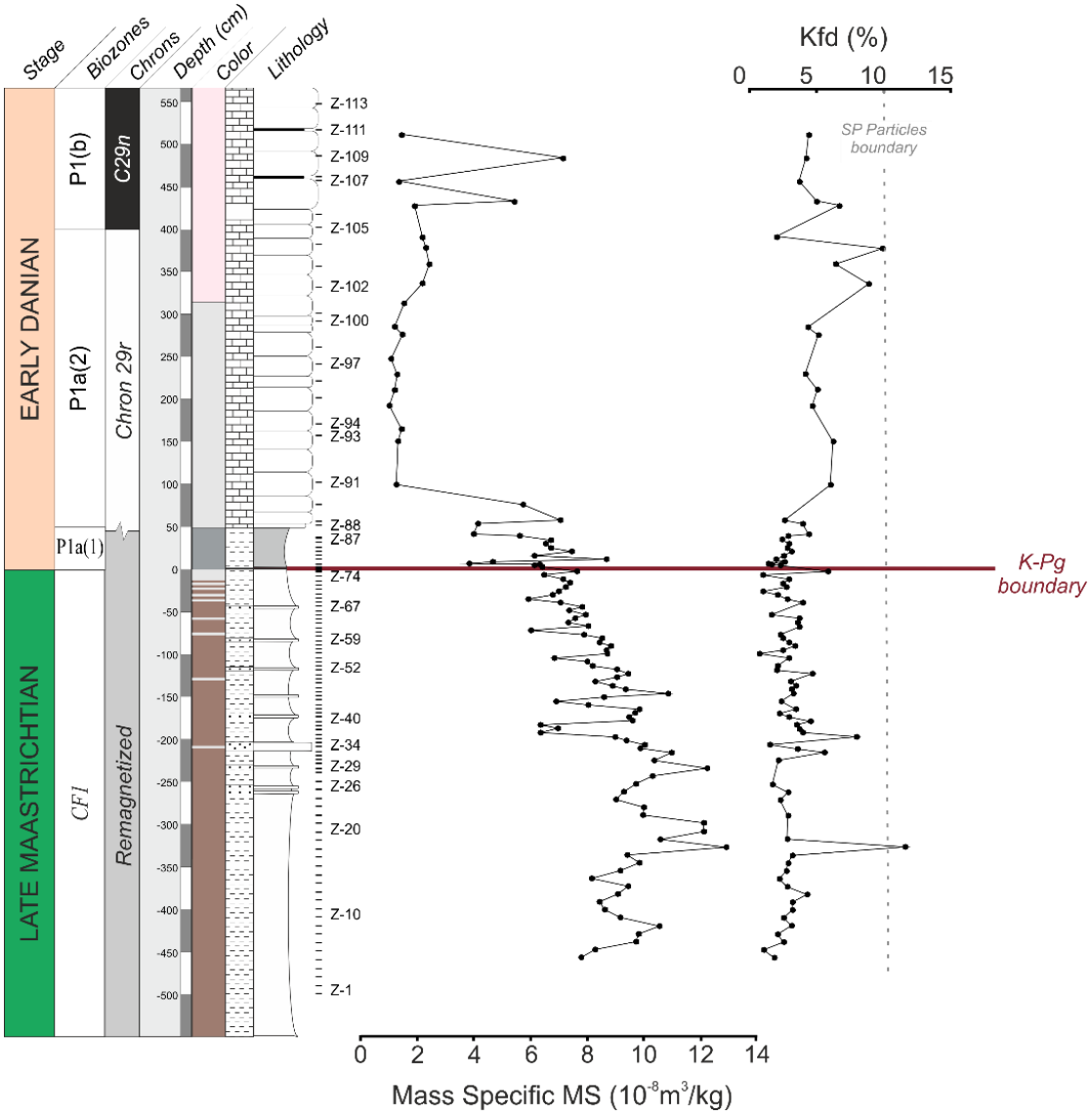

Figure 4.1 – Magnetic data (MS and K_{fd}) of Zumaia (collection Z). MS is the Magnetic susceptibility, expressed as a function of the mass (m^3/kg), and K_{fd} is the frequency-dependent magnetic susceptibility. Absolute values are reported in table 8.1.

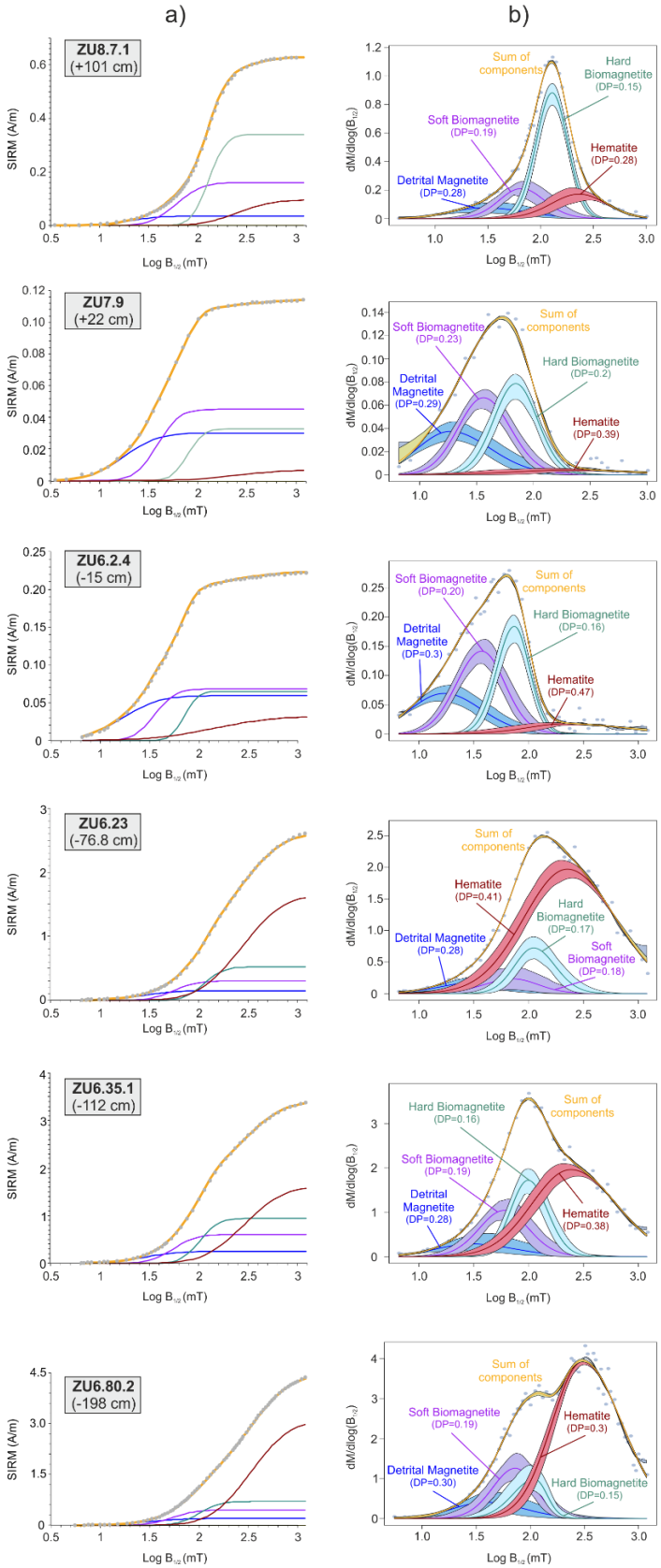

Figure 4.2 – a) Linear Acquisition plot of Isothermal Remanent Magnetization (IRM) curves of 6 representative samples of the Zumaia section (ZU collection), unmixed by using the Kruiver et al. (2001) software. b) Coercivity distribution (Gradient acquisition plot) derived from IRM curves obtained by using the MAX UnMix software (Maxbauer et al., 2016). The shaded area represents error envelopes of 95% confidence intervals.

Frequency-dependent susceptibility (K_{fd}) results of the Zumaia section (Z collection) are indicative of a very low SP particle contribution. K_{fd} values vary essentially between 2-10% (Figure 4.1), which is indicative of admixture of SP and coarser non-SP grains, or SP grains < 0.005 μm (Dearing, 1994). However, a significant number of samples range K_{fd} values between 0-2% revealing the absence of SP grains (Dearing, 1994). Such values indicate that there were no significant biochemical processes leading to rock alteration. Negative and very high values (>14%) of K_{fd} are generally considered to be erroneous (Dearing, 1994) and therefore were not considered in Figure 4.1. Moreover, values above sample Z-91 might not be significant, due to the very low susceptibility, which induces higher measurement errors.

IRM measurements were carried out for the high resolution ZU sample collection. The linear and gradient acquisition plots (LAP and GAP, respectively) of 6 samples, representative of the section, are presented in Figure 4.2. After unmixing IRM curves, four components were identified along the Zumaia section (Figures 4.2 and 4.3): detrital magnetite, soft biomagnetite, hard biomagnetite and hematite.

The LAP's of IRM curves (Figure 4.2 a) show that between samples ZU8.7.1 (+101 cm) and ZU6.2.4 (-15 cm) the contribution of hematite is considerably lower compared to the other components. However, below sample ZU6.23 (-76.8 cm) the contribution of hematite becomes higher and the total SIRM does not reach saturation. This is because hematite is a more coercive mineral than magnetite (Figure 4.2 b), which implies a higher applied magnetic field to reach saturation. The hematite is interpreted as a post-depositional component, probably responsible for the reddish color of the altered rocks and therefore, may not have an environmental significance.

Component 1 has logarithmic values of mean coercivity (Log $B_{1/2}$) ranging 1.2 – 1.47 mT and dispersion parameter (DP) values ranging from 0.28 to 0.35 mT, wich are typical of detrital magnetite (Figure 4.3) (Egli, 2004). Component 2 and Component 3 are both characterized by very small values of DP, essentially between 0.1 and 0.2 mT, wich is typical of biogenic magnetite. Component 2 shows typical values of soft biomagnetite and component 3 of hard biomagnetite. Finally, Component 4 has a Log $B_{1/2}$ values between 2.15 – 2.67 mT and DP values from 0.2 to 0.45 mT, typical of hematite.

The concentrations of detrital magnetite, biomagnetite (hard and soft) and hematite are proportional to their saturation remanent values (SIRM). SIRM values of each component are represented in Figures 4.2 and 4.3. The concentration of each component is dependent of the lithology. Danian carbonates have a lower abundance of magnetite and hematite than the Maastrichtian marls, because marls have a much more detrital affinity than carbonates. Components 1, 2 and 3 experience a gradual decrease in the upper Maastrichtian up to the K-Pg boundary. However, the abundance of hard biomagnetite decreases more abruptly in the last 50 cm below the K-Pg boundary, and reach values as low as those observed in the basal Danian sediments, including carbonates. Hematite decreases abruptly right below the K-Pg boundary and almost disappears in biozone P1a. As expected, Danian carbonates are characterized by very low SIRM values, due to the very low content of iron oxides. However, this low iron oxide content is not expected in the case of detrital material such as the marls of the top of the Maastrichtian. This suggests that iron oxides in this stratigraphic interval may have been affected by dissolution, possibly related to environmental or climate changes (i.e. anoxia or acidification).

The S-ratio parameter is indicative of the relative proportion between magnetite (low coercivity mineral) and hematite (high coercivity mineral). Therefore, values > 0.5 are indicative of a higher magnetite contribution and values < 0.5 are indicative of a higher hematite contribution for the total remanence of each sample. S-ratio values at Zumaia range from 0.65 to 0.98 (Figure 4.3), which indicates a higher

magnetite contribution along the entire section. However, this higher contribution of magnetite is much more significant in the Danian carbonates and in the top 15 cm of Maastrichtian marls, where S-ratio values are 0.80-0.90 (Figure 4.3). Below the -15 cm, the contribution of hematite equals approximately the contribution of magnetite, with S-ratio values around 0.65.

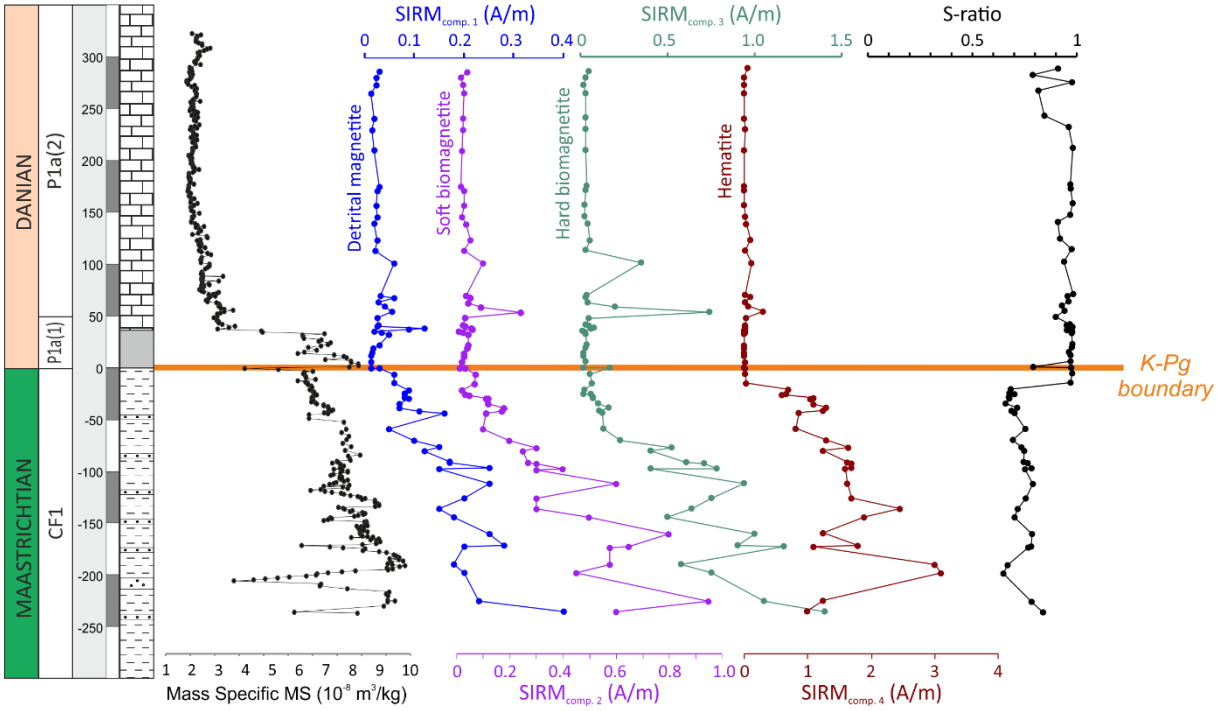

Figure 4.3 – Magnetic data of ZU collection: Mass specific magnetic susceptibility (MS), Saturation Isothermal Remanent Magnetization (SIRM) of component 1 (detrital magnetite), component 2 (soft biomagnetite), component 3 (hard biomagnetite) and component 4 (hematite), S-ratio which is indicative of magnetite - hematite relative proportion. SIRM and S-ratio curves were acquired by using the Kruiver et al. (2001) software. Absolute values are reported in Table 8.2.

4.2 The PETM transition at Dababiya

Mass specific magnetic susceptibility is nearly cyclical along the entire section, varying between 3.12 x 10^{-8} and 6.28 x 10^{-8} m^3/kg (Figure 4.5), suggesting that MS is mostly controlled by climate parameters such as eustatism and Milankovitch cycles. However, the interval near the PETM boundary is characterized by abrupt shifts of higher values of MS, varying between 5.26 x 10^{-8} and 1.5 x 10^{-7} m^3/kg (Figure 4.5). This abrupt and positive shift in MS, resulting from the absence of carbonates (diamagnetic compound) and, consequently, higher relative abundance of ferromagnetic particles. Such acyclical and sudden changes cannot be explained by eustatism or Milankovitch cycles, but are rather the signature of the abrupt climate change characterizing the PETM interval.

Frequency-dependent susceptibility (K_{fd}) of Dababiya section vary essentially between 2-8% (Figure 4.5), which is indicative of admixture of SP grains and coarser non-SP grains or eventually, SP grains under 0.005 µm. There are also a few samples with K_{fd} values < 2%, which indicates the absence of SP grains. Such values may suggest that Dababiya section was affected by bichemical processes. Negative and very high values (>14%) of K_{fd} are considered as measurement error and was dismissed from the analysis.

IRM measurements were carried out for all samples of Dababiya collection. The linear and gradient acquisition plots (LAP and GAP, respectively) of 6 representative samples are presented in Figure 4.4.

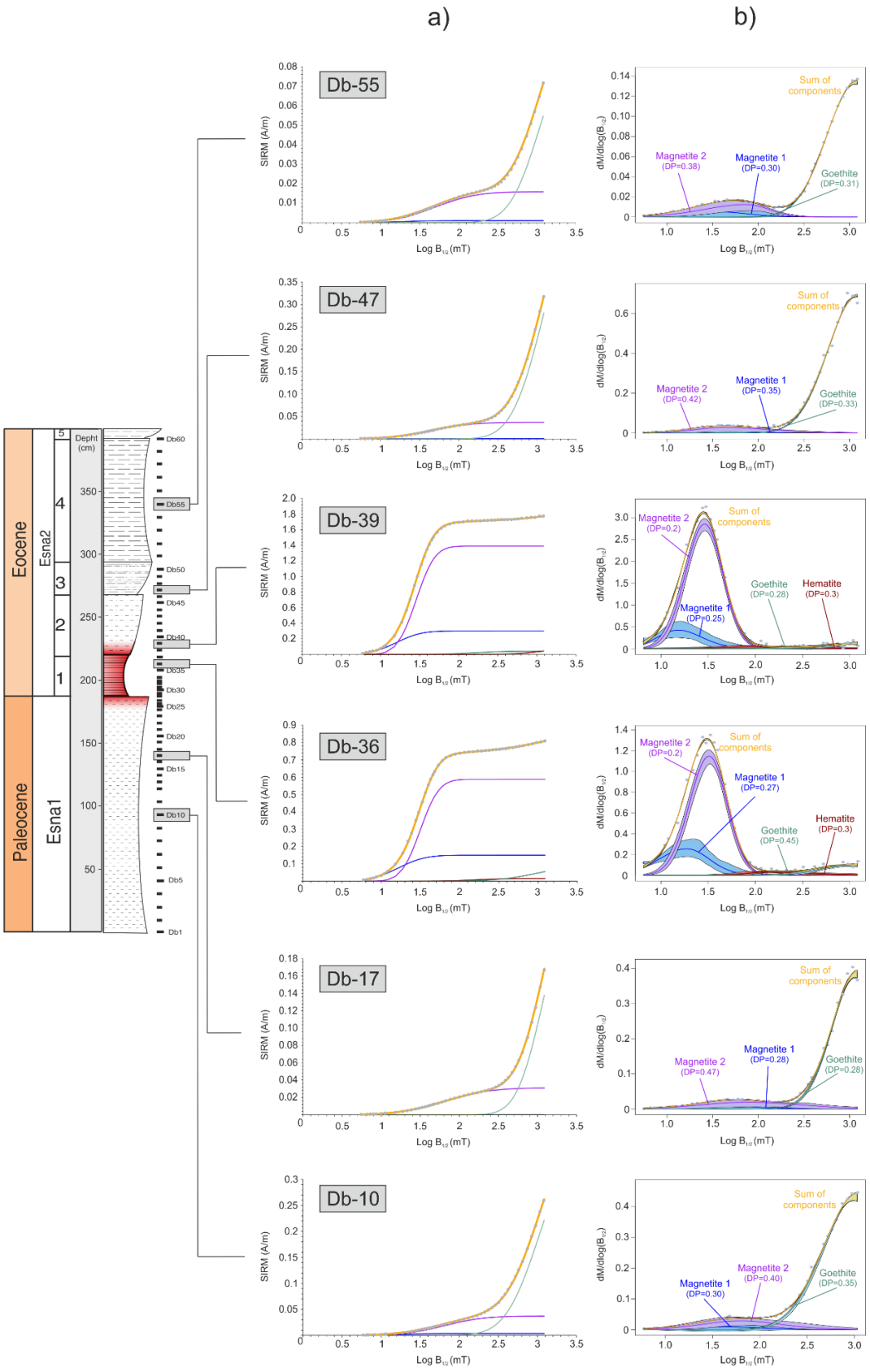

Figure 4.4 - a) Linear Acquisition plot of Isothermal Remanent Magnetization (IRM) curves from six representative samples of the Dababiya section, unmixed by using the Kruiver et al. (2001) software. b) Coercivity distribution (Gradient acquisition plot) derived from IRM curves obtained by using the MAX UnMix software (Maxbauer et al., 2016). The shaded area represents error envelopes of 95% confidence intervals.

After unmixing IRM curves, four components were identified: two populations of magnetite (components 1 and 2), hematite and goethite.

Linear acquisition plots of IRM curves (Figure 4.4a) clearly shows the predominance of goethite along the Dababiya section. The contribution of the other components is very small compared to the contribution of goethite. As goethite is strongly coercive (Figure 4.4b), a higher magnetic field is required to saturate goethite, much higher than the maximum field induced by the equipment (~1.2 T). Therefore, the IRM curve do not reach saturation at 1.2 T. A very distinct pattern of the linear and gradient acquisition plots is found for samples within the PETM interval (Db-36 and Db-39). In the PETM interval, the contribution of the magnetite is higher than the contribution of goethite. As magnetite is a lower coercive mineral (Figure 4.4b), the sample reaches the magnetization of saturation below 1.2 mT.

Unmixed Isothermal remanent magnetization curves indicate the presence of three ferromagnetic components in the whole Dababiya section, except in the PETM interval, where four components are identified (Figure 4.4 and 4.5). Component 1 has very low logarithmic values of mean coercivity (Log $B_{1/2}$), ranging 1.2 – 1.3 mT, and DP values between 0.25 and 0.37 mT, which are typical of detrital magnetite (Egli, 2004). Component 2 has Log $B_{1/2}$ values ranging from 1.65 to 1.9 mT along the entire section except in the PETM interval where Log $B_{1/2}$ values are significatly lower (between 1.4 – 1.55 mT). The DP of component 2 varies between 0.25 and 0.5 mT along the Dababiya section and it also decreases in the PETM for values ranging 0.18 – 0.26 mT. The values along the section are typical of detrital magnetite (Egli, 2004). However, DP values < 0.2 mT found in the PETM interval (Figure 4.4 and 4.5) may also be suggestive of the presence of magnetossome. Component 3 has Log $B_{1/2}$ values ranging 2 – 2.2 mT and DP values of 0.3 – 0.45 mT which are typical of hematite. Finally, component 4 is characterized by high Log $B_{1/2}$ values, which vary between 2.86 – 3.22 mT and, by DP values oscilatting between 0.26 – 0.47 mT, typical of goethite (Egli, 2004).

The concentrations of magnetite 1, magnetite 2, hematite and goethite are represented in Figure 4.4a and 4.5 as a function of their saturation remanent values (SIRM). The magnetite content is very low along the Dababiya section except in the PETM interval where abrupt positive shifts are observed for both components, magnetite 1 and magnetite 2. The concentration of hematite is below detection limit along the section, except in the PETM interval where the SIRM of hematite is characterized by two prominent positive shifts. The increase of magnetite and hematite content in the interval near the PETM boundary results from the absence of carbonates in Bed-1 and the very small carbonate content of Bed-2. Carbonates are diamagnetic compounds, so they do not contribute to the remanence. In addition, the mineralogy of beds -1 and -2 has a higher detrital affinity, namely clays, which generally host high contents of ferromagnetic iron oxides. The SIRM curve of goethite is more variable than the SIRM curves of the other components. However, a clear negative shift is identified in the interval above de Paleocene-Eocene boundary, indicating a lower content in goethite.

The S-ratio is indicative of the relative proportion between the low (magnetite) and high (hematite and goethite) coercive components. S-ratio values at Dababiya section are relatively constant, varying essentially between 0.1 and 0.3 (Figure 4.5), which reflects the dominant contribution of the higher coercive components, principally goethite. As expected, this pattern is reversed in the interval above the Paleocene-Eocene boundary where S-ratio acquires values between 0.58 – 0.98, indicating a higher contribution of magnetite for the total remanence.

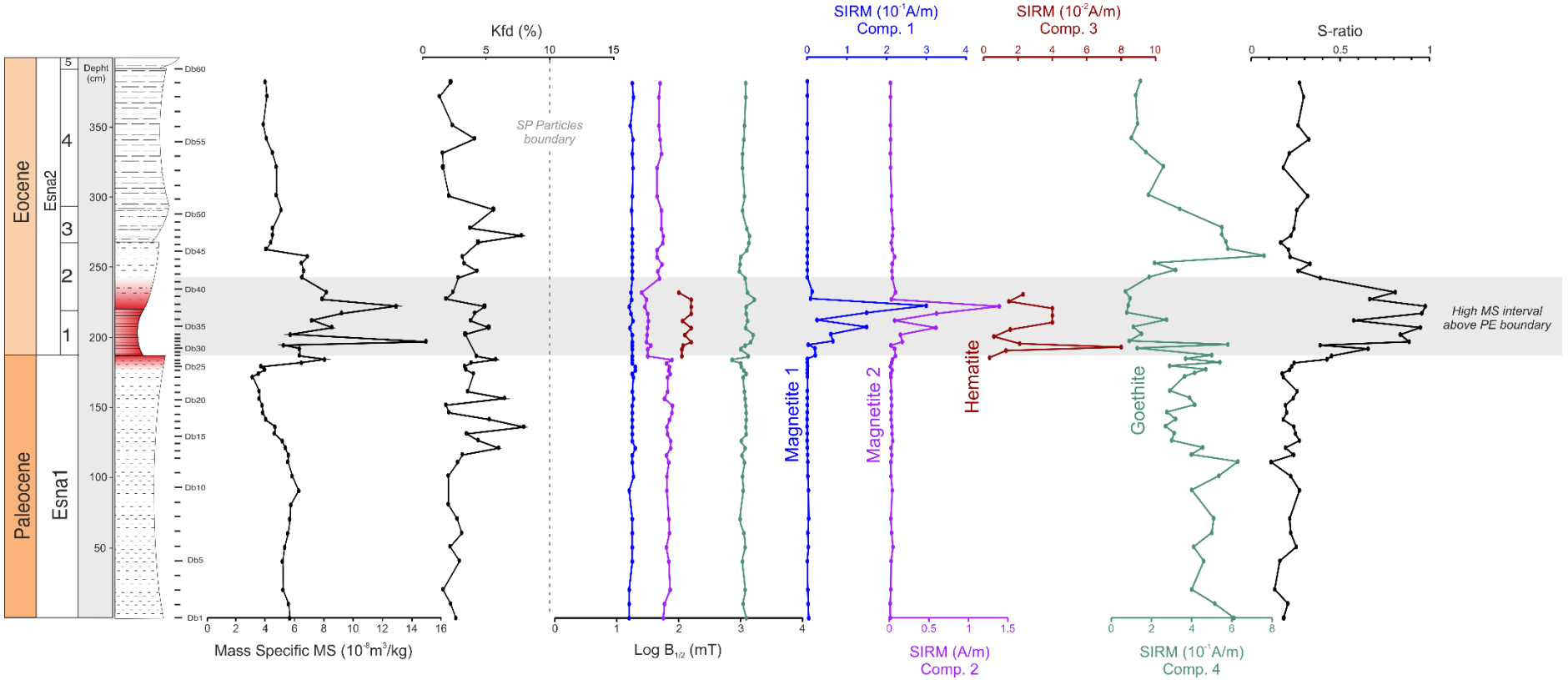

Figure 4.5 - Magnetic data for the Paleocene-Eocene transition at Dababiya: Mass Specific Magnetic Susceptibility (MS), Frequency Dependent Susceptibility (Kfd), Coercivity (logB1/2), Saturation Isothermal Remanent Magnetization (SIRM) and Dispersion Parameter (DP) for component 1 (detrital magnetite), component 2 (magnetite), component 3 (hematite) and component 4 (goethite) and S-ratio which is indicative of magnetite - hematite relative proportion. SIRM, log (B1/2) and S-ratio curves were acquired by using the Kruiver et al. (2001) software. The red interval corresponds to the dissolution interval defined by Saleh (2013). Absolute values are reported in table 8.3.

In order to evaluate the presence of magnetosomes in the PETM interval, First-Order Reversal Curves (FORC) measurements were performed for two samples within the interval (Db-36 and Db-39). Indeed, magnetofossils are generally characterized by very low DP values and a central narrow ridge typical of non-interacting SD magnetite in FORC diagram (Abrajevitch et al., 2015). FORC results (Figure 4.6) do not show any evidence of the typical narrow central ridge, suggesting the absence of biomagnetite. The pattern obtained for both samples is similar and corresponds to the signature of SD particles. Since there is no biomagnetite in the interval, the lower DP values previously described may reveal the presence of a very fine grain magnetite.

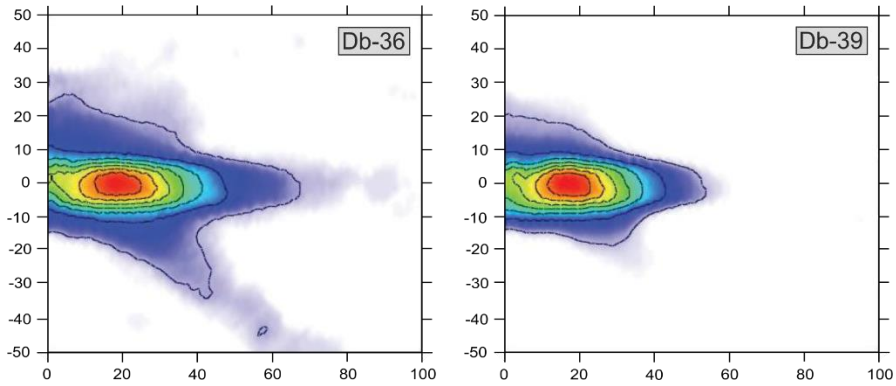

Figure 4.6 – First Order Reversal Curves (FORC) diagram for samples Db-36 and Db-39, revealing a single-domain signature

5. Discussion

A continuous sedimentary record is one of the most important criterion to reconstruct past climate and environmental changes. Both sections, Zumaia and Dababiya, have been considered expanded and complete, and therefore representative of KPg and PETM events (Dinares-Turrel et al., 2003; Batemburg et al., 2014; Despuis et al., 2003; Aubry et al., 2007). However, Font et al. (2018) shown that part of the early Danian, namely P0 and the lower part of P1(a1) biostratigraphic zones, is missing at Zumaia. At Dababiya, Schulte et al. (2011) observed that the GSSP occurred in a submarine channel, which was confirmed by Saleh (2013) who also identified significant lateral variations in lithology, suggesting erosion and/or non-deposition. The non-continuity of both sections may introduce some doubts about the viability of Zumaia and Dababiya as representative of the KPg and PETM events. However, both sections have excellent outcrops where the lithostratigraphic units can be easily identified, characteristic mineralogical and geochemical contents, well preserved fossil records and other global and important proxies. All these characteristics make both, Zumaia and Dababiya, good sections to reconstruct the past climate and environmental changes. However, the presence of hiatus in the sections should be considered with caution in the interpretations.

5.1 The KPg transition at Zumaia

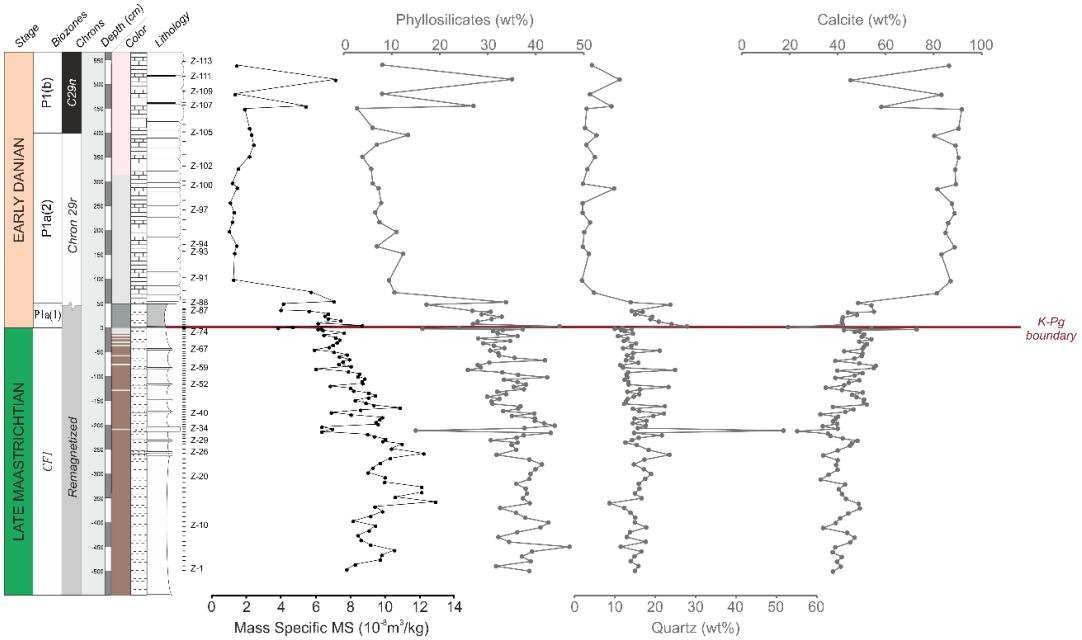

Figure 5.1 – Mass Specific Magnetic Susceptibility (MS) and Mineralogical Data of Zumaia samples (Z collection). The concentration of Phyllosilicates, Quartz and Calcite is expressed as a percentage of the total mass of each sample (wt%). Mineralogical data provided by Thierry Adatte. Absolute values are in table 8.4.

A strong correlation of phyllosilicates and calcite with MS, suggest that MS is dominantly controlled by the lithology, and thus may have a climate and environmental significance (Figure 5.1 and 5.2). Fundamentally, MS is controlled by the balance between detrital input and carbonate productivity, which depends on the distance of the source, itself controlled by sea level changes. The several picks along the Maastrichtian marls correspond to the turbidites deposits and therefore are not significant to explain the paleoenvironmental changes.

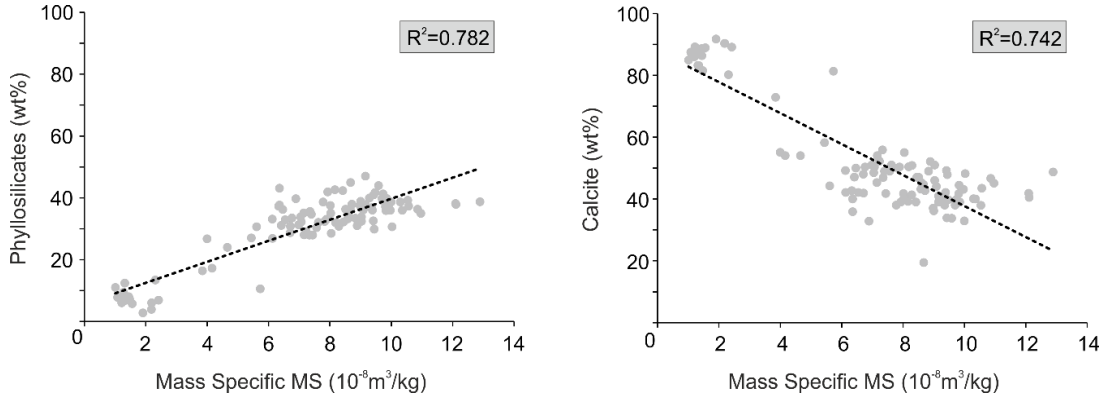

Figure 5.2 – Correlation between mass specific magnetic susceptibility and phyllosilicates (left) and calcite (right). The samples corresponding to turbiditic deposits were not considered in the correlations. R^2 is the determination coefficient, $R^2 = 1$ - (SSresidual / SStotal) where SStotal is the total sum of squares and SSresidual is the sum of the squares of residuals. Mineralogical data provided by Thierry Adatte.

A high magnetic susceptibility level was found at the clay interval just above the KPg boundary in other KPg sections, namely at Gubbio (Italy) and Bidart (France) (Font et al., 2011, 2014; Abrajevitch et al., 2015) (Figure 5.3). Since there is a hiatus on the basal part of the Danian limestones, indicated by the absence of characteristic planctik foraminifera (Font et al., 2018), this level is not observed at Zumaia. Actually, the level that marks the Maastrichtian-Danian boundary at Zumaia is characterized by very low MS values (Figure 5.1) caused by a high content of secondary calcite observable in the field. Font et al. (2018) interpreted this low MS level as a decollement level, filled by secondary calcite, providing an explanation for the presence of a hiatus at the base of Danian.

A low MS interval characterized by loss in detrital and biogenic magnetite has also been clearly identified below the KPg transition at Gubbio and Bidart (Lowrie et al., 1990; Font et al., 2011, 2014; Abrajevitch et al., 2015) (Figure 5.3). The first explanation for such a low magnetite interval was given by Lowrie et al. (1990) who interpreted this low content observed at Gubbio as a result from the reduction of iron oxide and subsequent removal of the Fe^{2+} ions. According to the author, the reduction may be a consequence of downwards infiltration of reducing waters resulting from the large quantity of organic matter produced by the extinctions at the KPg boundary.

However, there is no evidence of reducing conditions at Bidart and Gubbio, leading Font et al. (2014) to suggest that the loss in magnetite rather result from particular environmental changes that prevailed at that time, where acidic weathering provides a plausible mechanism for iron oxide dissolution. Increased acidity of meteoric water is a common consequence of large aerosol release during volcanic eruptions (Abrajevitch et al., 2015). Under normal pH conditions (pH~5.6 for present-day rainwaters), detrital magnetite can persist on the continental surface for several million years, but it is rapidly dissolved with decreasing pH (Font et al., 2014). Using a geochemical weathering model (PREEQC) on a regolith, Font et al. (2014) showed that the time required to dissolve 90% of the initial magnetite mass, during transportation from the sediment source area to the deposition site, is between 31,000 (pH 3.3) and 68,000 yr (pH 4.3). Based on paleomagnetic data (Chenet et al., 2008; 2009), these values are compatible with the temporal duration of the Deccan volcanic emissions.

Although detrital magnetite loss may be explained by acid dissolution as consequence of the intense volcanism, the decrease in biogenic magnetite cannot. Magnetotatic bacteria live in marine sediments and the pH of the ocean is rapidly buffered by carbonate cycle. A decrease in reactive iron (Fe^{2+}) could limit the growth of magnetotatic bacteria (Roberts et al., 2011). On the other hand, magnetotatic bacteria

live at the oxic-anoxic interface, being very sensitive to variations in the ocean chemistry. Therefore, the loss of biogenic magnetite could be explained by a Fe^{2+} ocean input decrease or by changes in seawater/sediment chemistry. Since rivers are the main ocean suppliers of chemical species, they should transport less Fe^{2+} to the ocean. However, because acid rains are promoting the dissolution of magnetite on land, Fe^{2+} and Fe^{3+} ions are being produced and transported to the ocean. This suggests that development of magnetotatic bacteria, and consequently the production of magnetossomes, is not related to the supply of Fe^{2+} but rather to seawater/sediment chemistry (acidification). Actually, intense acid rains may promote variations in the chemocline, changing the oxic-anoxic interface, disturbing the magnetotatic bacteria development.

Unmixed IRM curves obtained for the Zumaia section revealed the presence of four main magnetic compounds: detrital magnetite, soft magnetite, hard magnetite and hematite. Having primary hematite (which is usually dark) in marine sediments is not very common. The red color of the rocks at Zumaia (Figure 2.1) suggest the presence of hematite pigments, which have a secondary origin. Therefore, the hematite origin is probably secondary, resulting from the oxidation of the primary magnetite during diagenesis. Consequently, it has no significance to the paleoclimatic interpretations, in contrary to detrital and biogenic (soft and hard) magnetite.

At Zumaia, the low MS interval recorded at Gubbio and Bidart is not clearly observed (Figure 5.3), although a slight but significant gradual decrease in MS values was found 2 m below the KPg boundary (Figure 5.3). This slight MS decrease during the uppermost Maastrichtian and early Danian can be comparable with the low MS interval at Gubbio and Bidart (Figure 5.3). Although a slight increase in calcite content (from ~40 to ~50wt%) is observed (Figure 5.1), this mineralogical variation is too small to explain the observed MS decrease, suggesting that the sea level is not the only factor controlling the magnetic susceptibility variations.

The concentration of detrital magnetite is proportional in abundance to the detrital fraction (phyllosilicates) and therefore, Maastrichtian marls have higher contents of detrital magnetite and hematite than Danian carbonates (Figure 4.3). However, magnetite content (SIRM of comp. 1, 2 and 3) is abnormally low in the last 50 cm below the KPg boundary as well as in the first centimeters above this limit, being comparable to the typical low values of the Danian limestones which do not have terrigenous affinity (Figure 4.3). Once again, the variations in mineralogy are not significant, being too small to explain such a low content in magnetite (Figure 5.1). Therefore, I suggest that dissolution of ferromagnetic iron oxides, rather than sea level, may control the decrease in magnetic susceptibility and magnetite content, similarly to what has been observed in Bidart and Gubbio.

These data provide further evidence of the influence of Deccan-induced climate perturbation at the dawn of the KPg mass extinction. Furthermore, Abrajevitch et al. (2015) found biogenic magnetite, which is particularly sensitive to reductive dissolution, between the KPg clay layer (with the iridium anomaly) and the low susceptible zone, at Gubbio and Bidart (Figure 5.4). This, together with the fact that the magnetite depleted interval at Zumaia encompasses the KPg boundary (Figure 4.3 and 5.3), is inconsistent with the downward percolation of reducing fluids suggested by Lowrie et al. (1990). Therefore, the low susceptible zone more likely marks a different environmental event that preceded the impact.

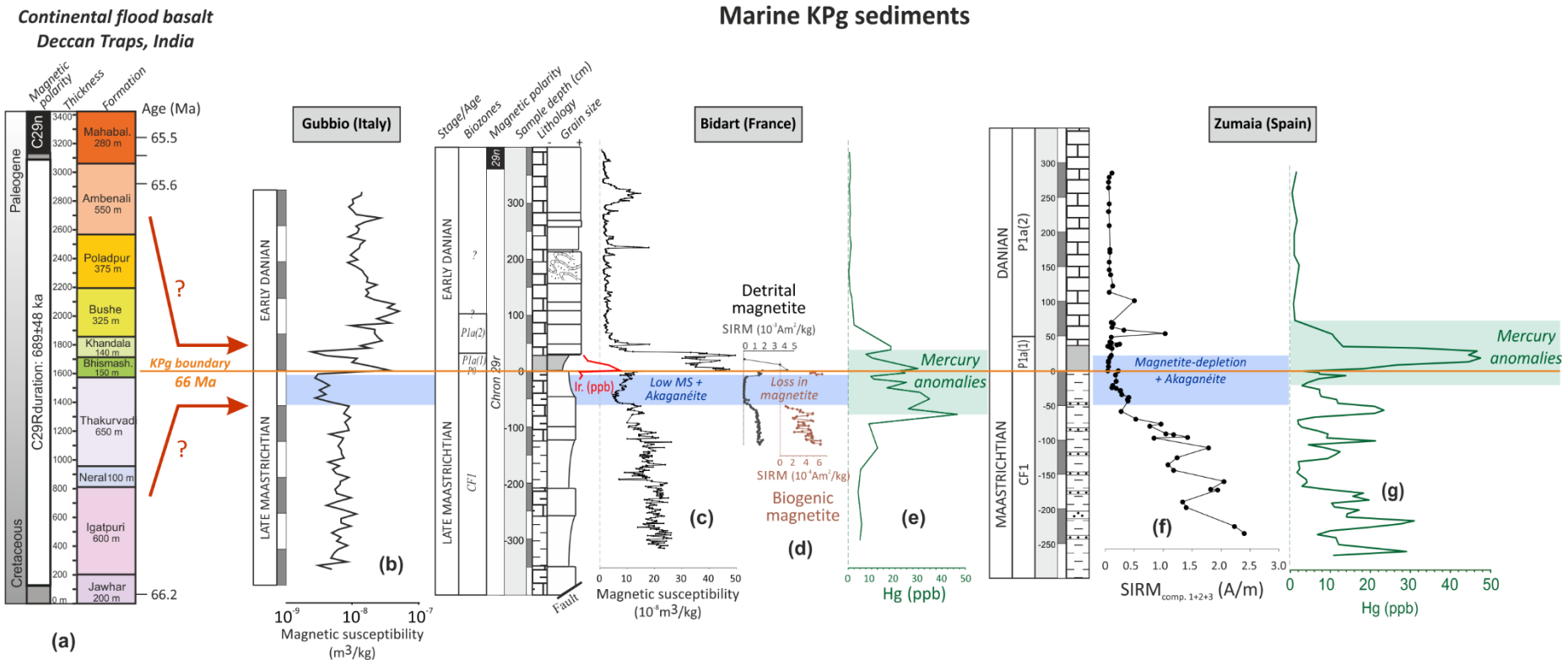

Figure 5.3 – Correlation of a) the age of the Deccan lava flows in India (Schoene et al., 2014) with the KPg marine sections marked by b) the low MS interval at Gubbio (Italy); c) the low MS interval containing akaganéite at Bidart (France); d) the depletion in detrital and biogenic magnetite at Bidart; e) mercury anomalies at Bidart; f) the magnetite-depleted interval containing akaganéite at Zumaia (Spain); and, g) mercury anomalies at Zumaia. Modified from Font et al. (2018).

The link with the Deccan volcanism is also comforted by the presence of a rare chlorine-bearing iron oxyhydroxide, akagenéite, which was observed in the magnetite depleted interval at Gubbio and Bidart (Font et al., 2011; 2014) and later at Zumaia (Font et al., 2018). Akaganéite is very rare on Earth, because its precipitation requires highly oxidizing, acidic and hyper-chlorinated environments, similar to those present on Mars or in acid-sulphidic and volcanic settings on Earth (Font et al., 2018). The akaganéite founded at Zumaia is present not only below the KPg boundary as well just above this limit (Figure 5.3). However, the presence of akaganéite above the KPg boundary may be suspicious due to the presence of sulfur in its composition. To address this problem, more Micro-Raman spectrometry analysis should be conducted in the future.

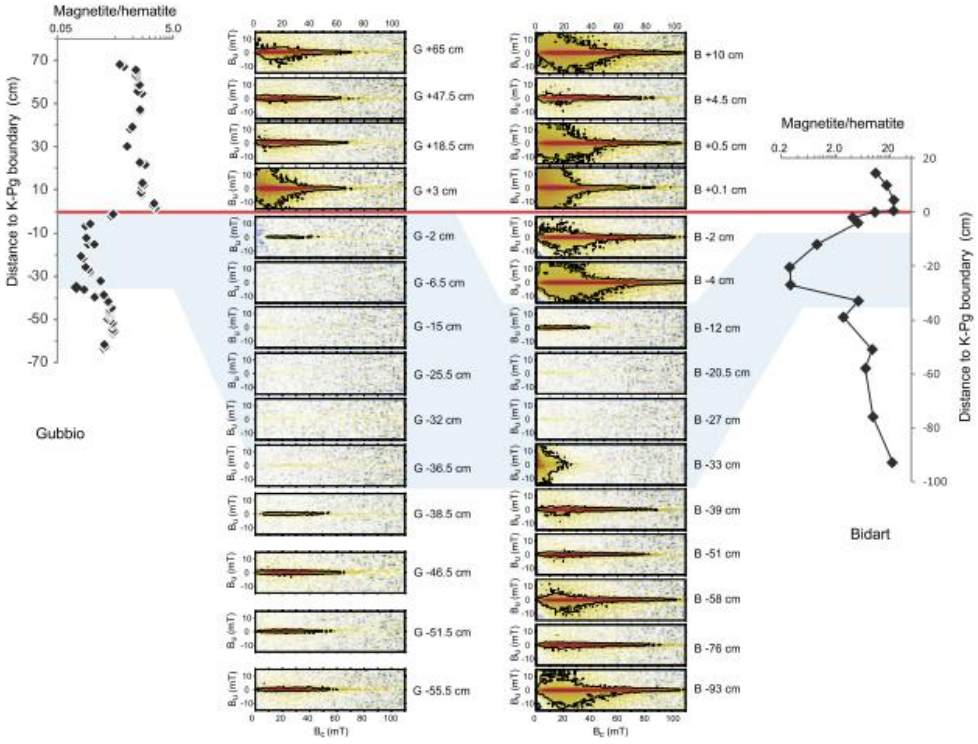

Figure 5.4 – FORC characteristics of the KPg transition intervals at Gubbio and Bidart. The central ridge is indicative of the presence of magnetite magnetofossils. The central ridge is absent in samples from the low susceptible zone in both sections except in the 2cm below the KPg boundary at Gubbio and in samples from -2 to -12 cm interval at Bidart. Figure from Abrajevitch et al. (2015).

The occurrence of akaganéite in the marine sediments of all three sections is exceptional, providing support for a volcanism related origin of the low susceptible zone. A plate-like shape well-embedded in concordance with the deposition plane of the sediment, as well as the fact that akaganéite does not fill fractures, suggest a primary depositional origin. The relatively well-preserved shape of the akageneite grains compared to the severely altered aspect of the detrital iron oxides contained in the same sample argue for aeolian transportation (Font et al., 2017). These observations suggest that akaganéite was formed in the Deccan volcanic plume and was further transported to the Atlantic and Tethys realms through the stratosphere (Font et al., 2017).

Also supporting the volcanic origin of the low susceptible zone is the presence of a mercury-rich level observed at Bidart and Zumaia (Font et al., 2016; 2018) (Figure 5.3). Mercury (Hg) have been identified as an excellent indicator of massive volcanism in the marine sedimentary record (Font et al., 2016). Mercury could enter marine sediments bound to clays, but its presence is usually related with the input

of terrestrial organic matter. Font et al. (2016; 2018) showed that there was no correlation between Hg and total organic carbon or phyllosilicates, suggesting that Hg was deposited from the atmosphere, and therefore that it has a volcanic provenience.

During Mesozoic, Zumaia and Bidart were part of the Basque-Cantabric basin, located in the Atlantic Ocean, while Gubbio was located in the Tethys realm. The presence of Deccan volcanic markers like magnetite depletion, akaganéite and Hg-rich levels in these sections thus suggest a rather global phenomenon. On a global scale, the low magnetite interval observed at Zumaia, Gubbio and Bidart, correlates with an abrupt increase of temperature (2-4ºC), beginning at 500 kyr and ending at ~20-50 kyr before the KPg boundary, recorded in fossil plants and foraminifera present in terrestrial and marine sections from North Dakota, respectively (Wilf et al., 2003). Stable carbon and oxygen isotopes from paleosol carbonates in Texas also point to an increase in temperature, accompanied by an elevated atmospheric CO_2 pressure, with CO_2 levels ranging between 1000 and 1400 ppmV, in the 500 kyr prior to the KPg boundary (Nordt et al., 2003). In the South Atlantic, a short-term warming of 2-3ºC was also reported by carbon and oxygen isotopes below the KPg boundary (Li and Keller, 1998). This positive shift in temperature recorded worldwide is coincident with the Deccan main phase-2 (Figure 5.5). Therefore, the temperature anomaly is likely consequence of the huge amount of CO_2 and other greenhouse gases released during the second and most intense phase of Deccan eruptions.

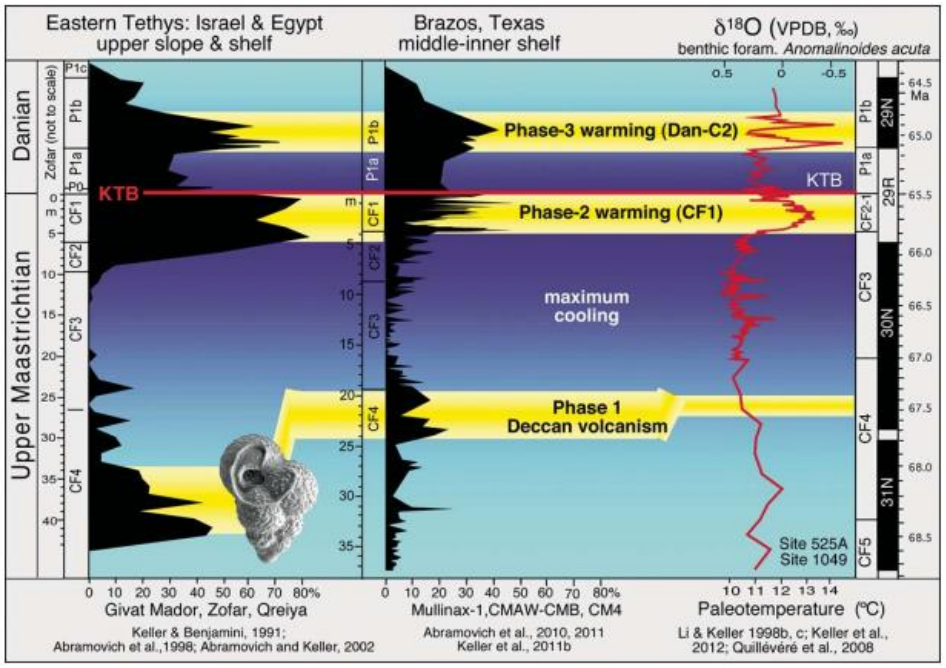

Figure 5.5 – Guembelitria cretacea blooms recorded from the eastern Tethys and Texas correlative with the three phases of Deccan volcanism. Phases 2 and 3 are associated with times of rapid warming in biozones CF1 and P1b. Phase-2 of the Deccan eruptions and the warming in CF1 biozone correlates with the magnetite decrease interval observed at Zumaia in this study.

Moreover, the low contents of detrital and biogenic magnetite, correlates not only with the global warming as well as with higher abundance of *Guembelitrian cretacea*, a disaster opportunist species that was recorded in the eastern Tethys and Texas (Keller, 2014) (Figure 5.5). Blooms of this foraminifera consist of generally dwarfed specimens that dominate low diversity high-stress marine assemblages worldwide and are frequently accompanied by rapid climate changes and ocean acidification (Font et al., 2018).

A decline in seawater $^{187}Os/^{188}Os$ ratio was also recorded throughout the global ocean just below the KPg boundary (Robinson et al., 2009) (Figure 5.6). The authors indicated the second (main) phase of Decan volcanism as the cause of such isotopic decline but the process by which volcanism could generate such isotopic anomaly was not described. The large difference in osmium isotope ratio between continental crust (~1.4) and mantle (~0.127) reservoirs could generate large seawater Os isotope variations (Dickin, 2005; Percival et al., 2016). Actually, large igneous provinces have been associated to negative excursions in the marine Os isotope (Cohen & Coe, 2002; Turgeon & Creaser, 2008; Percival et al., 2016). However, the specific pathway(s) for transfer unradiogenic osmium from LIP magmatism to the oceans is poorly constrained.

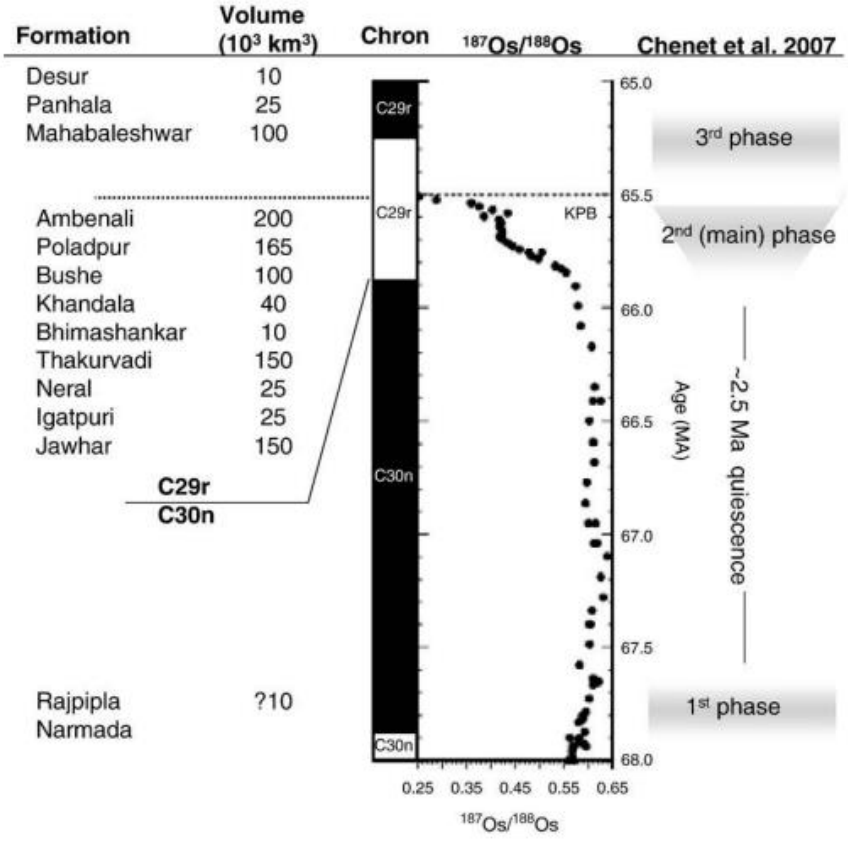

Figure 5.6 – Comparison of proposed stratigraphic sequence of Deccan Basalts with proposed stages of volcanism from Chenet et al. (2007) and $^{187}Os/^{188}Os$ data from Bottaccione (Gubbio, Italy). The same $^{187}Os/^{188}Os$ pattern was recorded at 3 more different locations: DSDP Site 577 (Shatsky Rise, Western Pacific), ODP Site 690 (Maud Rise, Weddell Sea) and DSDP Site 525 (Walvis Ridge, Atlantic), see Robinson et al. (2009). Figure from Robinson et al. (2009).

The isotopic composition of dissolved osmium in the oceans reflects mass balance between osmium input from hydrothermal alteration of juvenile oceanic crust, average riverine input from continental weathering, together with a generally minor extraterrestrial contribution from meteorites and cosmic dust particles (Turgeon & Creaser, 2008). Therefore, processes such as, continental weathering of basalt lava flows, low-temperature hydrothermal alteration of ultramafic rocks or meteoritic impacts/dissolution of cosmic dust have been indicated as possible causes for $^{187}Os/^{188}Os$ ratio depletions (Sharma et al., 2000; Cohen & Coe, 2002; Turgeon & Creaser, 2008; Percival et al., 2016).

The $^{187}Os/^{188}Os$ anomaly below the KPg boundary coincides in time with the second phase of Deccan volcanism, when huge amounts of lava were extruded (Figure 5.6), and with the global warming and

consequent weathering intensification. Therefore, the most likely explanation for the Os isotopic excursion is the intensive weathering of Deccan basalts, which were located at subtropical latitudes at that time. The dissolved radiogenic osmium would then enter the ocean by riverine input causing the global ocean anomaly after ocean homogenization.

Robinson et al. (2009) also recorded a decrease in bulk carbonate content that coincide with the Os isotope negative shift, suggesting that carbonate burial flux may have been lower during the $^{187}Os/^{188}Os$ ratio decline. The authors speculated that diminished carbonate burial rate may have been the result of ocean acidification caused by Deccan volcanism. Such theory is consistent with the hypothesis presented here to explain the loss in magnetite in the interval below the KPg boundary.

The new data presented here supports an important climate event preceding the KPg boundary and comfort previous results obtained in Bidart and Gubbio (Font et al., 2014, 2016). Volcanic markers like magnetite dissolution previously identified in Bidart and Gubbio are confirmed here in the case of the Zumaia section. Magnetite depletion also corroborates the presence of akaganéite and Mercury at Zumaia to support the volcanic theory. On a global scale, these markers correlate with global warming, an increase in atmospheric CO_2, environmental acidification via acid rains and presence of high stress environments with opportunistic species blooms. This climate perturbation also corresponds to the age of the main Deccan eruptions recently dated by U-Pb method on zircon (Schoene et al., 2014) reinforcing the link with the Deccan traps. These findings provide new clues to elucidate the origin of the KPg mass extinction.

5.2 The PETM transition at Dababiya

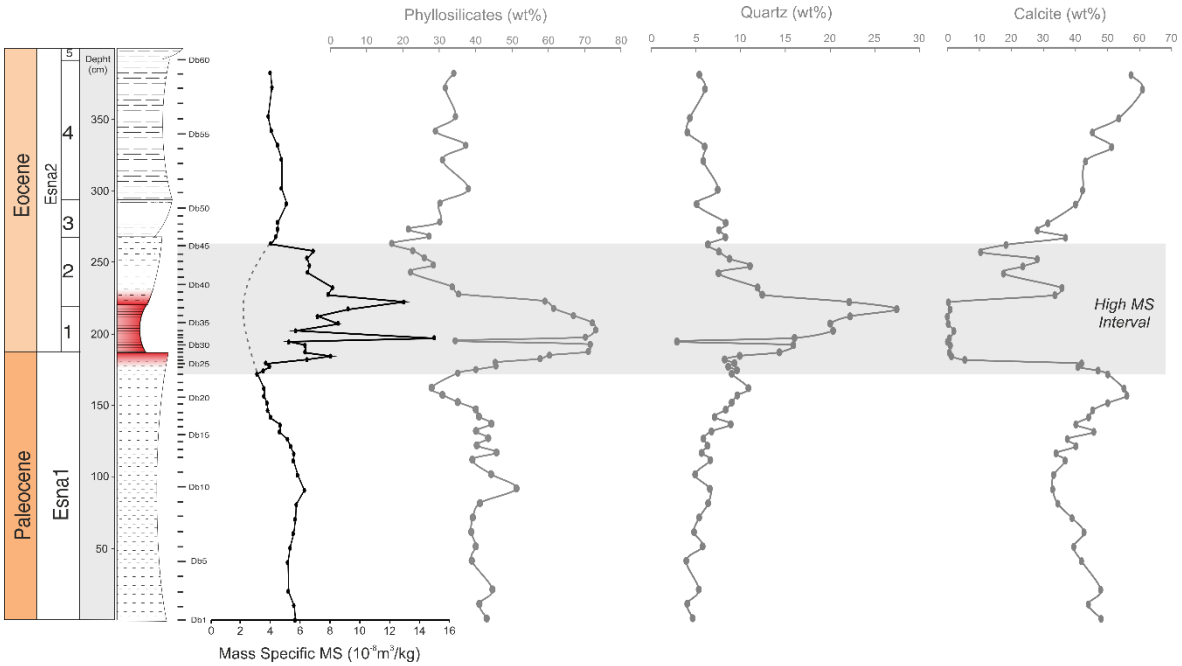

Figure 5.7 – Mass Specific Magnetic Susceptibility (MS) and Mineralogical Data of Dababiya samples. The concentration of Phyllosilicates, Quartz and Calcite is expressed as a percentage of the total mass of each sample. Absolute values are in table 8.5.

The PETM interval defined by changes in MS is different in extend from the one defined by SIRM (Figure 5.8), showing clearly that such magnetic parameters are controlled by different sources. In fact, SIRM only depends on the presence of ferromagnetic particles in a sample. On the other hand, as

referred is chapter 3, magnetic susceptibility depends not only on the concentration of ferromagnetic particles but on all magnetizable material present in a sample which include ferromagnetic, diamagnetic and paramagnetic compounds (see topic 3.1).

A strong relation between MS and mineralogy is clearly observed at Dababiya (Figure 5.7). The concentration of the main mineralogical compounds, as well as the MS concentration, is nearly cyclical along the section, suggesting that MS is mostly controlled by the balance between carbonate productivity and detrital input, in turn controlled by climate parameters such as the eustatism and the Milankovitch cycles. However, the interval near the PETM boundary is characterized by an acyclical, abrupt and positive shift in MS, resulting from the absence of carbonates (diamagnetic compounds) and higher relative abundance of ferromagnetic particles. Such sudden changes cannot be explained by eustatism or Milankovitch cycles, suggesting that leaching of carbonate contents under acid conditions and/or dilution by increased detrital input may have disturbed the balance between carbonate productivity and detrital input.

A magnetic approach has never been applied at Dababiya but several mineralogical and geochemical studies have been carried out (Schulte et al., 2011, 2013; Khozyem et al. 2014, 2015; Keller et al., 2017). Schulte et al. (2011) interpreted this absence of calcite and concomitant phyllosilicate increase at Dababiya as a result of severe carbonate dissolution, in addition to enhanced fluvial input due to erosion of coastal low lands, and deposition during a period of low or slightly rising sea level. Based on the paleotopography of the depositional basins, Khozyem et al. (2015) interpreted the PETM low calcite/high detrital interval as a result of increased fluvial discharge into the Dababiya submarine channel during a transgressive system tract period. This detrital input reported at Dababiya, characterizes not only this section but several PETM sections worldwide (Bolle et al., 2000). Such global increase of detrital content is attributed to the intense on-land weathering during a hot humid climate, which is supported by a concomitant increase of the kaolinite in oceanic sediments (Bolle et al., 2000).

Unmixed IRM curves indicated the presence of detrital magnetite and goethite in the whole Dababiya section (Figure 4.4 and 5.8). The concentration of detrital magnetite is very low in the whole Dababiya section except in the PETM interval where it increases considerably. As expected, this abrupt increase is consistent with the increase of the detrital components, phyllosilicates and quartz (Figures 5.7 and 5.8). Goethite was interpreted as post-depositional and originating from the oxidation of pyrite. This mineral is much less abundant in the PETM interval, which could suggest that more oxic conditions inhibited the formation of pyrite at that time. However, Khozyem et al. (2015) reported the presence of disseminated idiomorphic pyrite crystals and pyrite framboids in the PETM interval, showing that anoxic conditions prevailed. Higher values of V/Cr comfort the existence of anoxic conditions (Figure 5.8). A more likely explanation to the low content in goethite is a better preservation of pyrite (and relative lower production of goethite, due to a lower porosity of the corresponding sediments). Therefore, goethite may be interpreted as an indicator of anoxia and pyrite preservation at the PETM interval.

Hematite is also present at Dababiya section, but its occurrence is restricted to the PETM interval (Figure 4.4 and 5.8). The presence of goethite (high coercive mineral) may mask the signal of less coercive minerals, which means that hematite may be present along the whole section but with a very weak concentration that are not detectable due to high concentrations of goethite. As well, the signal of magnetite is very weak along the entire section except in the PETM interval, where the concentration of goethite decreases.

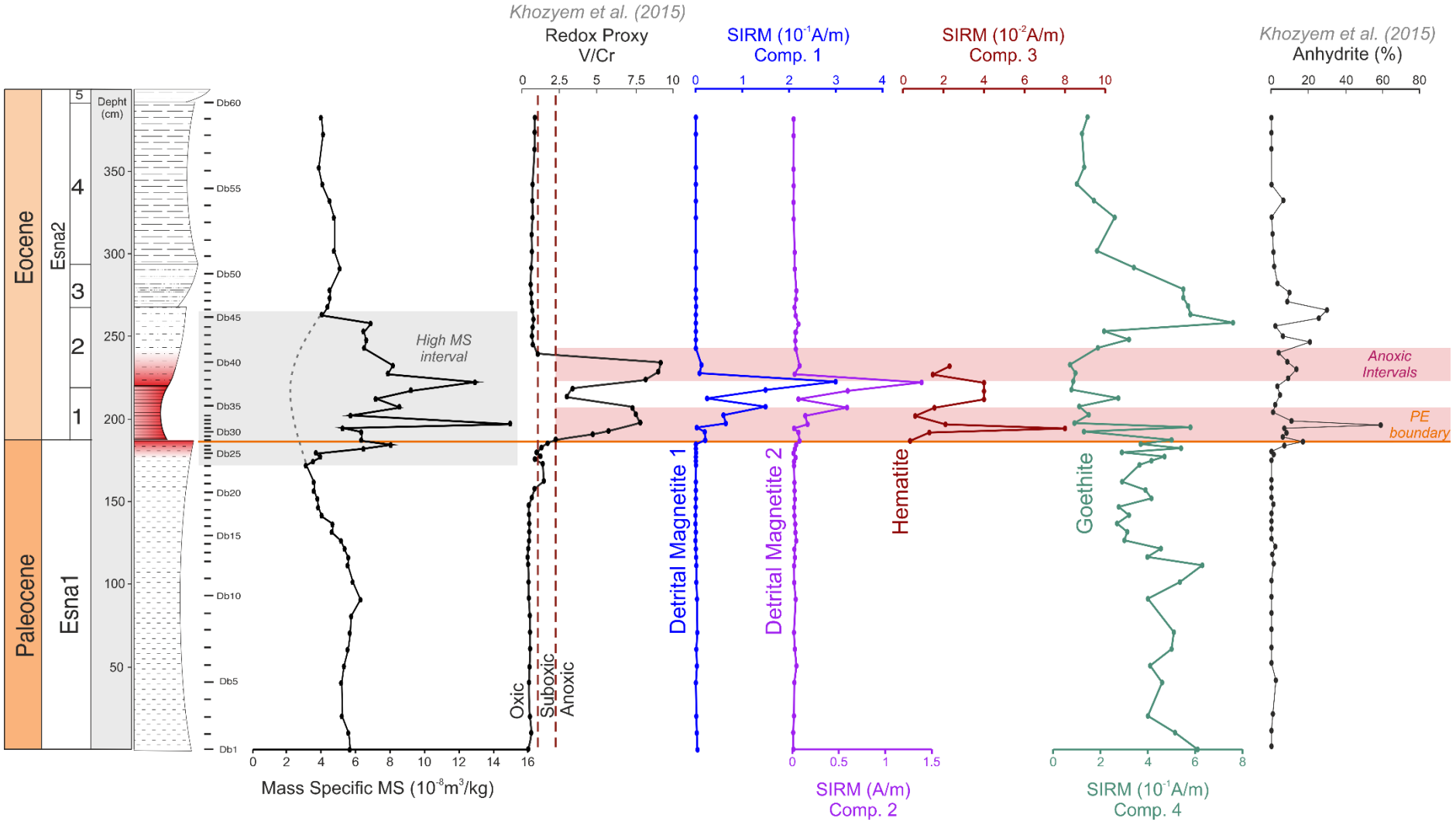

Figure 5.8 – Correlation between magnetic data from Dababiya section (Mass Specific Magnetic Susceptibility; concentration of detrital magnetite, hematite and goethite, expressed as a function of SIRM) and redox environmental conditions and anhydrite contents reported by Khozyem et al. (2015).

Nevertheless, the SIRM signal obtained for hematite has two distinct positive peaks. The second one correlates with the peak of magnetite and with a return to more oxic conditions, as noted by lower ratios of V/Cr (Figure 5.8). This, suggests that hematite may be secondary, resulting from the oxidation of magnetite. However, the first and most prominent peak cannot be explained by the alteration of magnetite because very anoxic conditions prevailed at that time and because magnetite content at that level is too low to explain the hematite peak.

The magnetic data are insufficient to determinate the origin of such hematite but several hypotheses can be discussed: (1) the first peak of hematite correlates with an abrupt decrease of detrital components (phyllosilicates and quartz) (Figure 5.7 and 5.8) and therefore a detrital origin is excluded; (2) hematite can result from the oxidation of pyrite but the anoxic conditions (Figure 5.8) and the fact that pyrite is very well preserved in the PETM interval lay down this hypothesis; (3) Hematite peak coincides with a prominent peak of anhydrite (Figure 5.8), which is usually originated in shallow waters due to intense evaporation. These environmental conditions are compatible with the formation of hematite but, once again, oxic conditions would be required. At Dababiya, the formation of anhydrite under anoxic conditions seems to be related with ocean acidification due methane release (Khozyem et al., 2015), (4) finally, the last and more likely explanation is the development of a Fe-rich level by leaching due to the circulation of meteoric and diagenetic waters. Such enrichments typically occur at lithologic discontinuities due to porosity contrasts. Indeed, the hematite peak is located at the bottom of bed-1, right above the PE boundary which marks a change in lithology from marine hemipelagic to coarser sediments linked to increased fluvial discharge from shallower environments (Schulte et al., 2011). The formation of hematite is therefore post depositional and linked to the accumulation of Fe species, during a return to more oxic conditions.

Resuming, the magnetic properties of the Dababiya section represent reliable indicator of climate changes, marking carbonate dissolution (i.e. high MS and SIRM values), detrital input (i.e. magnetite content) and anoxia (i.e. goethite content).

Concerning the nature and origin of the PETM climate perturbations, an extreme ocean warming starting in the final stage of Paleocene was reported worldwide by several authors. Based on TEX_{86} and oxygen isotope records from planktonic foraminifera, Zachos et al. (2006) estimated a sea surface temperature increase of 8ºC on the eastern margin of North America. Thomas et al. (2002) reported a period of gradual surface-water warming, infered on high-resolution analysis of single planktonic and benthic foraminiferal shells from the Weddel Sea (Southern Ocean). Tripati & Elderfield (2004) indicated a 3.5º-4ºC increase of sea surface temperatures infered by high-resolution temperature records of Mg/Ca ratios of planktonic foraminifera across the PE boundary in the equatorial Pacific and subtropical Atlantic. The period of ocean warming in the late Paleocene is also characterized by a significant global sea level rise (~20 m), which may have resulted from the melting of high-altitude or polar ice caps (specially small alpine ice sheets on Antarctida), thermal expansion of the oceanic water column (which could explained a maximum rise of 8 m), or both (Speijer and Wagner, 2002; Sluijs et al., 2008).

The North Atlantic Igneous Province (NAIP) volcanism has been indicated as the main cause for the ocean warming starting at the Paleocene. Ash deposits and a large drop in sediment $^{187}Os/^{188}Os$ ratio were reported at Svalbard Archipelago (Norway) in the onset of the PETM event (Wieczorek et al., 2013). Contrary to the Os anomaly reported near the KPg boundary (see topic 5.1), the low $^{187}Os/^{188}Os$ ratio of the PETM is not global in extend, being restricted to the North Atlantic area. It should be taken into account that isotopic Os measurements near the KPg transition were carried out for sea water and the isotopic Os ratios infered by Wieczorek et al. (2013) were reported in sediments thus, a local

anomaly could only be expected. Wieczorek et al. (2013) suggest that the negative Os excursion that started in the late Paleocene resulted from both, direct input of ash (carring low $^{187}Os/^{188}Os$ ratios) to the basin and rapid terrestrial weathering of the ash deposited on land during the NAIP volcanism.

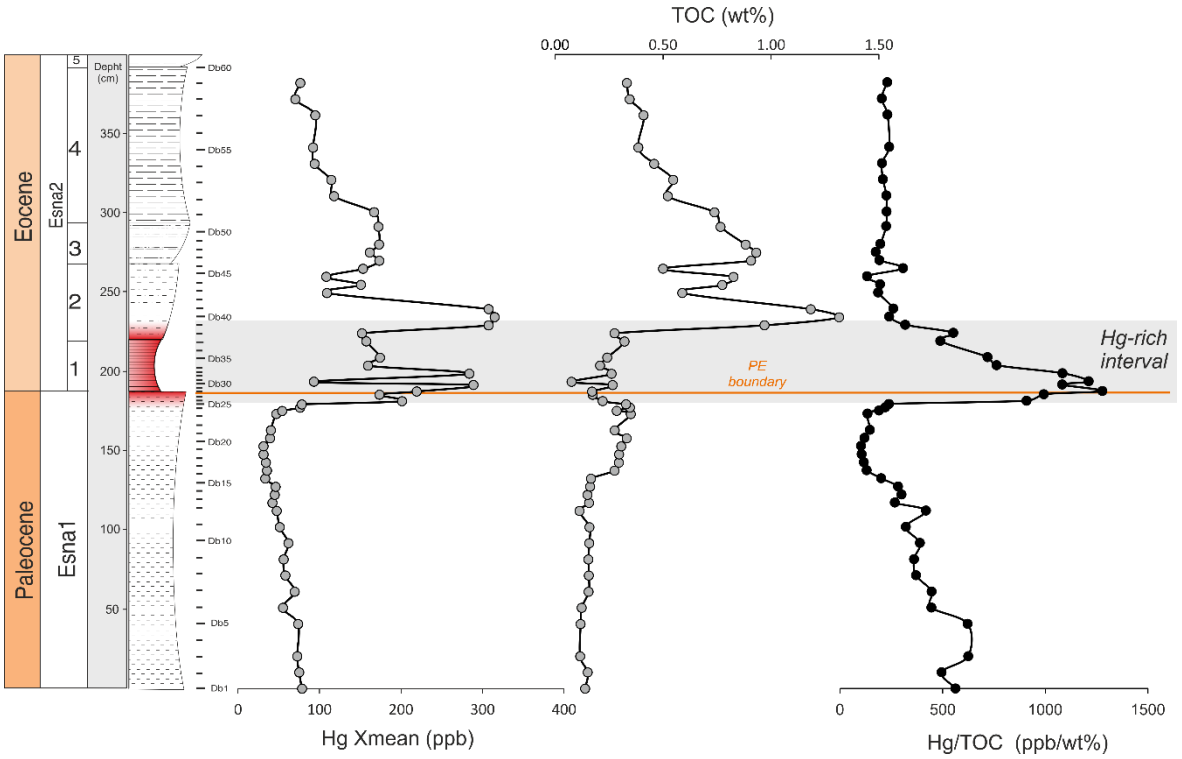

Figure 5.9 – Correlation between mercury concentration (Hg Xmean) and total organic carbon (TOC) along the Dababiya section. The resulting curve (Hg/TOC) shows a Hg-rich level which is not related with the concentration of organic compounds. Data provided by Thierry Adatte.

In order to check a volcanic origin linked to the NAIP for the PETM, I present here mercury data (provided by Thierry Adatte), which reveal that the PETM dissolution interval is also characterized by significant Hg enrichments. Two major Hg anomalies were identified in bed-1 and bed-2 at the Dababiya section (Figure 5.9). The Hg anomaly of bed-2 dissapears after normalization by TOC (Figure 5.9), suggesting that this peak results from organic matter scavenging. On the other hand, the Hg anomaly of bed-1 remains after normalization (Figure 5.9), suggesting that it resulted from higher atmospheric Hg input into the marine realm, rather than organic matter scavenging and/or increased run off. The presence of the Hg peak at the beginning of PETM also supports the role of volcanism (NAIP) to initiate the concomitant warming and sea-level rise that mark the beginning of the PETM.

The PETM interval is characterized by an important negative carbone isotope excursion (CIE), which permits identification and correltion of this event globally. The magnitude and shape of this excursion varies worldwide from abrupt (mostly) to gradual negative shifts. Based on the organic ($\delta^{13}C_{org}$) and inorganic ($\delta^{13}C_{carb}$) carbon isotopes, Khozyem et al. (2015) characterized the CIE at Dababiya in three main phases: 1) gradual decrease, 2) CIE minimum and 3) gradual recovery (Figure 5.10). The inorganic carbon ratio reach minimum values ~60 cm below the PE boundary whereas organic carbon reach the minimum value in the middle of bed-2, ~70 cm above the PE boundary.

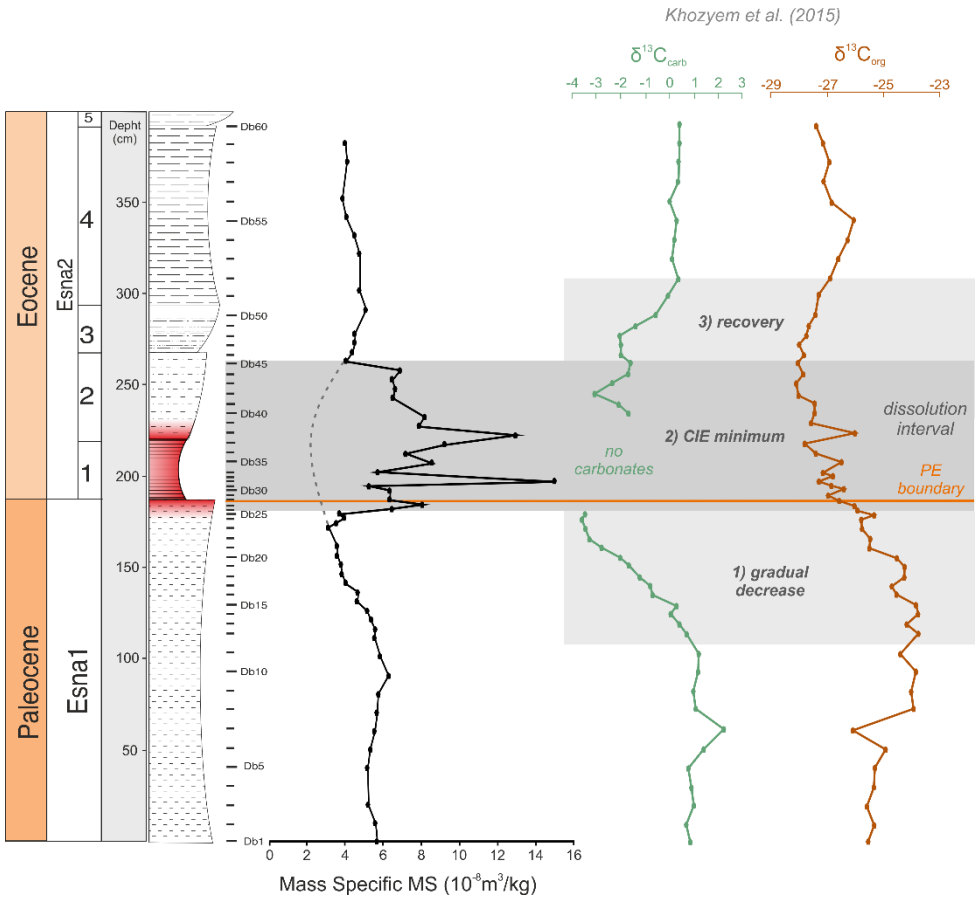

Figure 5.10 – correlation between mass specific magnetic susceptibility (MS) and inorganic ($\delta^{13}C_{carb}$) and organic ($\delta^{13}C_{org}$) carbon isotope data from Khozyem et al. (2015). MS dissolution interval coincides with the minimum values of the CIE that characterize the PETM.

The global decrease in the $\delta^{13}C$ have been related with the destabilization of clathrates stored in the continental shelf, which released large quantities of methane into the water column and atmosphere. Oxidation of the methane species would have produced strongly ^{13}C-depleted CO_2. Consequently, carbonates had precipitated with low $\delta^{13}C$ values, which could account for the $\delta^{13}C_{carb}$ CIE-minimum significantly before the $\delta^{13}C_{org}$ CIE-minimum. Moreover, the oxidation of methane gas had consumed sea water oxygen originating the first anoxia event observed at the base of the PETM interval (Figure 5.8) (Khozyem et al. 2015).

Thre most obvious mechanism for clathrates destabilization is the ocean warming and sea level rise identified in the beginning of the PETM event as consequence of NAIP volcanism Although clathrates are very sensitive to temperature and sea level variations, according with Svensen et al., (2004), a large scale hydrate melting as the one observed in the PETM, recquires a major triggering mechanism, proposing for the first time a link between contact metamorphism and the PETM event. According with Svensen et al. (2004), the intrusion of voluminous mantle-derived melts in carbon-rich sedimentary strata in the northeast Atlantic may have caused an explosive release of methane-transported to the ocean or atmosphere through vent complexes. The authors also found that similar volcanic and metamorphic processes may explain climate events associated with other LIP such as the Siberian Traps and the Karoo Igneous Province.

The ocean warming, the NAIP volcanism and the methane release led to changes in ocean chemistry. Using boron-based proxies for surface ocean carbonate chemistry, Penman et al. (2014) presented the

first evidence for a drop in the pH surface (~0.3 units) and thermocline seawater, which had persisted at least 70 kyr. Zachos et al. (2005) had also reported a significant shoaling of the carbonate compensation depht (CCD) by 2000 m, at five different South Atlantic deep-sea sections.

The delayed $\delta^{13}C_{org}$ CIE-minimum coincides with the maximum content of organic matter (Figures 5.9 and 5.10), which appears to be of terrestrial origin and thus reflects the delayed response of the continental environment to the huge light carbon input into the atmosphere (Khozyem et al. 2015). In fact, the additional CO_2 resulted in global hot humid conditions and increased precipitation (Bolle et al., 2000). Therefore, the resulted weathered terrestrial materials have been carried out to the oceans by streams and fluvial discharges, increasing the input of terrestrial organic matter (Schulte et al., 2011). According with Khozyem et al. (2015), the intensive continental weathering led also to an increase in the nutrients flux from land to the ocean, which associated with ocean surface productivity, activated the biological bump, thus decreasing ocean acidity.

However, the mechanism and rate by which the excess of carbon was removed from the atmosphere and oceans is ambiguous and poorly constrained. The brevity (150-220 kyr) of the PETM event reflects the rapid enhancement of negative feedback mechanisms within Earth's exogenic carbon cycle that served the dual function of buffering ocean pH and reducing atmospheric greenhouse gas levels (Kelly et al., 2005).

One of the most prominent hypotheses in this regard is that a sharp increase in marine biological productivity and an associated increase in export production (flux of biologically produced organic carbon from the surface ocean to the deep ocean) resulted in a drawdown of atmospheric CO2 concentrations (Bains et al., 2000; Zachos & Dickens, 2000; Khozyem et al., 2014, 2015). However, Torfefstein et al. (2010) re-evaluated the "productivity feedback hypothesis", based on biogenic barium mass accumulation rates, and found that any increase export production lagged the initial carbon release by at least ~70 kyr and thus, export production did not facilitate a rapid removal of the excess of carbon from the atmosphere. The authors indicated silicate weathering as the most likely mechanism for carbon removal. On the other hand, Bowen et al. (2010) found that the rate of recovery is an order of magnitude more rapid than that expected for carbon drawdown by silicate weathering alone, suggesting that the accelerated sequestration of organic carbon could reflect the regrowth of carbon stocks in the biosphere or shallow lithosphere that were released at the onset of the event.

The recovery phase of the carbon isotope excursions is coincident with a recovery of goethite concentration and with the return to more oxic conditions (Figures 5.8 and 5.10). Since pyrite crystals found at Dababiya precipitated due to bacterian activity (Khozyem et al., 2015), an increase in biological productivity would be consistent with the increase in pyrite content, which may suffer alteration to form goethite under oxic conditions. Such data reinforces the idea of goethite as an indicator of anoxia in the PETM interval.

The magnetic data and the three phases described above for the $\delta^{13}C$ evolution, correlate well with the biostratigraphy of Dababiya section, which shows major turnovers across the PETM interval (Ernst et al., 2006; Khozyem et al., 2014; Keller et al., 2017). The biostratigraphic zone P5 is coincident with the gradual decrease of the $\delta^{13}C$ values and marks the onset of the PETM, with a 40% increase in planktic foraminifera species diversity (from 21 to 35), but also a slight decrease in the abundance of these species (Figure 5.11) (Khozyem et al., 2014; Keller et al., 2017). Planktic foraminifera and calcareous nannofossils temporarily dissappeared in biostratigraphic zone E1, right above the PE boundary, suggesting warming and surface ocean acidification. Assemblages returned after the PETM interval, in

the carbon isotope excursion recovery phase, with no significant extinctions and underwent evolutionary diversification (Figure 5.11) (Keller et al. 2017). Although an exctinction of benthic foraminifera had been reported during the PETM probably due to the shoal of CCD (Alegret et al., 2009), no significant extinctions were found at Dababiya (Khozyem et al., 2014; Keller et al., 2017).

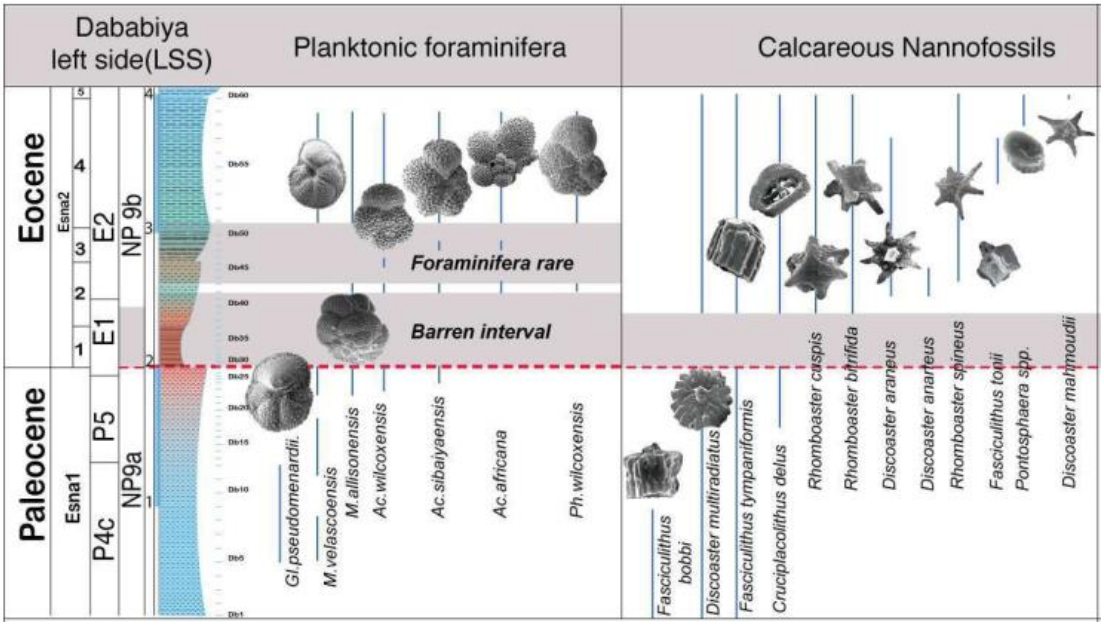

Figure 5.11 – Representative Planktic foraminifera species, calcareous nannofossils and carbon stable isotopes ($\delta^{13}C_{org}$ and $\delta^{13}C_{carb}$) at Dababiya section. Figure from Khozyem et al. (2014).

The magnetic data presented here fully supports the existence of an ocean acidification event starting below the PE boundary. The interval where $\delta^{13}C$ reach minimum values coincides with the PETM interval defined in this project based on MS variations (Figure 5.10), demonstrating the reliability of magnetic data as a proxy to identify important acidification events. In addition, the decrease of goethite during the PETM and its increase during the recovery phase of the carbon isotope excursion, demonstrate that goethite may be a good proxy to identify not only the anoxic conditions in the PETM but also the increase of biological productivity that marks the recovery of the PETM event.

At Zumaia, low contents in detrital magnetite demonstrated to be an excellent proxy to identify environmental acidification on the continent, leading to dissolution of detrital magnetite inland. At Dababiya, such decrease in detrital magnetite is not observed, indicating distinct climate processes. In fact, in the end of Cretaceous period, large quatities of carbon were inputed directly into the atmosphere, leading to environmental acidification via acid rains affecting continental surface. In the PETM, large quantities of carbon were mainly released to the ocean, leading to ocean acidification. The order of magnitude of both acidification events is significantly different because in the oceans, pH is rapidly buffered by carbonate dissolution. Penman et al. (2014), estimated a drop of ~0.3 units in the pH ocean. Such decrease is insufficient to explain magnetite dissolution, which recquires pH values of ~3-4 units (Font et al., 2014; White et al., 1994).

The anomalous interval of magnetite content correlates with foraminifera desappearence, corroborating that severe chemical changes (acidification) occurred in the surface ocean during the PETM. Moreover, magnetic data well correlates with the onset of a mercury anomaly, supporting the rule of volcanism (NAIP) to initiate the PETM event.

5.3 KPg and PETM events: link with the Anthropocene?

The Anthropocene is defined as the geological period where human activity influenced the Earth's climate. Humans have been responsible for recent major alterations of Earth's natural state (Ruddiman, 2008). Climate warming due to fossil fuel burning is indicated as the cause for the increased rate of extreme climate events, melting of polar glaciers and significant rising sea level. Scientists also recognize the accelerated rate of modern species extinctions, arguing that humans are now causing the sixth mass extinction (Barnosky et al., 2011). As rapid reductions in anthropogenic carbon emissions seem increasingly unlikely in the near future, forecasting the Earth systems response to ever-increasing emission rates has become a high-priority focus of climate research.

Geologic analogues from past transient climate changes, such as the KPg mass extinction and the PETM events, could provide invaluable constraints on the response of the present-day climate system. Independently of having different sources (volcanism, methane release or fossil fuel burning), all of these events have in common the massive input of greenhouse gases into the ocean-atmosphere system and consequent climate warming. However, the current climate warming is happening at rates 12 to 16 times faster. The modern rate of change in atmospheric concentration is greater than 200 ppmv per century and is still increasing. Moreover, at current rates of fossil fuel burning, atmospheric CO_2 levels will reach Cretaceous levels of 2 times the pre-industrial level about 2070 and 8 times the pre-industrial level shortly after 2300 (Hay, 2010).

Such data are quite alarming and the first climate consequences from the huge inputs of greenhouse gases linked to human activities are now ongoing. Ozone depletion and particle pollution from fossil fuel burning and other human activities result in dust clouds that trap solar radiation in Earth's atmosphere with lower reflection back to space, thus contributing to increase Earth´s temperature. Similar to the KPg and PETM events, present-day CO_2 concentrations from the atmosphere are absorbed in the oceans and has already lowered the pH. Ocean acidification is already affecting shelly organisms at the base of the food chain and endangering all life up to the food chain (Keller et al., 2017).

Based on the KPg and PETM geological records, two future scenarios can be presumed. The worst-case scenario is the one similar to the KPg, when the environmental changes led to a severe mass extinction. Since the actual greenhouse input rates are much higher than the ones estimated for the Cretaceous, a future mass extinction would be expected to happen with a faster rate. The best-case scenario would be similar to the PETM event, where no significant extinctions were reported. Nevertheless, the Earth would suffer a period of extreme environmental stress marked by intense heat, extreme climate events, rising sea level and severe food shortages reducing population and forcing migration to higher latitudes for survival (Keller et al., 2017).

According to Ruddiman (2008), we are now ~0.7ºC of the way into this huge new experiment in transforming our planet. Political and social efforts have been made to reduce the greenhouse gas emissions in some countries. The possibility of altering Earth´s future climate by engineering has also been discussed in the scientific community specially during the last decade (Figueroa et al., 2007; Getter et al. 2009; Szulczewki et al., 2012; Li et al., 2013). Unless technology or extreme conservation efforts intervene, Earth is headed toward a warmer future at rates that are unprecedented in its 4.5-billion-year history.

6. Conclusions

The magnetic results obtained for both sections, Zumaia and Dababiya, correlate very well with biostratigraphic, mineralogical and geochemical data from previous studies at different sections worldwide, demonstrating not only the reliability of the data as well as the global dimension of both events.

The magnetic data acquired in this project provided new insights to identify periods of severe environmental change in the global sedimentary record as well as new constrains about the KPg and PETM events:

(i) Magnetic susceptibility revealed to be a good proxy to identify important acidification events.
(ii) Abnormally low contents of detrital magnetite at Zumaia are likely the result of continental magnetite dissolution by acid rains.
(iii) A change in seawater/sediment chemistry due environmental acidification would suppress the development of magnetotatic bacteria in the interval below the KPg.
(iv) Several proxies such as akageneite, Hg-rich levels, $^{187}Os/^{188}Os$ and atmospheric CO_2 pressure link the low susceptibility interval found at Zumaia with an acceleration of eruption rates of the Deccan volcanism recently dated with accuracy by U-Pb dating zircon.
(v) Contrary to Gubbio and Bidart, the magnetite depleted interval found at Zumaia (as well as the occurrence of akaganéite) encompasses the KPg boundary, reinforcing the contribution of the Deccan volcanism to the KPg mass extinction.
(vi) Overall, the magnetic data acquired for Zumaia section corroborates the existence of a severe period of environmental changes prior to the KPg boundary, which certainly contributed to the Cretaceous mass extinction. The impact that succeeded such climate changes, likely exacerbated climate warming and may have intensified Deccan eruptions. However, precise contribution of each catastrophic event in the massive extinction of the end of the Cretaceous period is still under debate.
(vii) Dababiya MS interval correlates with the CIE-minimum phase and calcite and foraminifera disappearance, supporting an ocean acidification starting below the PE boundary.
(viii) Mercury enrichments at the beginning of PETM together with negative excursions of $^{187}Os/^{188}Os$ supports the role of volcanism (NAIP) to initiate the concomitant warming and sea level rise that mark the beginning of the PETM.
(ix) Low contents of goethite in the PETM interval are indicative of pyrite preservation due to lithological contrast. However, high contents of goethite above the PETM interval support the increase in biological productivity theory as the main feedback mechanism leading to the end of PETM event, and therefore represent a good indicator of anoxia.
(x) Higher values of magnetite are the result of low calcite/high detrital interval that characterizes the PETM.
(xi) Concentration patterns of detrital magnetite indicate that, although both events (KPg and PETM) were triggered by a massive release of CO_2, the resulted climate processes were distinct.
(xii) Similar (or even more severe) climate changes of those occurred at the KPg and PETM are expected to occur in the future, unless technology or extreme conservation efforts intervene.

7. References

Abrajevitch, A., Font, E., Florindo, F. & Roberts, A. P. (2015). Asteroid impact vs. Deccan eruptions: The origin of low magnetic susceptibility beds below the Cretaceous-Paleogene boundary revisited. Earth and Planetary Science Letters 430 (2015) 209–223.

Alegret, L., Ortiz, S. & Molina, E. (2009). Extinction and recovery of benthic foraminifera across the Paleocene–Eocene Thermal Maximum at the Alamedilla section (Southern Spain). Palaeogeography, Palaeoclimatology, Palaeoecology, v.279, pp.186–200.

Alvarez, L.W., Alvarez, W., Asaro, F. & Michel, H.V. (1980). Extraterrestrial cause for the Cretaceous–Tertiary extinction. Science 208, 1095–1108.

Aubry, M. P., Ouda, K., Dupuis, C., Berggren, W. A. & Couvering, J. A. V. (2007). The Global Standard Stratotype-section and Point (GSSP) for the base of the Eocene Series in the Dababiya section (Egypt). Episodes, 30(4), 271.

Bains, S., Norris, R.D., Corfield, R.M. & Faul, K.L. (2000). Termination of global warmth at the Palaeocene/Eocene boundary through productivity feedback. Nature 407, 171–174.

Barnosky, A. D., Matzke, N., Tomiya, S., Wogan, G. O., Swartz, B., Quental, T. B., Marshall, C., McGuire, J. L., Lindsey, E. L., Maguire, K. C., Mersey, B. & Ferrer, E. A. (2011). Has the Earth's sixth mass extinction already arrived?. *Nature, 471*(7336), 51.

Batenburg, S. J., Sprovieri, M., Gale, A. S., Hilgen, F. J., Hüsing, S., Laskar, J., Liebrand, D., Lirer, F., Orue-Etxebarria, X., Pelosi, N. & Smit, J. (2012). Cyclostratigraphy and astronomical tuning of the Late Maastrichtian at Zumaia (Basque country, Northern Spain). Earth and Planetary Science Letters, 359, 264-278.

Batenburg, S.J., Gale, A.S., Sprovieri, M., Hilgen, F.J., Thibault, N., Boussaha, M. & OrueEtxebaria, X. (2014). An astronomical time scale for the Maastrichtian based on the Zumaia and Sopelana sections (Basque country, northern Spain). J. Geol. Soc. London 171, 165–180.

Berggren, W. A., & Ouda, K. (2003). Upper Paleocene-lower Eocene planktonic foraminiferal biostratigraphy of the Dababiya section, Upper Nile valley (Egypt). Micropaleontology, 49(Suppl 1), 61-92.

Bernaola, G., Martín-Rubio, M., & Baceta, J. I. (2009). New high resolution calcareous nannofossil analysis across the Danian/Selandian transition at the Zumaia section: comparison with South Tethys and Danish sections. Geologica Acta: an international earth science journal, 7(1-2).

Bloemendal, J., King, J. W., Hall, F.R. & Doh, S.-J. (1992). Rock magnetism of Late Neogene and Pleistocene deep-sea sediments: Relationship to sediment source, diagenetic processes and sediment lithology. J. Geophys, Res., 97, 4361-4375.

Bolle, M. P., Pardo, A., Adatte, T., Tantawy, A. A., Hinrichs, K. U., Von Salis, K. & Burns, S. (2000). Climatic evolution on the southern and northern margins of the Tethys from the Paleocene to the early Eocene. *GFF*, *122*(1), 31-32.

Bowen, G.J., Clyde, W.C., Koch, P.L., Ting, S., Alroy, J., Tsubamoto, T., Wang, Y. & Wang, Y. (2002). Mammalian dispersal at the Paleocene/Eocene boundary. Science, v. 295, pp. 2062–2065.

Bowen, G. J., & Zachos, J. C. (2010). Rapid carbon sequestration at the termination of the Palaeocene–Eocene Thermal Maximum. *Nature Geoscience*, *3*(12), 866.

Carvallo, C., Muxworthy, A. R., Dunlop, D. J. & Williams, W. (2003). Micromagnetic modeling of first-order reversal curve (FORC) diagrams for single-domain and pseudo-single-domain magnetite. Earth and Planetary Science Letters, 213(3), 375-390.

Channell, J. E. T. & McCabe, C. (1994). Comparison of magnetic hysteresis parameters of unremagnetized and remagnetized limestones, J. Geophys. Res., 99, 4613– 4623.

Chenet, A.-L., Quidelleur, X., Fluteau, F., Courtillot, V. & Bajpai, S. (2007). 40K/40Ar dating of the main Deccan large igneous province: Further evidence of KTB age and short duration: Earth and Planetary Science Letters, v. 263, p. 1–15.

Chenet, A.-L., Fluteau, F., Courtillot, V., Gerard, M. & Subbarao, K.V. (2008). Determination of rapid Deccan eruptions across the CretaceousTertiary boundary using paleomagnetic secular variation: Results from a 1200-m-thick section in the Mahabaleshwar: Journal of Geophysical Research, v. 113, B04101.

Chenet, A.-L., Courtillot, V., Fluteau, F., Gerard, M., Quidelleur, X., Khadri, S.F.R., Subbarao, K.V., & Thordarson, T. (2009). Determination of rapid Deccan eruptions across the Cretaceous-Tertiary boundary using paleomagnetic secular variation: 2. Constraints from analysis of eight new sections and synthesis for a 3500-m-thick composite section: Journal of Geophysical Research, v. 114, B06103.

Cohen, A. S., & Coe, A. L. (2002). New geochemical evidence for the onset of volcanism in the Central Atlantic magmatic province and environmental change at the Triassic-Jurassic boundary. *Geology*, *30*(3), 267-270.

Correia, J. M. F. (2010). O Limite Cretácico-Paleogénico: Alterações climáticas e Crises Biológicas. Tese de Mestrado em Ciências Geofísicas, especialização em Meteorologia. Faculdade de Ciências – Universidade de Lisboa, Lisboa. 17 pp.

Courtillot, V., Besse, J., Vandamme, D., Montigny, R., Jaeger, J.-J., & Cappetta, H. (1986). Deccan flood basalts at the Cretaceous/Tertiary boundary?. Earth and Planetary Science Letters, v. 80, p. 361–374.

Courtillot, V. (2003). Evolutionary catastrophes: the science of mass extinction. Cambridge University Press.

Courtillot, V. & Renne, J. (2003). On the ages of flood basalt events. C. R. Acad. Sci. Paris 335, 113–140.

Crick, R. E., Ellwood, B. B., Hladil, J., El Hassani, A., Hrouda, F., & Chlupac, I. (2001). Magnetostratigraphy susceptibility of the Přídolian–Lochkovian (Silurian–Devonian) GSSP (Klonk, Czech Republic) and a coeval sequence in Anti-Atlas Morocco. Palaeogeography, Palaeoclimatology, Palaeoecology, 167(1), 73-100.

Dearing, J. A., Environmental Magnetic Susceptibility. (1994). 1st edition.

Dickin, A. P. (2005). Radiogenic isotope geology. Cambridge University Press.

Dinares-Turell, J., Baceta, J.I., Pujalte, V., Orue-Etxebarria, X., Bernaola, G. & Lorito, S. (2003). Untangling the Palaeocene climatic rhythm: an astronomically calibrated Early Palaeocene magnetostratigraphy and biostratigraphy at Zumaia (Basque basin, northern Spain). Earth Planet. Sci. Lett. 216, 483–500.

Dinarès-Turell, J., Pujalte, V., Stoykova, K., & Elorza, J. (2013). Detailed correlation and astronomical forcing within the Upper Maastrichtian succession in the Basque Basin. Boletín Geológico y Minero, 124(2), 253-282.

Dupuis, C., Aubry, M. P., Steurbaut, E., Berggren, W. A., Ouda, K., Magioncalda, R., Cramer, B. J., Kent, D. V., Speijer, R. P. & Heilmann-Clausen, C. (2003). The Dababiya Quarry Section: Lithostratigraphy, clay mineralogy, geochemistry and paleontology. Micropaleontology, 49 (Suppl 1), 41-59.

Egli, R. (2003). Analysisofthe field dependence of remanent magnetization curves. J. Geophys. Res. 108, 2081.

Egli, R. (2004). Characterization of individual rock magnetic components by analysis of remanence curves. 3. Bacterial magnetite and natural processes in lakes. Phys. Chem. Earth 29, 869–884.

Egli, R. (2013). VARIFORC: An optimized protocol for calculating non-regular first-order reversal curve (FORC) diagrams. Global Planet Change 110, 302-320.

Egli, R., Chen, A. P., Winklhofer, M., Kodama, K. P., & Horng, C. S. (2010). Detection of noninteracting single domain particles using first-order reversal curve diagrams. Geochemistry, Geophysics, Geosystems, 11(1).

Ellwood, B., Tomkin, J., Ratcliffe, K., Wright, M. & Kafafy, A. (2008). High-resolution magnetic susceptibility and geochemistry for the Cenomanian-Turonian boundary GSSP with correlation to time equivalent core. Palaeogeography, Palaeoclimatology, Palaeoecology, 261, 105–126.

Ellwood, B., MacDonald, W., Wheeler, C. & Benoist, S. (2003). The K -T boundary in Oman: identified using magnetic susceptibility field measurements with geochemical confirmation.
Earth and Planetary Science Letters, 206, 529-540.

Ernst, S. R., Guasti, E., Dupuis, C. & Speijer, R. P. (2006). Environmental perturbation in the southern Tethys across the Paleocene/Eocene boundary (Dababiya, Egypt): Foraminiferal and clay mineral records. *Marine Micropaleontology*, *60*(1), 89-111.

Figueroa, J. D., Fout, T., Plasynski, S., McIlvried, H., & Srivastava, R. D. (2008). Advances in CO2 capture technology—the US Department of Energy's Carbon Sequestration Program. *International journal of greenhouse gas control*, *2*(1), 9-20.

Font, E., Trindade, R. I. F., & Nédélec, A. (2006). Remagnetization in bituminous limestones of the Neoproterozoic Araras Group (Amazon craton): hydrocarbon maturation, burial diagenesis, or both?. *Journal of Geophysical Research: Solid Earth*, *111*(B6).

Font, E., Nedelec, A., Ellwood, B.B., Mirão, J. & Silva, P.F. (2011). A new sedimentary benchmark for the Deccan Traps volcanism?. Geophysical Research Letters, v. 38, p. L24309.

Font, E., Fabre, S., Nédélec, A., Adatte, T., Keller, G., Veiga-Pires, C., Ponte, J., Mirão, J., Khozyem, H. & Spangenberg, J. E. (2014). Atmospheric halogen and acid rains during the main phase of Deccan eruptions: Magnetic and mineral evidence. Geological Society of America Special Papers, 505, SPE505-18.

Font, E., Carlut, J., Remazeilles, C., Mather, T.A., Nedelec, A., Mirao, J. & Casale, S. (2017). End-Cretaceous akaganeite as a mineral marker of Deccan volcanism in the sedimentary record. Sci. Rep. 7, 11453.

Font, E., Adatte, T., Andrade, M., Keller, G., Bitchong, A. M., Carvallo, C., Ferreira, J., Diogo, Z. & Mirão, J. (2018). Deccan volcanism induced high-stress environment during the Cretaceous–Paleogene

transition at Zumaia, Spain: Evidence from magnetic, mineralogical and biostratigraphic records. Earth and Planetary Science Letters, 484, 53-66.

Foreman, B. Z., Heller, P. L. & Clementz, M. T. (2012). Fluvial response to abrupt global warming at the Palaeocene/Eocene boundary. Nature, 491(7422), 92.

Getter, K. L., Rowe, D. B., Robertson, G. P., Cregg, B. M., & Andresen, J. A. (2009). Carbon sequestration potential of extensive green roofs. *Environmental science & technology*, *43*(19), 7564-7570.

Gubbins, D. & Herrero-Bervera, E. (Eds.). (2007). Encyclopedia of geomagnetism and paleomagnetism. Springer Science & Business Media.

Hay, W. W. (2011). Can humans force a return to a 'Cretaceous' climate?. *Sedimentary Geology*, *235*(1-2), 5-26.

Jackson, M. (1990). Diagenetic sources of stable remanence in remagnetized paleozoic cratonic carbonates: A rock magnetic study. J. Geophys. Res., 95, 2753– 2762.

Jackson, M., Sun, W. W. & Craddock, J. P. (1992). The rock magnetic fingerprint of chemical remagnetization in midcontinental Paleozoic carbonates, Geophys. Res. Lett., 19, 781– 784.

Jackson, M., Rochette, P., Fillilon, G., Banerjee, S. & Marvin, J. (1993). Rock magnetism of remagnetized Paleozoic carbonates: Low temperature behavior and susceptibility characteristics, J. Geophys. Res., 98, 6217 – 6225.

Keller, G., Barrera, E., Schmitz, B., & Mattson, E. (1993). Gradual mass extinction, species survivorship, and long-term environmental changes across the Cretaceous-Tertiary boundary in high latitudes. *Geological Society of America Bulletin*, *105*(8), 979-997.

Keller, G., Li, L., & MacLeod, N. (1995). The Cretaceous/Tertiary boundary stratotype section at El Kef, Tunisia: how catastrophic was the mass extinction?. *Palaeogeography, Palaeoclimatology, Palaeoecology*, *119*(3-4), 221-254.

Keller, G., Adatte, T., Gardin, S., Bartolini, A. & Bajpai, S. (2008). Main Deccan volcanism phase ends near the K-T boundary: Evidence from the Krishna-Godavari Basin, SE India: Earth and Planetary Science Letters, v. 268, p. 293–311.

Keller, G., Adatte, T., Bajpai, S., Mohabey, D.M., Widdowson, M., Khosla, A., Sharma, R., Khosla, S.C., Gertsch, B., Fleitmann, D. & Sahni, A. (2009a). K-T transition in Deccan Traps and intertrappean beds in central India mark major marine seaway across India: Earth and Planetary Science Letters, v. 282, p. 10–23.

Keller, G., Khosla, S.C., Sharma, R., Khosla, A., Bajpai, S., & Adatte, T. (2009b). Early Danian planktic foraminifera from Cretaceous-Tertiary inter trappean beds at Jhilmili, Chhindwara District, Madhya Pradesh, India: Journal of Foraminiferal Research, v. 39, no. 1, p. 40–55.

Keller, G., Sahni, A., & Bajpai, S. (2009c). Deccan volcanism, the KT mass extinction and dinosaurs: Journal of Biosciences, v. 34, p. 709–728.

Keller, G., Bhowmick, P.K., Upadhyay, H., Dave, A., Reddy, A.N., Jaiprakash, B.C. & Adatte, T. (2011). Deccan volcanism linked to the CretaceousTertiary boundary (KTB) mass extinction: New evidence from ONGC wells in the Krishna-Godavari Basin, India: Journal of the Geological Society of India, v. 78, p. 399–428.

Keller, G., Adatte, T., Bhowmick, P.K., Upadhyay, H., Dave, A., Reddy, A.N., & Jaiprakash, B.C. (2012). Nature and timing of extinctions in Cretaceous-Tertiary planktic foraminifera preserved in Deccan intertrappean sediments of the Krishna-Godavari Basin, India: Earth and Planetary Science Letters, v. 341–344, p. 211–221.

Keller, G. (2014). Deccan volcanism, the Chicxulub impact, and the end-Cretaceous mass extinction: Coincidence? Cause and effect? Spec. Pap., Geol. Soc. Am., vol. 505, pp. 57–89.

Keller, G., Mateo, P., Punekar, J., Khozyem, H., Gertsch, B., Spangenberg, J., Bitchong, A. M. & Adatte, T. (2017). Environmental changes during the Cretaceous-Paleogene mass extinction and Paleocene-Eocene Thermal Maximum: Implications for the Anthropocene. *Gondwana Research*, *56*, 69-89.

Kelly, D. C., Zachos, J. C., Bralower, T. J. & Schellenberg, S. A. (2005). Enhanced terrestrial weathering/runoff and surface ocean carbonate production during the recovery stages of the Paleocene-Eocene thermal maximum. *Paleoceanography and Paleoclimatology*, *20*(4).

Kemp, S. J., Ellis, M. A., Mounteney, I., & Kender, S. (2016). Palaeoclimatic implications of high-resolution clay mineral assemblages preceding and across the onset of the Palaeocene–Eocene Thermal Maximum, North Sea Basin. Clay Minerals, 51(5), 793-813.

Khozyem, H., Adatte, T., Spangenberg, J.E., Tantawy, A.A. & Keller, G. (2013). Paleoenvironmental and climatic changes during the Paleocene-Eocene Thermal Maximum (PETM) at the Wadi Nukhul Section, Sinai, Egypt. J. Geol. Soc. Lond. 170, 341–352.

Khozyem, H., Adatte, T., Keller, G., Tantawy, A. A., & Spangenberg, J. E. (2014). The Paleocene-Eocene GSSP at Dababiya, Egypt-Revisited. *Episodes*, *37*(2), 78-86.

Khozyem, H., Adatte, T., Spangenberg, J. E., Keller, G., Tantawy, A. A., & Ulianov, A. (2015). New geochemical constraints on the Paleocene–Eocene thermal maximum: Dababiya GSSP, Egypt. Palaeogeography, Palaeoclimatology, Palaeoecology, 429, 117-135.

Knight, K.B., Renne, P.R., Halkett, A. & White, N. (2003). 40Ar/ 39Ar dating of the Rajahmundry Traps, eastern India and their relationship to the Deccan traps. Earth Planet. Sci. Lett. 208, 85–99.

Knight, K.B., Renne, P.R., Baker, J., Waight, T. & White, N. (2005). Reply to '40Ar/39Ar dating of the Rajahmundry Traps, Eastern India and their relationship to the Deccan Traps: Discussion' by A.K. Baksi. Earth Planet. Sci. Lett. 239, 374–382.

Kruiver, P. P., Dekkers, M. J. & Heslop, D. (2001). Quantification of magnetic coercivity components by the analysis of acquisition curves of isothermal remanent magnetisation. Earth and Planetary Science Letters, 189(3), 269-276.

Li, B., Duan, Y., Luebke, D., & Morreale, B. (2013). Advances in CO2 capture technology: A patent review. *Applied Energy*, *102*, 1439-1447.

Li, L., & Keller, G. (1998). Abrupt deep-sea warming at the end of the Cretaceous. *Geology*, *26*(11), 995-998.

Lowrie, W., W. Alvarez, & F. Asaro (1990), The origin of the white beds below the Cretaceous-Tertiary boundary in the Gubbio section, Italy, Earth Planet. Sci. Lett., 98, 303–312.

Luciani, V., Giusberti, L., Agnini, C., Backman, J., Fornaciari, E., & Rio, D. (2007). Paleocene– Eocene Thermal Maximum as recorded by Tethyan planktonic foraminifera in the Forada section (northern Italy). Marine Micropaleontology, v.64, pp.189-214.

Maxbauer, D.P., Feinberg, J.M. & Fox, D.L. (2016). MAX UnMix: A web application for unmixing magnetic coercivity distributions. Comput Geosci-Uk 95, 140-145.

Meléndez, A. & Molina, E. (2008). The Cretaceous-Tertiary (KT) boundary. In: A. García-Cortés et al. eds. Contextos geológicos españoles. Publicaciones del Instituto Geológico y Minero de España. 107-113.

Muxworthy, A. R., & Dunlop, D. J. (2002). First-order reversal curve (FORC) diagrams for pseudo-single-domain magnetites at high temperature. Earth and Planetary Science Letters, 203(1), 369-382.

Nordt, L., Atchley, S., & Dworkin, S. (2003). Terrestrial evidence for two greenhouse events in the latest Cretaceous. *GSA today*, *13*(12), 4-9.

Payros, A., Pujalte, V., Orue-Etxebarria, X., Apellaniz, E., Bernaola, G., Baceta, J. I., Caballero, F., Dinarès-Turrel, J., Monechi, S., Ortiz, S., Schmitz, B. & Tosquella, J. (2016). The Relevance of Iberian Sedimentary Successions for Paleogene Stratigraphy and Timescales. In Stratigraphy & Timescales (Vol. 1, pp. 393-489). Academic Press.

Penman, D. E., Hönisch, B., Zeebe, R. E., Thomas, E., & Zachos, J. C. (2014). Rapid and sustained surface ocean acidification during the Paleocene-Eocene Thermal Maximum. Paleoceanography, 29(5), 357-369.

Percival, L.M.E., Cohen, A.S., Davies, M.K., Dickson, A.J., Hesselbo, S.P., Jenkyns, H.C., Leng, M.J., Mather, T.A., Storm, M.S. & Xu, W. (2016). Osmium isotope evidence for two pulses of increased continental weathering linked to Early Jurassic volcanism and climate change. Geology 44, 759–762.

Pérez-Rodríguez, I., Lees, J. A., Larrasoaña, J. C., Arz, J. A. & Arenillas, I. (2012). Planktonic foraminiferal and calcareous nannofossil biostratigraphy and magnetostratigraphy of the uppermost Campanian and Maastrichtian at Zumaia, northern Spain. Cretaceous Research, 37, 100-126.

Pike, C. R., Roberts, A. P. & Verosub, K. L. (1999). Characterizing interactions in fine magnetic particle systems using first order reversal curves. Journal of Applied Physics, 85(9), 6660-6667.

Ponte, J. M. N. (2013). Magnetic mineralogy of Cretaceous-Tertiary sections (Tethys, Iran and India): links with the Deccan Phase-2. Tese de Mestrado em Ciências Geofísicas, especialização em Geofísica Interna. Faculdade de Ciências – Universidade de Lisboa, Lisboa.

Punekar, J., Keller, G., Khozyem, H. M., Adatte, T., Font, E., & Spangenberg, J. (2016). A multi-proxy approach to decode the end-Cretaceous mass extinction. *Palaeogeography, Palaeoclimatology, Palaeoecology*, *441*, 116-136.

Renne, P.R., Deino, A.L., Hilgen, F.J., Kuiper, K.F., Mark, D.F., Mitchell, W.S., Morgan, L.E., Mundil, R., & Smit, J. (2013). Time scales of critical events around the Cretaceous-Paleogene boundary. Science, v. 339, p. 684–687.

Renne, P. R., Sprain, C. J., Richards, M. A., Self, S., Vanderkluysen, L., & Pande, K. (2015). State shift in Deccan volcanism at the Cretaceous-Paleogene boundary, possibly induced by impact. *Science*, *350*(6256), 76-78.

Roberts, A. P., Pike, C. R., & Verosub, K. L. (2000). First-order reversal curve diagrams: A new tool for characterizing the magnetic properties of natural samples. Journal of Geophysical Research: Solid Earth, 105(B12), 28461-28475.

Roberts, A.P., Florindo, F., Villa, G., Chang, L., Jovane, L., Bohaty, S.M., Larrasoana, J.C., Heslop, D. & Gerald, J.D.F. (2011). Magnetotactic bacterial abundance in pelagic marine environments is limited by organic carbon flux and availability of dissolved iron. Earth Planet. Sci. Lett. 310, 441–452.

Roberts, A.P., Heslop, D., Zhao, X. & Pike, C.R. (2014). Understanding fine magnetic particle systems through use of first-order reversal curve diagrams. Rev. Geo-phys.52, 557–602.

Robertson, D. J., & France, D. E. (1994). Discrimination of remanence-carrying minerals in mixtures, using isothermal remanent magnetisation acquisition curves. Physics of the Earth and Planetary interiors, 82(3-4), 223-234.

Robinson, N., Ravizza, G., Coccioni, R., Peucker-Ehrenbrink, B. & Norris, R. (2009). A high-resolution marine 187 Os/188 Os record for the late Maastrichtian: Distinguishing the chemical fingerprints of Deccan volcanism and the KP impact event. *Earth and Planetary Science Letters*, *281*(3), 159-168.

Ruddiman, W. F. (2008). Earth's Climate, Past and Future. Second Edition.

SAID, R. (1960). Planktonic foraminifera from the Thebes Formation, Luxor, Egypt. Micropaleontology, 8 (3): 277-286.

Saleh, H. M. A. K. (2013). Sedimentology, geochemistry and mineralogy of the Paleocene-Eocene Thermal Maximum (PETM): sediment records from Egypt, India and Spain. Faculté des géosciences et de l'environnement Université de Lausanne Géopolis CH-1015 Lausanne SUISSE: Université de Lausanne, Faculté des géosciences et de l'environnement.

Schoene, B., Samperton, K. M., Eddy, M. P., Keller, G., Adatte, T., Bowring, S. A., Syed, F., Khadri, R & Gertsch, B. (2014). U-Pb geochronology of the Deccan Traps and relation to the end-Cretaceous mass extinction. *Science*, *347*(6218), 182-184.

Schulte, P., Alegret, L., Arenillas, I., Arz, J. A., Barton, P.J., Bown, P.R., Bralower, T.J., Christeson, G.L., Claeys, P., Cockell, C.S., Collins, G.S., Deutsch, A., Goldin, T.J., Goto, K., Grajales-Nishimura, J.M., Grieve, R.A.F., Gulick, S.P.S., Johnson, K.R., Kiessling, W., Koeberl, C., Kring, D.A., MacLeod, K.G., Matsui, T., Melosh, J., Montanari, A., Morgan, J.V., Neal, C.R., Nichols, D.J., Norris, R.D., Pierazzo, E., Ravizza, G., Rebolledo-Vieyra, M., Reimold, W.U., Robin, E., Salge, T., Speijer, R.P., Sweet, A.R., Urrutia-Fucugauchi, J., Vajda, V., Whalen, M.T. & Willumsen, P.S. (2010). The Chicxulub asteroid impact and mass extinction at the Cretaceous Paleogene boundary. Science 327, 1214–1218.

Schulte, P., Scheibner, C., & Speijer, R. (2011). Fluvial discharge and sea-level changes controlling black shale deposition during the Paleocene–Eocene Thermal Maximum in the Dababiya Quarry section, Egypt: Chemical Geology, v.285, pp. 167-183.

Schulte, P., Schwark, L., Stassen, P., Kouwenhoven, T. J., Bornemann, A., & Speijer, R. P. (2013). Black shale formation during the Latest Danian Event and the Paleocene–Eocene Thermal Maximum in central Egypt: Two of a kind?. *Palaeogeography, palaeoclimatology, palaeoecology*, *371*, 9-25.

Sharma, M., Wasserburg, G. J., Hofmann, A. W. & Butterfield, D. A. (2000). Osmium isotopes in hydrothermal fluids from the Juan de Fuca Ridge. *Earth Planet. Sci. Lett.* 179, 139–52.

Sluijs, A., Brinkhuis, H., Schouten, S., Bohaty, S. M., John, C. M., Zachos, J. C., Reichart, G. J., Damsté, J. S. S., Crouch, E. M. & Dickens, G. R. (2007). Environmental precursors to rapid light carbon injection at the Palaeocene/Eocene boundary. Nature, 450(7173), 1218.

Sluijs, A., Brinkhuis, H., Crouch, E. M., John, C. M., Handley, L., Munsterman, D., Bohaty, S. M., Zachos, J. C., Reichart, G. J., Schouten, S., Pancost, R. D., Damsté, J. S. S., Welters, N. L. D., Lotter,

A. F. & Dickens, G. R. (2008). Eustatic variations during the Paleocene-Eocene greenhouse world. *Paleoceanography and Paleoclimatology*, *23*(4).

Smit, J., & Hertogen, J. (1980). An extraterrestrial event at the Cretaceous–Tertiary boundary. Nature, 285(5762), 198.

Speijer, R., & Wagner, T. (2002). Sea-level changes and black shales associated with the late Paleocene thermal maximum: Organic-geochemical and micropaleontologic evidence from the southern Tethyan margin (Egypt-Israel). In *Catastrophic events and mass extinctions: Impacts and beyond* (pp. 533-549). Geological Society of America, Boulder, Colorado.

Svensen, H., Planke, S., Malthe-Sørenssen, A., Jamtveit, B., Myklebust, R., Eidem, T. R., & Rey, S. S. (2004). Release of methane from a volcanic basin as a mechanism for initial Eocene global warming. *Nature*, *429*(6991), 542.

Szulczewski, M. L., MacMinn, C. W., Herzog, H. J., & Juanes, R. (2012). Lifetime of carbon capture and storage as a climate-change mitigation technology. *Proceedings of the National Academy of Sciences*, *109*(14), 5185-5189.

Ten Kate, W. G., & Sprenger, A. (1993). Orbital cyclicities above and below the Cretaceous/Paleogene boundary at Zumaya (N Spain), Agost and Relleu (SE Spain). Sedimentary Geology, 87(1-2), 69-101.

Thompson, R., Oldfield, F. (1986). Environmental Magnetism, Allen & Unwin, London.

Thomas, D. J., Zachos, J. C., Bralower, T. J., Thomas, E., & Bohaty, S. (2002). Warming the fuel for the fire: Evidence for the thermal dissociation of methane hydrate during the Paleocene-Eocene thermal maximum. *Geology*, *30*(12), 1067-1070.

Torfstein, A., Winckler, G. & Tripati, A. (2010). Productivity feedback did not terminate the Paleocene–Eocene Thermal Maximum (PETM). Clim. Past 6, 265–272.

Tripati, A. K., & Elderfield, H. (2004). Abrupt hydrographic changes in the equatorial Pacific and subtropical Atlantic from foraminiferal Mg/Ca indicate greenhouse origin for the thermal maximum at the Paleocene-Eocene Boundary. *Geochemistry, Geophysics, Geosystems*, *5*(2).

Turgeon, S. C., & Creaser, R. A. (2008). Cretaceous oceanic anoxic event 2 triggered by a massive magmatic episode. *Nature*, *454*(7202), 323.

Ward, P.D. & Kennedy, W.J. (1993). Maastrichtian ammonites from the Biscay Region (France, Spain). Journal of Paleontology Memoir, 34, 1–58

Westerhold, T., Röhl, U., McCarren, H. & ZachoS, J. (2009). Latest on the absolute age of the Paleocene–Eocene Thermal Maximum (PETM): new insights from exact stratigraphic position of key ash layers +19 and -17. Earth and Planetary Science Letters, 287, 412–419.

Wiedmann, J. (1988). The Basque coastal sections of the K/T boundary – A key to understanding "mass extinctions" in the fossil record. No. Extraordinario. In: Lamolda, M.A., Kauffman, E.G.,Walliser, O.H. (eds.), Paleontology and Evolution: Extinction Events. Revista Española de Paleontología, 127–140.

Wilf, P., Johnson, K. R., & Huber, B. T. (2003). Correlated terrestrial and marine evidence for global climate changes before mass extinction at the Cretaceous–Paleogene boundary. *Proceedings of the National Academy of Sciences*, *100*(2), 599-604.

Zachos, J. C., & Dickens, G. R. (2000). An assessment of the biogeochemical feedback response to the climatic and chemical perturbations of the LPTM. *Gff*, *122*(1), 188-189.

Zachos, J. C., Röhl, U., Schellenberg, S. A., Sluijs, A., Hodell, D. A., Kelly, D. C., Thomas, E., Nicolo, M., Raffi, I., Lourens, L. J., McCarren, H. & Kroon, D. (2005). Rapid acidification of the ocean during the Paleocene-Eocene thermal maximum. *Science*, *308*(5728), 1611-1615.

Zachos, J. C., Schouten, S., Bohaty, S., Quattlebaum, T., Sluijs, A., Brinkhuis, H., Gibbs, S.J. & Bralower, T. J. (2006). Extreme warming of mid-latitude coastal ocean during the Paleocene-Eocene Thermal Maximum: Inferences from TEX_{86} and isotope data. Geology, 34(9), 737-740.

Zhao, X., Heslop, D., & Roberts, A. P. (2015). A protocol for variable-resolution first-order reversal curve measurements. Geochemistry, Geophysics, Geosystems, 16(5), 1364-1377.

White, A.F., Peterson, M.L., and Hochella, M.F., 1994, Electrochemistry and dissolution kinetics of magnetite and ilmenite: Geochimica et Cosmochimica Acta, v. 58, p. 1859–1875.

Wieczorek, R., Fantle, M. S., Kump, L. R., & Ravizza, G. (2013). Geochemical evidence for volcanic activity prior to and enhanced terrestrial weathering during the Paleocene Eocene Thermal Maximum. *Geochimica et Cosmochimica Acta*, *119*, 391-410.

8. Attachments

Table 8.1 – Magnetic data of Zumaia samples (plotted at Figure 4.1). Negative and very high values (>14%) of Kfd were considered to be erroneous and they are not plotted in Figure 4.1. Samples marked with a star correspond to sampling errors, missed samples or samples without enough volume for magnetic measurements.

Sample	d (cm)	MS (m^3/kg)	Kfd (%)
Z-1	-500	7.777E-08	1.83
Z-2	-490	8.280E-08	1.04
Z-3	-480	9.724E-08	2.54
Z-4	-470	9.813E-08	2.11
Z-5	-460	1.054E-07	3.11
Z-6	-450	9.157E-08	2.53
Z-7	-440	8.604E-08	3.18
Z-8	-430	8.442E-08	3.16
Z-9	-420	9.083E-08	4.28
Z-10	-410	9.427E-08	2.79
Z-11	-400	8.159E-08	2.20
Z-12	-390	9.158E-08	2.71
Z-13	-380	9.824E-08	2.83
Z-14	-370	9.414E-08	3.19
Z-15	-360	1.289E-07	11.58
Z-16	-350	1.056E-07	2.78
Z-17	-340	1.209E-07	-24.71
Z-18	-330	1.211E-07	-3.01
Z-19	-320	9.969E-08	2.87
Z-20	-310	9.992E-08	-3.67
Z-21	-300	8.997E-08	2.25
Z-22	-290	9.287E-08	2.87
Z-23	-280	9.730E-08	1.71
Z-24	-270	1.030E-07	-0.62
Z-25	*	*	*
Z-26	-260	1.221E-07	-1.74
Z-27	-250	1.036E-07	2.15
Z-28	-240	1.096E-07	5.56
Z-29	-235	9.855E-08	3.58
Z-30	-230	1.002E-07	1.48
Z-31	-225	9.385E-08	-5.42
Z-32	-220	8.980E-08	7.95
Z-33	-215	6.357E-08	3.95
Z-34	-210	6.956E-08	3.71
Z-35	-205	6.355E-08	3.49
Z-36	-200	9.581E-08	4.54
Z-37	-195	9.470E-08	2.91
Z-38	-190	9.700E-08	2.21
Z-39	-185	9.844E-08	3.47
Z-40	-180	8.023E-08	-1.87
Z-41	-175	6.886E-08	2.33
Z-42	-170	8.581E-08	-0.58
Z-43	-165	1.085E-07	3.27
Z-44	-160	9.356E-08	3.09
Z-45	-155	8.883E-08	3.44
Z-46	-150	8.289E-08	3.04
Z-47	-145	9.030E-08	-4.87
Z-48	-140	9.439E-08	4.66
Z-49	-135	9.028E-08	2.04
Z-50	-130	8.182E-08	2.11
Z-51	-125	8.013E-08	-0.83
Z-52	-120	6.832E-08	2.89
Z-53	-115	8.716E-08	0.75
Z-54	-110	8.666E-08	2.49
Z-55	-105	8.833E-08	3.39
Z-56	-100	8.415E-08	2.94
Z-57	-95	8.513E-08	2.49
Z-58	-90	7.884E-08	2.27
Z-59	-85	6.024E-08	-5.50
Z-60	-80	8.043E-08	3.70
Z-61	-75	7.329E-08	3.58
Z-62	-70	7.566E-08	3.70
Z-63	-65	7.926E-08	1.66
Z-64	-60	7.350E-08	-4.33
Z-65	-55	7.824E-08	-0.06
Z-66	-50	7.064E-08	3.98
Z-67	-45	5.910E-08	2.81
Z-68	-40	6.762E-08	2.08
Z-69	-35	6.981E-08	1.01
Z-70	-30	7.230E-08	2.76
Z-71	-25	7.395E-08	2.45
Z-72	-20	7.156E-08	2.92
Z-73	-15	6.462E-08	1.01
Z-74	-10	7.621E-08	5.83
Z-75	-5	6.412E-08	-12.14
Z-76	-3	6.123E-08	2.28
Z-77	-1	6.330E-08	1.65
Z-78	0	3.845E-08	1.35
Z-79	2	4.660E-08	2.58
Z-80	5	8.676E-08	1.94
Z-81	10	6.128E-08	2.55
Z-82	15	7.438E-08	3.10
Z-83	20	6.710E-08	2.78
Z-84	25	6.543E-08	2.95
Z-85	30	6.707E-08	2.43
Z-86	35	5.608E-08	2.86
Z-87	37	3.996E-08	4.43
Z-88	50	4.157E-08	3.95
Z-89	55	7.044E-08	2.59
Z-90	75	5.733E-08	-3.09
Z-91	100	1.271E-08	5.99
Z-92	*	*	*
Z-93	155	1.316E-08	6.21
Z-94	170	1.453E-08	-2.33
Z-95	200	1.009E-08	4.68
Z-96	220	1.200E-08	5.08
Z-97	240	1.288E-08	4.16
Z-98	260	1.078E-08	-8.11
Z-99	*	*	*
Z-100	290	1.474E-08	5.10
Z-101	300	1.220E-08	4.33
Z-102	330	1.556E-08	-0.41
Z-103	355	2.181E-08	8.84
Z-104	380	2.421E-08	6.39
Z-105	400	2.311E-08	9.91
Z-106	415	2.187E-08	2.04
Z-107	455	1.907E-08	6.64
Z-108	460	5.437E-08	4.99
Z-109	485	1.347E-08	3.69
Z-110	*	*	*
Z-111	515	7.145E-08	4.22
Z-112	*	*	*
Z-113	545	1.447E-08	4.38

Table 8.2 – Magnetic data of Zumaia samples (plotted at Figure 4.3): Mass Specific Magnetic Susceptibility (MS), S-ratio and Coercivity (logB1/2), Isothermal remanent magnetization of saturation (SIRM) and Dispersion Parameter (DP) for each component.

Samples	d (cm)	MS (m^3/kg)	S-ratio	Comp. 1 (15-30 mT)			Comp. 2 (30-65 mT)			Comp. 3 (65-125 mT)			Comp. 4 (>125mT)		
				Log B1/2 (mT)	SIRM	DP	Log B1/2 (mT)	SIRM	DP	Log B1/2 (mT)	SIRM	DP	Log B1/2 (mT)	SIRM	DP
ZU8.30.1	286	1,40E-08	0,91	1,3	3,00E-02	0,31	1,478	4,00E-02	0,2	1,85	4,80E-02	0,2	2,45	3,00E-02	0,25
ZU8.27.6	280	1,28E-08	0,79	1,35	2,30E-02	0,3	1,53	1,80E-02	0,18	1,82	2,80E-02	0,17	2,3	5,00E-03	0,3
ZU8.26	273	9,67E-09	0,98	1,35	2,30E-02	0,33	1,55	2,50E-02	0,2	1,87	1,80E-02	0,16	2,35	5,00E-03	0,4
ZU8.25.11	265	1,09E-08	0,82	1,3	1,40E-02	0,3	1,55	2,60E-02	0,19	1,86	2,60E-02	0,16	2,35	1,00E-03	0,4
ZU8.22.20	241	9,98E-09	0,84	1,32	2,00E-02	0,3	1,536	2,20E-02	0,18	1,83	2,60E-02	0,18	2,5	1,00E-03	0,3
ZU8.22.9	230	1,29E-08	0,96	1,3	1,60E-02	0,3	1,57	2,20E-02	0,19	1,85	2,60E-02	0,14	2,3	1,00E-02	0,4
ZU8.20.9	210	1,12E-08	0,98	1,3	2,00E-02	0,3	1,51	2,00E-02	0,18	1,82	2,80E-02	0,16	2,4	4,00E-03	0,2
ZU8.18.15	175	1,07E-08	0,97	1,35	3,00E-02	0,28	1,5	1,76E-02	0,15	1,83	3,20E-02	0,15	2,55	5,50E-03	0,35
ZU8.18.2	171	1,01E-08	0,97	1,3	2,50E-02	0,28	1,62	2,60E-02	0,18	1,89	3,00E-02	0,16	2,4	7,00E-03	0,35
ZU8.15.6	157	9,95E-09	0,98	1,3	2,30E-02	0,3	1,62	2,80E-02	0,18	1,91	2,50E-02	0,16	2,35	5,00E-03	0,4
ZU8.14.2	146	1,12E-08	0,97	1,3	2,50E-02	0,3	1,58	2,00E-02	0,18	1,84	2,30E-02	0,16	2,2	1,10E-02	0,45
ZU8.13.3	139	1,03E-08	0,91	1,25	2,00E-02	0,3	1,5	3,50E-02	0,2	1,83	4,20E-02	0,15	2,35	3,80E-02	0,3
ZU8.10.8	123	1,26E-08	0,92	1,32	2,60E-02	0,28	1,62	5,00E-02	0,17	1,88	5,50E-02	0,16	2,3	9,80E-02	0,2
ZU8.9.3	113	1,41E-08	0,97	1,3	2,20E-02	0,3	1,57	2,60E-02	0,19	1,86	2,60E-02	0,16	2,2	9,50E-03	0,4
ZU8.7.1	101	1,57E-08	0,94	1,4	6,00E-02	0,28	1,77	1,00E-01	0,16	2,09	3,50E-01	0,14	2,35	1,20E-01	0,28
ZU8.6.4.1	70	1,42E-08	0,98	1,3	3,30E-02	0,3	1,56	3,50E-02	0,18	1,84	3,50E-02	0,15	2,2	9,00E-03	0,4
ZU8.6.2.5	68	1,41E-08	0,96	1,4	6,00E-02	0,33	1,65	5,00E-02	0,19	1,97	3,00E-02	0,13	2,15	1,05E-01	0,26
ZU8.4.13	63	1,68E-08	0,96	1,23	2,90E-02	0,28	1,57	4,50E-02	0,2	1,89	4,40E-02	0,15	2,45	1,20E-02	0,3
ZU8.4.9	59	2,10E-08	0,93	1,3	4,00E-02	0,35	1,67	9,00E-02	0,18	2,02	2,00E-01	0,18	2,5	7,00E-02	0,45
ZU8.4.4	54	2,63E-08	0,94	1,3	5,50E-02	0,28	1,66	2,40E-01	0,18	1,96	7,40E-01	0,18	2,3	3,00E-01	0,28
ZU8.3.5	48	2,02E-08	0,90	1,35	2,50E-02	0,28	1,65	3,00E-02	0,16	1,94	4,80E-02	0,15	2,4	3,80E-02	0,28
ZU8.1.2	41	2,48E-08	0,97	1,35	2,80E-02	0,3	1,58	2,50E-02	0,18	1,86	3,00E-02	0,14	2,3	1,20E-02	0,3
ZU8.1.1	40	2,04E-08	0,95	1,3	2,60E-02	0,3	1,55	3,30E-02	0,19	1,9	4,50E-02	0,16	2,25	2,50E-02	0,4
ZU7.18.2	38,5	3,72E-08	0,98	1,35	1,20E-01	0,3	1,6	5,50E-02	0,16	1,87	7,80E-02	0,13	2,2	2,50E-02	0,45
ZU7.18.1	37	3,76E-08	0,97	1,3	9,00E-02	0,3	1,57	6,00E-02	0,17	1,87	6,00E-02	0,12	2,45	1,50E-02	0,4

Table xx – (continued)

Samples	d (cm)	MS (m^3/kg)	S-ratio	Comp. 1 (15-30 mT)			Comp. 2 (30-65 mT)			Comp. 3 (65-125 mT)			Comp. 4 (>125mT)		
				Log B1/2 (mT)	SIRM	DP	Log B1/2 (mT)	SIRM	DP	Log B1/2 (mT)	SIRM	DP	Log B1/2 (mT)	SIRM	DP
ZU7.17	35,5	6,15E-08	0,95	1,37	2,00E-02	0,3	1,6	1,00E-02	0,16	1,83	1,30E-02	0,14	2,2	5,50E-03	0,28
ZU7.16.2	34	5,30E-08	0,98	1,3	3,50E-02	0,29	1,58	2,50E-02	0,16	1,85	2,50E-02	0,12	2,25	9,00E-03	0,33
ZU7.16.1	32,5	5,33E-08	0,98	1,3	5,00E-02	0,28	1,65	4,20E-02	0,16	1,9	2,60E-02	0,1	2,45	8,00E-03	0,4
ZU7.9	22	5,53E-08	0,98	1,27	3,00E-02	0,3	1,57	4,50E-02	0,17	1,89	3,20E-02	0,12	2,4	7,00E-03	0,4
ZU7.7	19	5,84E-08	0,98	1,2	1,80E-02	0,3	1,55	3,80E-02	0,18	1,85	3,10E-02	0,13	2,3	8,50E-03	0,3
ZU7.5.4	14,5	6,53E-08	0,96	1,25	1,50E-02	0,3	1,57	2,70E-02	0,21	1,85	1,90E-02	0,16	2,4	7,00E-03	0,3
ZU7.5.2	11,5	7,00E-08	0,97	1,25	1,30E-02	0,28	1,55	2,70E-02	0,19	1,85	1,75E-02	0,15	2,35	6,00E-03	0,3
ZU7.4.1	5,5	7,44E-08	0,97	1,27	1,40E-02	0,3	1,5	2,00E-02	0,16	1,8	2,70E-02	0,15	2,25	1,00E-02	0,3
ZU7.1	0	4,37E-08	0,79	1,4	1,30E-02	0,28	1,62	1,20E-02	0,17	1,96	1,90E-02	0,15	2,3	6,00E-03	0,3
ZU6.1.4	-6	5,40E-08	0,98	1,22	5,90E-02	0,3	1,58	7,00E-02	0,18	1,88	5,50E-02	0,11	2,3	1,60E-02	0,45
ZU6.2.4	-15	5,51E-08	0,97	1,22	5,90E-02	0,3	1,55	6,80E-02	0,17	1,85	6,50E-02	0,11	2,15	3,20E-02	0,5
ZU6.3.1	-21,25	5,69E-08	0,68	1,35	9,00E-02	0,3	1,6	2,00E-02	0,18	1,8	2,00E-02	0,18	2,4	7,00E-01	0,4
ZU6.3.4	-25	5,85E-08	0,68	1,37	8,00E-02	0,3	1,65	3,00E-02	0,18	1,85	1,50E-02	0,18	2,4	6,70E-01	0,35
ZU6.3.5	-26	5,74E-08	0,70	1,37	8,00E-02	0,3	1,57	4,80E-02	0,14	1,87	6,00E-02	0,12	2,41	6,00E-01	0,28
ZU6.4.3	-29	5,66E-08	0,67	1,3	8,00E-02	0,28	1,65	1,20E-01	0,17	1,9	7,00E-02	0,1	2,42	1,100E+00	0,29
ZU6.4.4	-30	5,67E-08	0,68	1,3	9,00E-02	0,28	1,65	1,10E-01	0,17	1,91	7,00E-02	0,1	2,42	1,05E+00	0,3
ZU6.5.3	-35	6,13E-08	0,66	1,3	7,00E-02	0,28	1,65	1,20E-01	0,17	1,91	1,00E-01	0,12	2,45	1,10E+00	0,35
ZU6.8	-39	6,32E-08	0,71	1,3	7,00E-02	0,28	1,65	1,80E-01	0,18	2	1,60E-01	0,12	2,4	1,30E+00	0,4
ZU6.11	-42	6,29E-08	0,69	1,3	1,10E-01	0,28	1,7	1,70E-01	0,19	1,98	1,10E-01	0,14	2,43	1,25E+00	0,35
ZU6.13	-44	6,28E-08	0,70	1,45	1,60E-01	0,33	1,63	1,10E-01	0,18	1,9	1,25E-01	0,14	2,45	8,70E-01	0,33
ZU 6.18	-59,3	6,98E-08	0,75	1,32	5,00E-02	0,28	1,67	1,00E-01	0,18	1,96	1,30E-01	0,15	2,47	8,10E-01	0,34
ZU 6.21	-69,8	7,00E-08	0,69	1,33	1,00E-01	0,3	1,68	2,00E-01	0,18	1,96	2,30E-01	0,15	2,45	1,30E+00	0,34
ZU 6.23	-76,8	7,18E-08	0,73	1,43	1,50E-01	0,28	1,75	3,00E-01	0,19	2,06	5,20E-01	0,16	2,44	1,65E+00	0,34
ZU 6.24	-80,3	6,93E-08	0,75	1,43	1,20E-01	0,28	1,75	2,50E-01	0,19	2,06	4,00E-01	0,16	2,43	1,25E+00	0,33
ZU 6.30	-91	6,62E-08	0,74	1,45	1,70E-01	0,28	1,75	2,70E-01	0,19	2,06	6,10E-01	0,16	2,44	1,62E+00	0,34

Table xx – (continued)

Samples	d (cm)	MS (m^3/kg)	S-ratio	Comp. 1 (15-30 mT)			Comp. 2 (30-65 mT)			Comp. 3 (65-125 mT)			Comp. 4 (>125mT)		
				Log B1/2 (mT)	SIRM	DP	Log B1/2 (mT)	SIRM	DP	Log B1/2 (mT)	SIRM	DP	Log B1/2 (mT)	SIRM	DP
ZU 6.31	-92	6,67E-08	0,76	1,45	1,70E-01	0,28	1,75	3,00E-01	0,19	2,08	7,10E-01	1,18	2,42	1,70E+00	0,34
ZU6.33.4	-97	6,82E-08	0,78	1,45	2,50E-01	0,28	1,75	4,00E-01	0,18	2,06	7,80E-01	1,43	2,42	1,70E+00	0,34
ZU6.33.5	-98	6,74E-08	0,75	1,42	1,50E-01	0,28	1,75	3,00E-01	0,18	2,06	4,00E-01	0,85	2,4	1,60E+00	0,36
ZU6.35.1	-112	6,60E-08	0,79	1,45	2,50E-01	0,28	1,74	6,00E-01	0,19	2,01	9,40E-01	1,79	2,46	1,62E+00	0,32
ZU6.42.6	-126	7,42E-08	0,75	1,42	2,00E-01	0,28	1,6	3,00E-01	0,15	1,94	7,50E-01	1,25	2,45	1,70E+00	0,35
ZU6.49.2	-136	8,10E-08	0,72	1,4	1,50E-01	0,28	1,65	3,00E-01	0,16	1,93	6,40E-01	1,09	2,43	2,45E+00	0,35
ZU6.54.3	-144	7,63E-08	0,70	1,45	1,80E-01	0,28	1,75	5,00E-01	0,19	2,05	5,00E-01	1,18	2,5	1,90E+00	0,33
ZU6.59.2	-160	7,66E-08	0,79	1,45	2,50E-01	0,28	1,8	8,00E-01	0,19	2,03	1,00E+00	2,05	2,55	1,25E+00	0,28
ZU6.67	-172	8,18E-08	0,78	1,45	2,80E-01	0,28	1,75	6,50E-01	0,17	2	9,00E-01	1,83	2,46	1,80E+00	0,33
ZU6.68	-173	8,13E-08	0,77	1,45	2,00E-01	0,3	1,75	5,80E-01	0,2	2,03	1,17E+00	1,95	2,67	1,10E+00	0,3
ZU6.77.1	-190	9,18E-08	0,67	1,4	1,80E-01	0,28	1,72	5,80E-01	0,19	2	5,80E-01	1,34	2,5	3,00E+00	0,34
ZU6.80.2	-198	9,04E-08	0,65	1,47	2,00E-01	0,3	1,73	4,50E-01	0,19	2	7,50E-01	1,4	2,52	3,10E+00	0,32
ZU6.93	-225	8,59E-08	0,78	1,4	2,30E-01	0,28	1,77	9,50E-01	0,19	2,04	1,05E+00	2,23	2,56	1,25E+00	0,25
ZU6.97	-235	8,43E-08	0,84	1,45	4,00E-01	0,28	1,73	6,00E-01	0,16	1,99	1,40E+00	2,4	2,54	1,00E+00	0,28

Table 8.3 – Magnetic data of Dababiya samples (plotted at Figure 4.5): Mass Specific Magnetic Susceptibility (MS), Frequency Dependent Susceptibility (Kfd), S-ratio and Coercivity (logB1/2), Isothermal remanent magnetization of saturation (SIRM) and Dispersion Parameter (DP) for each component. Negative and very high values (>14%) of Kfd were considered to be erroneous and they are not plotted in Figure 4.4. Samples marked with a star correspond to sampling errors, missed samples or samples without enough volume for magnetic measurements.

Samples	d (cm)	MS (m^3/kg)	Kfd (%)	S-ratio	Comp. 1 (20-35 mT)			Comp. 2 (38-50 mT)			Comp. 3 (50-125 mT)			Comp. 4 (>125mT)		
					Log B1/2 (mT)	SIRM	DP	Log B1/2 (mT)	SIRM	DP	Log B1/2 (mT)	SIRM	DP	Log B1/2 (mT)	SIRM	DP
Db -1	0	5.66E-08	2.62	0.18	1.2	4.00E-03	0.3	1.75	1.15E-02	0.25				3.09	6.10E-01	0.38
Db -2	0.1	5.59E-08	2.19	0.21	1.2	3.00E-03	0.35	1.77	1.00E-02	0.3				3.04	5.15E-01	0.39
Db -3	0.2	5.22E-08	1.61	0.13	1.2	2.00E-03	0.35	1.86	1.80E-02	0.4				3.07	4.00E-01	0.26
Db -4	*	*	*	*	*	*	*	*	*	*	*	*	*	*	*	*
Db -5	0.4	5.17E-08	2.89	0.16	1.25	1.00E-03	0.3	1.84	2.20E-02	0.4				3.03	4.60E-01	0.3
Db -6	0.5	5.30E-08	2.14	0.25	1.25	3.20E-03	0.25	1.8	4.46E-02	0.43				3.07	4.10E-01	0.28
Db -7	0.6	5.55E-08	3.07	0.22	1.25	2.00E-03	0.35	1.85	2.80E-02	0.43				3.05	5.00E-01	0.36
Db -8	0.7	5.67E-08	2.70	0.22	1.25	4.00E-03	0.35	1.84	1.80E-02	0.3				2.99	5.10E-01	0.36
Db -9	0.8	5.73E-08	2.00	*	*	*	*	*	*	*	*	*	*	*	*	*
Db -10	0.9	6.28E-08	13.65	0.27	1.2	3.50E-03	0.3	1.81	3.70E-02	0.4				3.04	4.00E-01	0.35
Db -11	1	5.83E-08	2.04	0.22	1.27	2.00E-03	0.35	1.81	2.10E-02	0.43				3.03	5.35E-01	0.38
Db -12	1.1	5.55E-08	2.77	0.11	1.25	2.00E-03	0.35	1.84	1.90E-02	0.44				3.06	6.30E-01	0.28
Db -13	1.15	5.56E-08	3.11	0.24	1.25	1.50E-03	0.35	1.8	2.90E-02	0.45				3.02	3.98E-01	0.35
Db -14	1.2	5.35E-08	5.95	0.19	1.3	1.00E-03	0.35	1.87	2.20E-02	0.48				3.07	4.55E-01	0.35
Db -15	1.25	5.15E-08	4.37	0.27	1.25	1.00E-04	0.34	1.87	4.25E-02	0.48				3.01	3.01E-01	0.31
Db -16	1.3	4.62E-08	3.43	0.25	1.25	1.00E-03	0.35	1.82	3.30E-02	0.45				3.09	3.13E-01	0.3
Db -17	1.35	4.67E-08	7.95	0.24	1.25	1.00E-04	0.28	1.81	3.10E-02	0.47				3.08	2.70E-01	0.27
Db -18	1.4	4.01E-08	5.24	0.18	1.25	1.00E-04	0.26	1.85	2.30E-02	0.47				3.09	3.20E-01	0.28
Db -19	1.45	3.83E-08	2.06	0.20	1.25	8.00E-04	0.3	1.89	2.05E-02	0.5				3.09	2.77E-01	0.31
Db -20	1.5	3.77E-08	1.84	0.19	1.25	1.00E-03	0.35	1.9	2.80E-02	0.47				3.08	4.15E-01	0.315
Db -21	1.55	3.58E-08	6.42	0.24	1.27	1.00E-03	0.35	1.77	2.40E-02	0.44				3.07	3.90E-01	0.37
Db -22	1.6	3.59E-08	3.55	0.26	1.25	1.00E-03	0.3	1.82	2.35E-02	0.45				3.06	2.91E-01	0.365
Db -23	*	*	*	*	*	*	*	*	*	*	*	*	*	*	*	*
Db -24	1.7	3.12E-08	-1.96	0.18	1.27	1.20E-03	0.35	1.82	1.80E-02	0.45				3.04	3.65E-01	0.325
Db -25	1.725	3.52E-08	3.99	0.17	1.25	1.00E-03	0.35	1.86	1.75E-02	0.45				3.09	4.15E-01	0.34

Table xx – (continued)

Samples	d (cm)	MS (m^3/kg)	Kfd (%)	S-ratio	Comp. 1 (20-35 mT)			Comp. 2 (38-50 mT)			Comp. 3 (50-125 mT)			Comp. 4 (>125mT)		
					Log B1/2 (mT)	SIRM	DP	Log B1/2 (mT)	SIRM	DP	Log B1/2 (mT)	SIRM	DP	Log B1/2 (mT)	SIRM	DP
Db -26	1.75	3.93E-08	3.40	0.22	1.3	9.00E-04	0.3	1.84	3.50E-02	0.47				3.05	4.70E-01	0.33
Db -27	1.775	3.70E-08	3.32	0.23	1.3	1.50E-03	0.35	1.85	1.35E-02	0.45				3.01	2.90E-01	0.37
Db -28	1.8	6.45E-08	3.79	0.24	1.25	1.00E-03	0.35	1.8	2.70E-02	0.46				3	5.40E-01	0.38
Db -29	1.825	8.04E-08	5.75	0.43	1.25	1.00E-03	0.35	1.89	4.00E-02	0.42				2.86	3.70E-01	0.47
Db -30	1.85	6.33E-08	4.23	0.45	1.25	2.10E-02	0.3	1.5	7.81E-02	0.19	2.05	3.50E-03	0.3	3.12	5.00E-01	0.42
Db -31	*	*	*	*	*	*	*	*	*	*	*	*	*	*	*	*
Db -32	1.9	6.33E-08	24.53	0.66	1.25	2.00E-02	0.3	1.5	6.60E-02	0.2	2.05	1.30E-02	0.3	3	1.30E-01	0.36
Db -33	1.925	5.26E-08	-64.54	0.39	1.25	3.00E-03	0.35	1.55	2.00E-02	0.24	2.07	8.00E-02	0.45	3.07	5.80E-01	0.43
Db -34	1.95	1.50E-07	178.88	0.89	1.25	6.50E-02	0.28	1.48	1.64E-01	0.175	2.2	2.10E-02	0.4	3.16	9.00E-02	0.38
Db -35	2	5.71E-08	3.33	0.84	1.25	6.00E-02	0.28	1.49	1.39E-01	0.19	2.1	6.00E-03	0.36	3.2	1.50E-01	0.48
Db -36	2.05	8.55E-08	5.21	0.95	1.21	1.50E-01	0.27	1.495	5.88E-01	0.19	2.2	1.56E-02	0.3	3.08	1.10E-01	0.45
Db -37	2.1	7.18E-08	3.78	0.58	1.26	2.50E-02	0.31	1.51	6.60E-02	0.2	2.06	4.00E-02	0.4	3.11	2.75E-01	0.35
Db -38	2.15	9.20E-08	4.08	0.96	1.23	1.50E-01	0.28	1.5	5.95E-01	0.19	2.2	4.00E-02	0.3	3.09	7.70E-02	0.29
Db -39	2.2	1.29E-07	4.85	0.98	1.2	3.00E-01	0.25	1.455	1.39E+00	0.19	2.2	4.00E-02	0.3	3.09	8.50E-02	0.27
Db -40	2.25	7.86E-08	1.82	0.67	1.24	9.00E-03	0.35	1.48	2.50E-02	0.22	2.2	1.47E-02	0.45	3.22	9.40E-02	0.27
Db -41	2.3	8.15E-08	2.39	0.81	1.23	1.30E-02	0.37	1.4	7.85E-02	0.26	2	2.30E-02	0.45	3.11	7.10E-02	0.26
Db -42	*	*	*	*	*	*	*	*	*	*	*	*	*	*	*	*
Db -43	2.4	6.50E-08	2.78	0.39	1.25	1.00E-03	0.34	1.69	3.80E-02	0.4				3.07	1.89E-01	0.34
Db -44	2.45	6.60E-08	4.26	0.26	1.25	1.00E-03	0.34	1.66	3.20E-02	0.39				2.98	3.20E-01	0.33
Db -45	2.5	6.45E-08	3.25	0.33	1.25	1.00E-03	0.35	1.73	3.60E-02	0.41				2.99	2.15E-01	0.33
Db -46	2.55	6.88E-08	3.12	0.22	1.25	1.00E-03	0.3	1.65	6.70E-02	0.37				3	7.60E-01	0.3
Db -47	2.6	4.03E-08	-2.80	0.21	1.25	1.00E-03	0.35	1.65	3.70E-02	0.42				3.1	5.80E-01	0.33
Db -48	2.65	4.36E-08	4.36	0.17	1.25	1.50E-03	0.3	1.74	2.40E-02	0.4				3.13	5.70E-01	0.32
Db -49	2.7	4.51E-08	7.78	0.22	1.25	1.00E-03	0.35	1.75	4.00E-02	0.42				3.14	5.50E-01	0.32
Db -50	2.75	4.51E-08	3.72	0.24	1.25	1.00E-03	0.3	1.72	4.45E-02	0.4				3.1	5.50E-01	0.335

Table xx – (continued)

Samples	d (cm)	MS (m^3/kg)	Kfd (%)	S-ratio	Comp. 1 (20-35 mT)			Comp. 2 (38-50 mT)			Comp. 3 (50-125 mT)			Comp. 4 (>125mT)		
					Log B1/2 (mT)	SIRM	DP	Log B1/2 (mT)	SIRM	DP	Log B1/2 (mT)	SIRM	DP	Log B1/2 (mT)	SIRM	DP
Db -51	2.88	5.09E-08	5.56	0.26	1.24	1.00E-03	0.34	1.72	2.65E-02	0.42				3.03	3.41E-01	0.36
Db -52	2.98	4.75E-08	2.05	0.32	1.25	1.00E-03	0.35	1.65	2.60E-02	0.4				3.06	1.85E-01	0.33
Db -53	3.18	4.75E-08	1.60	0.18	1.26	1.00E-03	0.35	1.65	1.50E-02	0.36				3.03	2.60E-01	0.3
Db -54	3.28	4.48E-08	1.54	0.21	1.25	1.00E-03	0.35	1.72	1.30E-02	0.42				3.03	1.72E-01	0.31
Db -55	3.38	4.05E-08	4.10	0.32	1.26	1.00E-03	0.3	1.7	1.50E-02	0.42				3.05	1.00E-01	0.31
Db -56	3.48	3.86E-08	2.35	0.26	1.22	1.00E-03	0.3	1.68	1.32E-02	0.38				3.06	1.31E-01	0.318
Db -57	*	*	*	*	*	*	*	*	*	*	*	*	*	*	*	*
Db -58	3.68	4.10E-08	1.33	0.29	1.27	1.00E-03	0.3	1.68	1.40E-02	0.37				3.08	1.22E-01	0.33
Db -59	3.78	4.00E-08	2.22	0.27	1.25	1.00E-03	0.3	1.7	1.40E-02	0.42				3.08	1.45E-01	0.34
Db -60	*	*	*	*	*	*	*	*	*	*	*	*	*	*	*	*

Table 8.4 – Mineralogical data of Zumaia samples (plotted at Figure 5.1). The concentration of Phyllosilicates, Quartz and Calcite is expressed as percentage of the total mass (wt%) of each sample.

Samples	d (cm)	MS (m^3/kg)	Phyllosilicates (wt%)	Quartz (wt%)	Calcite (wt%)
Z-1	-500	7,78E-08	38,68	14,96	38,03
Z-2	-490	8,28E-08	31,74	15,82	41,33
Z-3	-480	9,72E-08	38,94	13,90	39,73
Z-4	-470	9,81E-08	37,11	14,85	41,70
Z-5	-460	1,05E-07	39,24	16,56	37,93
Z-6	-450	9,16E-08	47,03	11,43	39,02
Z-7	-440	8,60E-08	34,46	17,63	45,23
Z-8	-430	8,44E-08	32,21	12,95	47,03
Z-9	-420	9,08E-08	36,12	13,76	44,02
Z-10	-410	9,43E-08	40,97	17,74	33,93
Z-11	-400	8,16E-08	42,65	14,93	39,23
Z-12	-390	9,16E-08	37,84	15,02	41,03
Z-13	-380	9,82E-08	35,89	13,86	44,45
Z-14	-370	9,41E-08	32,59	12,32	49,23
Z-15	-360	1,29E-07	38,76	8,64	48,74
Z-16	-350	1,06E-07	37,34	16,60	43,44
Z-17	-340	1,21E-07	38,18	14,94	41,83
Z-18	-330	1,21E-07	37,91	16,07	40,48
Z-19	-320	9,97E-08	35,93	15,89	43,10
Z-20	-310	9,99E-08	38,65	17,51	32,93
Z-21	-300	9,00E-08	38,90	18,93	36,20
Z-22	-290	9,29E-08	39,95	17,16	40,00
Z-23	-280	9,73E-08	41,29	14,67	39,35
Z-24	-270	1,03E-07	38,67	17,27	40,04
Z-27	-250	1,04E-07	35,94	18,32	40,02
Z-28	-240	1,10E-07	34,97	15,40	45,12
Z-30	-230	1,00E-07	30,65	14,25	48,22
Z-31	-225	9,38E-08	36,02	15,88	42,15
Z-32	-220	8,98E-08	37,51	21,63	37,02
Z-33	-215	6,36E-08	43,12	14,73	35,92

Samples	d (cm)	MS (m^3/kg)	Phyllosilicates (wt%)	Quartz (wt%)	Calcite (wt%)
Z-35	-205	6,36E-08	37,66	15,65	40,03
Z-36	-200	9,58E-08	43,94	17,67	33,80
Z-37	-195	9,47E-08	41,70	14,44	39,78
Z-38	-190	9,70E-08	39,78	17,82	38,02
Z-39	-185	9,84E-08	39,82	14,85	39,02
Z-40	-180	8,02E-08	35,03	19,52	40,23
Z-41	-175	6,89E-08	39,71	22,14	32,84
Z-42	-170	8,58E-08	33,19	16,02	43,20
Z-43	-165	1,09E-07	36,32	14,45	46,65
Z-44	-160	9,36E-08	36,82	22,35	38,03
Z-45	-155	8,88E-08	30,99	12,26	52,10
Z-46	-150	8,29E-08	30,78	12,73	50,83
Z-47	-145	9,03E-08	32,45	13,11	51,02
Z-48	-140	9,44E-08	29,90	14,66	47,89
Z-49	-135	9,03E-08	33,83	16,02	46,02
Z-50	-130	8,18E-08	31,99	13,08	50,45
Z-51	-125	8,01E-08	37,54	16,17	41,81
Z-53	-115	8,72E-08	37,95	13,42	42,67
Z-54	-110	8,67E-08	36,18	13,36	44,66
Z-55	-105	8,83E-08	33,40	12,38	49,02
Z-56	-100	8,41E-08	42,36	13,07	39,03
Z-57	-95	8,51E-08	36,35	12,86	47,02
Z-58	-90	7,88E-08	33,03	13,28	50,33
Z-60	-80	8,04E-08	28,55	12,03	55,02
Z-61	-75	7,33E-08	27,93	11,32	55,90
Z-62	-70	7,57E-08	30,33	15,79	49,02
Z-63	-65	7,93E-08	41,91	12,70	39,02
Z-64	-60	7,35E-08	35,59	14,30	46,98
Z-65	-55	7,82E-08	32,36	13,04	50,02
Z-66	-50	7,06E-08	32,19	14,48	50,33

Table xx – (continued)

Samples	d (cm)	MS (m^3/kg)	Phyllosilicates (wt%)	Quartz (wt%)	Calcite (wt%)
Z-68	-40	6,76E-08	33,46	12,03	50,33
Z-69	-35	6,98E-08	31,25	14,06	51,02
Z-70	-30	7,23E-08	29,06	15,23	52,23
Z-71	-25	7,40E-08	34,69	12,15	49,02
Z-72	-20	7,16E-08	28,02	13,17	54,02
Z-73	-15	6,46E-08	36,22	10,73	50,02
Z-74	-10	7,62E-08	32,10	14,43	51,02
Z-75	-5	6,41E-08	31,08	12,47	47,12
Z-76	-3	6,12E-08	33,15	11,54	49,23
Z-77	-1	6,33E-08	37,31	14,15	42,70
Z-78	0	3,84E-08	16,41	9,95	72,92
Z-79	2	4,66E-08	24,02	11,82	54,02
Z-80	5	8,68E-08	44,94	27,85	19,41
Z-81	10	6,13E-08	26,92	24,02	42,12
Z-82	15	7,44E-08	27,93	20,83	41,77
Z-83	20	6,71E-08	30,78	18,78	41,92
Z-84	25	6,54E-08	32,92	19,25	42,11
Z-85	30	6,71E-08	28,72	15,02	48,02
Z-86	35	5,61E-08	30,62	16,88	44,29
Z-87	37	4,00E-08	26,78	14,17	55,08
Z-88	50	4,16E-08	17,26	23,75	54,01
Z-89	55	7,04E-08	33,81	13,90	48,49
Z-90	75	5,73E-08	10,59	4,77	81,31
Z-91	100	1,27E-08	9,45	1,81	87,05
Z-93	155	1,32E-08	12,40	3,53	83,21
Z-94	170	1,45E-08	6,92	2,05	88,73
Z-95	200	1,01E-08	11,00	2,40	84,94
Z-96	220	1,20E-08	7,45	3,82	86,02
Z-97	240	1,29E-08	6,58	2,00	88,67
Z-98	260	1,08E-08	7,82	2,00	87,52

Samples	d (cm)	MS (m^3/kg)	Phyllosilicates (wt%)	Quartz (wt%)	Calcite (wt%)
Z-100	290	1,47E-08	7,29	9,82	81,56
Z-101	300	1,22E-08	6,07	2,08	89,22
Z-102	330	1,56E-08	5,75	3,15	88,92
Z-103	355	2,18E-08	3,89	5,01	90,32
Z-104	380	2,42E-08	6,89	2,92	89,10
Z-105	400	2,31E-08	13,40	5,43	80,23
Z-106	415	2,19E-08	6,02	2,59	90,34
Z-107	455	1,91E-08	2,81	2,99	91,72
Z-108	460	5,44E-08	27,03	9,14	58,22
Z-109	485	1,35E-08	8,02	3,78	83,20
Z-111	515	7,14E-08	35,10	11,15	45,33
Z-113	545	1,45E-08	8,03	4,30	86,34

Table 8.5 – Mineralogical data of Dababiya samples (plotted at figure 5.7). The concentration of Phyllosilicates, Quartz and Calcite is expressed as percentage of the total mass (wt%) each sample.

Samples	d (cm)	MS (m^3/kg)	Phyllosilicates (%)	Quartz (%)	Calcite (%)
Db -1	0	5.66E-08	43.02	4.64	47.98
Db -2	0.1	5.59E-08	41.04	4.04	44.01
Db -3	0.2	5.22E-08	44.63	5.33	47.87
Db -4	*	*	*	*	*
Db -5	0.4	5.17E-08	38.92	3.94	41.87
Db -6	0.5	5.30E-08	40.03	5.77	39.45
Db -7	0.6	5.55E-08	38.78	4.80	42.65
Db -8	0.7	5.67E-08	39.22	5.38	38.90
Db -9	0.8	5.73E-08	*	*	*
Db -10	0.9	6.28E-08	51.23	6.57	32.87
Db -11	1	5.83E-08	44.23	4.93	33.17
Db -12	1.1	5.55E-08	39.12	6.62	36.78
Db -13	1.15	5.56E-08	45.73	5.66	33.91
Db -14	1.2	5.35E-08	40.32	6.30	40.13
Db -15	1.25	5.15E-08	43.48	5.84	37.45
Db -16	1.3	4.62E-08	40.12	6.75	45.70
Db -17	1.35	4.67E-08	44.34	8.90	40.12
Db -18	1.4	4.01E-08	40.88	7.09	44.07
Db -19	1.45	3.83E-08	40.03	8.34	45.34
Db -20	1.5	3.77E-08	35.09	9.01	50.03
Db -21	1.55	3.58E-08	30.89	9.63	56.00
Db -22	1.6	3.59E-08	27.89	10.88	55.12
Db -23	*	*	*	*	*
Db -24	1.7	3.12E-08	35.09	9.01	50.03
Db -25	1.725	3.52E-08	40.02	9.59	47.02
Db -26	1.75	3.93E-08	45.55	8.63	40.74
Db -27	1.775	3.70E-08	45.41	9.31	41.90
Db -28	1.8	6.45E-08	57.74	8.21	5.44
Db -29	1.825	8.04E-08	60.33	9.90	1.28
Db -30	1.85	6.33E-08	71.02	14.34	0.65

Samples	d (cm)	MS (m^3/kg)	Phyllosilicates (%)	Quartz (%)	Calcite (%)
Db -31	*	*	*	*	*
Db -32	1.9	6.33E-08	71.53	15.89	0.92
Db -33	1.925	5.26E-08	34.36	2.90	0.04
Db -34	1.95	1.50E-07	70.23	16.03	0.62
Db -35	2	5.71E-08	73.02	20.34	2.02
Db -36	2.05	8.55E-08	72.11	20.02	0.30
Db -37	2.1	7.18E-08	66.89	22.23	0.00
Db -38	2.15	9.20E-08	61.45	27.44	0.86
Db -39	2.2	1.29E-07	59.07	22.14	0.34
Db -40	2.25	7.86E-08	35.31	12.43	33.56
Db -41	2.3	8.15E-08	33.56	11.90	35.78
Db -42	*	*	*	*	*
Db -43	2.4	6.50E-08	22.12	7.52	17.52
Db -44	2.45	6.60E-08	28.34	11.05	23.54
Db -45	2.5	6.45E-08	25.89	8.77	28.07
Db -46	2.55	6.88E-08	22.68	7.58	10.38
Db -47	2.6	4.03E-08	16.90	6.34	18.32
Db -48	2.65	4.36E-08	27.18	8.30	36.89
Db -49	2.7	4.51E-08	21.51	7.59	28.10
Db -50	2.75	4.51E-08	30.12	8.34	31.34
Db -51	2.88	5.09E-08	30.17	5.08	40.00
Db -52	2.98	4.75E-08	38.01	7.45	42.21
Db -53	3.18	4.75E-08	30.87	5.83	43.12
Db -54	3.28	4.48E-08	37.28	5.99	51.28
Db -55	3.38	4.05E-08	28.92	4.05	45.29
Db -56	3.48	3.86E-08	34.45	4.34	53.51
Db -57	*	*	*	*	*
Db -58	3.68	4.10E-08	31.63	6.02	60.89
Db -59	3.78	4.00E-08	33.96	5.39	57.34
Db -60	*	*	*	*	*